



**NAVAL
POSTGRADUATE
SCHOOL**

MONTEREY, CALIFORNIA

THESIS

**EXTENDING THE ENDURANCE, MISSIONS AND
CAPABILITIES OF MOST UAVS USING ADVANCED
FLEXIBLE/RIDGED SOLAR CELLS AND NEW HIGH
POWER DENSITY BATTERIES TECHNOLOGY**

by

Chee Keen Chin

March 2011

Thesis Advisor:
Second Reader:

Sherif Michael
Rudolf Panholzer

Approved for public release; distribution is unlimited

THIS PAGE INTENTIONALLY LEFT BLANK

REPORT DOCUMENTATION PAGE			Form Approved OMB No. 0704-0188
Public reporting burden for this collection of information is estimated to average 1 hour per response, including the time for reviewing instruction, searching existing data sources, gathering and maintaining the data needed, and completing and reviewing the collection of information. Send comments regarding this burden estimate or any other aspect of this collection of information, including suggestions for reducing this burden, to Washington headquarters Services, Directorate for Information Operations and Reports, 1215 Jefferson Davis Highway, Suite 1204, Arlington, VA 22202-4302, and to the Office of Management and Budget, Paperwork Reduction Project (0704-0188) Washington DC 20503.			
1. AGENCY USE ONLY (Leave blank)	2. REPORT DATE March 2011	3. REPORT TYPE AND DATES COVERED Master's Thesis	
4. TITLE AND SUBTITLE Extending the Endurance, Missions and Capabilities of Most UAVs Using Advanced Flexible / Ridged Solar Cells and New High Power Density Batteries Technology		5. FUNDING NUMBERS	
6. AUTHOR(S) Chee Keen Chin			
7. PERFORMING ORGANIZATION NAME(S) AND ADDRESS(ES) Naval Postgraduate School Monterey, CA 93943-5000		8. PERFORMING ORGANIZATION REPORT NUMBER	
9. SPONSORING /MONITORING AGENCY NAME(S) AND ADDRESS(ES) Unmanned Aerial Systems Weaponization Laboratory, Naval Air Warfare Center Weapons Division (NAWCWD) China Lake, CA		10. SPONSORING/MONITORING AGENCY REPORT NUMBER	
11. SUPPLEMENTARY NOTES The views expressed in this thesis are those of the author and do not reflect the official policy or position of the Department of Defense or the U.S. Government. IRB Protocol number _____ N/A _____.			
12a. DISTRIBUTION / AVAILABILITY STATEMENT Approved for public release; distribution is unlimited		12b. DISTRIBUTION CODE	
13. ABSTRACT (maximum 200 words) The extension of flight time for military miniature unmanned aerial vehicles (UAVs) has been demonstrated through the implementation of thin-film photovoltaic (TFPV) cells. Currently, most electric mini-UAVs are powered by high energy density lithium-ion or lithium polymer batteries; however, the flight endurance is usually limited between 60 to 90 minutes before requiring a forced recovery to replace exhausted batteries. In this thesis, the viability of extending flight endurance by complementing the on-board battery source of a mini-UAV using advanced TFPV cells made of copper-indium-gallium di-selenide (CIGS) semiconductor materials is considered. In order to achieve a higher efficiency, the simulation and testing phase incorporates the use of a DC-to-DC converter and a maximum power point tracking device or algorithm to provide the desired output voltage and deliver maximum power from the TFPV cells to the battery and load. In addition to investigating the application of TFPV cell technology, development of new high power/energy density batteries and fuel cells technologies, as well as the potential benefit of applying less mature, high-efficiency photovoltaic cells to military UAVs are also considered.			
14. SUBJECT TERMS Thin-Film Photovoltaics, CIGS, UAV Systems, Solar Array, Maximum Power Point Tracker (MPPT), Energy Storage Systems, Fuel Cells		15. NUMBER OF PAGES 197	
		16. PRICE CODE	
17. SECURITY CLASSIFICATION OF REPORT Unclassified	18. SECURITY CLASSIFICATION OF THIS PAGE Unclassified	19. SECURITY CLASSIFICATION OF ABSTRACT Unclassified	20. LIMITATION OF ABSTRACT UU

THIS PAGE INTENTIONALLY LEFT BLANK

Approved for public release; distribution is unlimited

**EXTENDING THE ENDURANCE, MISSIONS AND CAPABILITIES OF MOST
UAVs USING ADVANCED FLEXIBLE/RIDGED SOLAR CELLS AND NEW
HIGH POWER DENSITY BATTERIES TECHNOLOGY**

Chee Keen Chin
Civilian, Defence Science and Technology Agency, Singapore
B.Eng (Hons), Nanyang Technological University, 2001

Submitted in partial fulfillment of the
requirements for the degree of

MASTER OF SCIENCE IN ELECTRICAL ENGINEERING

from the

**NAVAL POSTGRADUATE SCHOOL
March 2011**

Author: Chee Keen Chin

Approved by: Sherif Michael
Thesis Advisor

Rudolf Panholzer
Second Reader

Clark Robertson
Chairman, Department of Electrical and
Computer Engineering

THIS PAGE INTENTIONALLY LEFT BLANK

ABSTRACT

The extension of flight time for military miniature unmanned aerial vehicles (UAVs) has been demonstrated through the implementation of thin-film photovoltaic (TFPV) cells. Currently, most electric mini-UAVs are powered by high energy density lithium-ion or lithium polymer batteries; however, the flight endurance is usually limited between 60 to 90 minutes before requiring a forced recovery to replace exhausted batteries. In this thesis, the viability of extending flight endurance by complementing the on-board battery source of a mini-UAV using advanced TFPV cells made of copper-indium-gallium di-selenide (CIGS) semiconductor materials is considered. In order to achieve a higher efficiency, the simulation and testing phase incorporates the use of a DC-to-DC converter and a maximum power point tracking device or algorithm to provide the desired output voltage and deliver maximum power from the TFPV cells to the battery and load. In addition to investigating the application of TFPV cell technology, development of new high power/energy density batteries and fuel cell technologies, as well as the potential benefit of applying less mature, high-efficiency photovoltaic cells to military UAVs are also considered.

THIS PAGE INTENTIONALLY LEFT BLANK

TABLE OF CONTENTS

I.	INTRODUCTION	1
A.	BACKGROUND	1
B.	OBJECTIVE	3
C.	RELATED WORK	4
D.	APPROACH	4
E.	ORGANIZATION	5
II.	MINI-UAV SYSTEMS	7
A.	TRACKER	7
B.	RAVEN RQ-11B	9
C.	DESERT HAWK	11
D.	DRAGANFLY TANGO	12
E.	ALADIN	14
F.	SKYLARK	15
G.	SCAN-EAGLE	18
H.	SKYLITE B	20
I.	PUMA	22
J.	SKYBLADE III	24
K.	CHAPTER SUMMARY	25
III.	ENERGY STORAGE TECHNOLOGIES	27
A.	SODIUM-SULFUR BATTERY (NA-S)	28
B.	LITHIUM SULFUR BATTERY	29
1.	Advantages and Drawbacks of Lithium-Sulfur Cells	30
C.	LITHIUM ION (LI-ION) AND LITHIUM POLYMER (LI-PO) BATTERY	31
1.	Advantages and Limitations of Lithium Battery	33
D.	NICKEL-CADMIUM (NI-CD) BATTERY	33
1.	Advantages and Limitations of Nickel-Cadmium Battery	35
E.	NICKEL-METAL-HYDRIDE (NI-MH) BATTERY	36
1.	Advantages and Limitations of Nickel-Metal- Hydride Battery	38
F.	FLYWHEEL	39
1.	Advantages and Limitations of Flywheel	40
G.	ULTRA-CAPACITOR OR SUPER-CAPACITOR	41
1.	Advantages and Limitations of Super- Capacitors	43
H.	CHAPTER SUMMARY	45
IV.	FUEL CELL TECHNOLOGIES	49
A.	POLYMER ELECTROLYTE MEMBRANE (PEM) FUEL CELLS	51

B.	DIRECT METHANOL FUEL CELLS	53
C.	ALKALINE FUEL CELLS	55
D.	PHOSPHORIC ACID FUEL CELLS	56
E.	MOLTEN CARBONATE FUEL CELLS	57
F.	SOLID OXIDE FUEL CELLS	57
G.	REGENERATIVE OR REVERSIBLE FUEL CELLS	58
H.	CHAPTER SUMMARY	60
V.	SOLAR CELLS AND POWER DEVICES	61
A.	INTRODUCTION	61
B.	SOLAR SPECTRUM AND SOLAR RADIATION	63
1.	Air Mass	64
C.	SOLAR CELLS	65
1.	P-N Junctions	67
2.	Band Gap Energy	68
3.	Photovoltaic Effect	69
4.	Factors Affecting Cell Efficiency	69
D.	THIN-FILM SOLAR CELLS	70
1.	Performance of CIGS Solar Cells	72
2.	Degradation and Encapsulation of CIGS Solar Cells	73
E.	DC-TO-DC POWER CONVERTERS	74
1.	Buck Converter	74
2.	Boost Chopper	75
3.	Buck-Boost Chopper (Polarity Reversal)	76
F.	MAXIMUM POWER POINT TRACKER	77
G.	BATTERY BALANCER CHARGER	79
H.	CHAPTER SUMMARY	79
VI.	SOLAR PANEL TESTING, DESIGN AND ASSEMBLY	81
A.	TEST PLAN FOR EXPERIMENTAL SOLAR ARRAY CONFIGURATION	81
1.	Preliminary Testing without Laminated Solar Panel	84
2.	Preliminary Testing with Laminated Solar Panel	86
3.	Test Conclusion	87
B.	FINAL SOLAR ARRAY ARRANGEMENT	89
C.	PREPARATION WORK FOR FINAL SOLAR ARRAY	91
D.	LAMINATION OF FINAL SOLAR ARRAY	92
E.	ELECTRICAL CONNECTIONS	93
F.	SPV1020 DC-TO-DC BOOST CONVERTER WITH BUILT-IN MAXIMUM POWER POINT TRACKER ALGORITHM	95
1.	Partitioning Input and Output Voltages	97
2.	SPV1020 as a Battery Charger	98
G.	GENASUN MAXIMUM POWER POINT TRACKER	100
H.	SYSTEM INTEGRATION	101

I.	CHAPTER SUMMARY	102
VII.	TEST AND ANALYSIS	103
A.	SOLAR ARRAY TESTING	104
B.	VALIDATION OF BASIC SIMULATION MODELS	105
1.	Simulation Results Using Battery without Solar Panel	109
2.	Simulation Results Using Battery and Solar Panel	113
C.	DETERMINATION OF AVERAGE ENERGY CONSUMED AT DIFFERENT THROTTLE SPEEDS	120
D.	SIMULATION TEST FOR FINAL SOLAR ARRAY	124
E.	CONCLUSION ON SIMULATION WORK	148
F.	OBSERVATIONS	148
1.	Ground Tests	148
2.	Operating Temperature and Sunlight Irradiance	149
3.	Simulink Models	149
G.	CHAPTER SUMMARY	150
VIII.	CONCLUSIONS	151
A.	RECOMMENDATIONS	152
1.	Simulation Models	152
2.	New Technology CIGS, Energy Storage, and Power Electronics Devices	153
3.	Improved Aerodynamics	153
4.	Indoor Testing Facility	154
APPENDIX A.	MATLAB SOURCE CODES	155
A.	GENERIC CODES FOR SIMULINK MODEL	155
B.	DATA AND GENERIC CODES FOR PLOTTING VARIOUS FLIGHT ENDURANCES AT DIFFERENT THROTTLE SPEED SETTINGS	155
	LIST OF REFERENCES	157
	INITIAL DISTRIBUTION LIST	171

THIS PAGE INTENTIONALLY LEFT BLANK

LIST OF FIGURES

Figure 1.	Tracker mini-UAV. (From [6]).....	9
Figure 2.	Raven RQ-11B mini-UAV. (From [9]).....	11
Figure 3.	Desert Hawk III mini-UAV. (From [11]).....	12
Figure 4.	DraganFly Tango mini-UAV. (From [12]).....	14
Figure 5.	Aladin mini-UAV. (From [15]).....	15
Figure 6.	Skylark mini-UAV. (From [20]).....	18
Figure 7.	ScanEagle mini-UAV. (From [21]).....	20
Figure 8.	Skylite B mini-UAV. (From [23]).....	22
Figure 9.	Puma mini-UAV. (From [29]).....	23
Figure 10.	Skyblade III mini-UAV. (From [31]).....	25
Figure 11.	Sodium sulfur battery. (From [34]).....	29
Figure 12.	Lithium sulfur battery. (From [36]).....	30
Figure 13.	Lithium polymer battery. (From [39]).....	32
Figure 14.	Nickel-cadmium battery. (From [42]).....	34
Figure 15.	Nickel-metal-hydride battery. (From [44]).....	37
Figure 16.	Example of Flywheels used in energy storage systems. (From [46]).....	40
Figure 17.	Super-capacitors. (From [50]).....	43
Figure 18.	Basic operation of a fuel cell. (From [56]).....	50
Figure 19.	PEM fuel cell stack. (From [61]).....	53
Figure 20.	Micro direct methanol fuel cell. (After [65]).....	55
Figure 21.	Electolyzer and reversible fuel cell. (After [73]).....	59
Figure 22.	CIGS TFPV cell. (From [77]).....	62
Figure 23.	Electromagnetic spectrum. (From [79]).....	63
Figure 24.	Air mass. (After [80]).....	64
Figure 25.	Current and voltage curve at different light intensities. (From [81]).....	66
Figure 26.	Band gap diagram. (After [83]).....	69
Figure 27.	Solar cell structure. (From [85]).....	70
Figure 28.	Typical process flow for preparing a flexible CIGS submodule cell. (From [87]).....	72
Figure 29.	Buck chopper. (From [91]).....	75
Figure 30.	Boost chopper. (From [92]).....	76
Figure 31.	Buck-boost chopper (polarity reversal). (From [93]).....	77
Figure 32.	First solar panel (630 cm ²).....	82
Figure 33.	Second solar panel (1890 cm ²).....	82
Figure 34.	Solar array test setup circuitry.....	83
Figure 35.	Amprobe Solar-600, Solar Analyzer.....	83
Figure 36.	Amprobe Solar-100, Solar Power Meter.....	84
Figure 37.	IV curve for first solar panel without lamination.....	85

Figure 38.	IV curve for second solar panel without lamination.....	85
Figure 39.	IV curve for first solar panel with lamination..	86
Figure 40.	IV curve for second solar panel with lamination.....	87
Figure 41.	CIGS TFPV cells. (After [100]).....	89
Figure 42.	Solar array arrangement.....	90
Figure 43.	Slicing CIGS TFPV cells.....	92
Figure 44.	Clear adhesive tape. (From [101]).....	93
Figure 45.	Solar array lamination.....	93
Figure 46.	Self-adhesive flat copper tape. (From [102])....	94
Figure 47.	Solar array wiring.....	95
Figure 48.	SPV1020 DC-to-DC boost converter evaluation pack. (After [104]).....	98
Figure 49.	ST SEA05. (From [103]).....	99
Figure 50.	SPV1020 as a battery charger. (After [103])....	100
Figure 51.	GV26-4 solar charge controller. (From [3])....	100
Figure 52.	Schematic diagram for final system integration.	102
Figure 53.	IV curve for final solar array without lamination.....	104
Figure 54.	IV curve for final solar array with lamination.	104
Figure 55.	Simulation model with solar panel.....	106
Figure 56.	Simulation model without solar panel.....	107
Figure 57.	Simulation for battery energy consumption at throttle speed (100%-55%) without solar panel..	110
Figure 58.	Simulation for battery energy consumption at throttle speed (100%-65%) without solar panel..	111
Figure 59.	Simulation for battery energy consumption at throttle speed (100%-70%) without solar panel..	112
Figure 60.	Simulation for battery energy consumption with solar panel (12 W) and MPPT at throttle speed (100%-55%).....	114
Figure 61.	Simulation for battery energy consumption with solar panel (17 W) and MPPT at throttle speed (100%-55%).....	115
Figure 62.	Simulation for battery energy consumption with solar panel (12 W) and MPPT at throttle speed (100%-65%).....	116
Figure 63.	Simulation for battery energy consumption with solar panel (17 W) and MPPT at throttle speed (100%-65%).....	117
Figure 64.	Simulation for battery energy consumption with solar panel (12 W) and MPPT at throttle speed (100%-70%).....	118

Figure 65.	Simulation for battery energy consumption with solar panel (17 W) and MPPT at throttle speed (100%-70%).....	119
Figure 66.	Raven mini-UAV throttle speed equivalent resistance.....	121
Figure 67.	Enhanced simulation model with and without solar array.....	125
Figure 68.	Simulation for battery energy consumption with and without solar array at throttle speed (100% - 40%).....	126
Figure 69.	Simulation for battery energy consumption with and without solar array at throttle speed (100%-45%).....	127
Figure 70.	Simulation for battery energy consumption with and without solar array at throttle speed (100%-50%).....	128
Figure 71.	Simulation for battery energy consumption with and without solar array at throttle speed (100%-55%).....	129
Figure 72.	Simulation for battery energy consumption with and without solar array at throttle speed (100%-60%).....	130
Figure 73.	Simulation for battery energy consumption with and without solar array at throttle speed (100%-65%).....	131
Figure 74.	Simulation for battery energy consumption with and without solar array at throttle speed (100%-70%).....	132
Figure 75.	Simulation for battery energy consumption with and without solar array at throttle speed (100%-75%).....	133
Figure 76.	Simulation for battery energy consumption with and without solar array at throttle speed (100%-80%).....	134
Figure 77.	Simulation for battery energy consumption with and without solar array at throttle speed (100%-85%).....	135
Figure 78.	Simulation for battery energy consumption with and without solar array at throttle speed (100%-90%).....	136
Figure 79.	Simulation for battery energy consumption with and without solar array at throttle speed (100%-95%).....	137
Figure 80.	Simulation for battery energy consumption with and without solar array at throttle speed (100%).....	138

Figure 81. General equation associated with flight endurance (without solar array).....143

Figure 82. Normalized equation associated with flight endurance (solar array with output power 18.11 W).....144

Figure 83. Normalized equation associated with flight endurance (solar array with output power 32.44 W).....145

Figure 84. Normalized equation associated with flight endurance (solar array with output power 40 W).147

Figure 85. Airfoil. (After [106]).....154

LIST OF TABLES

Table 1.	UAV tier classification and characteristics. (After [1]).....	2
Table 2.	Overview of Tracker mini-UAV system capabilities. (After [4]).....	9
Table 3.	Overview of Raven RQ-11B mini-UAV system capabilities. (After [7]).....	10
Table 4.	Overview of Desert Hawk III mini-UAV system capabilities. (After [10]).....	12
Table 5.	Overview of DraganFly Tango mini-UAV system capabilities. (From [12]).....	13
Table 6.	Overview of Aladin mini-UAV system capabilities. (From [14]).....	15
Table 7.	Overview of Skylark mini-UAV system capabilities. (From [18], [19]).....	17
Table 8.	Overview of Scan-Eagle mini-UAV system capabilities. (From [22]).....	19
Table 9.	Overview of Skylite B mini-UAV system capabilities. (After [24]).....	21
Table 10.	Overview of Puma mini-UAV system capabilities. (After [27],[28]).....	23
Table 11.	Overview of Skyblade III mini-UAV system capabilities. (After [30]).....	25
Table 12.	Comparison table between various types of energy storage systems. (After [53],[54]).....	46
Table 13.	Solar panels test measurement under sunlight conditions.....	88
Table 14.	SPV1020 electrical characteristics. (From [103]).....	96
Table 15.	GV24-6 solar charge controller specifications. (After [3]).....	101
Table 16.	IV curves data for final solar array.....	105
Table 17.	Summary of actual Raven mini-UAV energy consumption and flight endurance test data. (After [3]).....	108
Table 18.	Comparison between simulation results and actual flight endurance data [3] without solar panel incorporated.....	112
Table 19.	Comparison between simulation results and actual data [3] using battery and solar panel with MPPT.....	119
Table 20.	Throttle speed equivalent resistance. (After [3]).....	120

Table 21.	Average battery capacity (AH) and battery energy capacity (WH) consumption.....	122
Table 22.	Computation of output power for simulation.....	124
Table 23.	Simulated flight endurance results at throttle speed (100% - 40%).....	126
Table 24.	Simulation flight endurance results at throttle speed (100% - 45%).....	127
Table 25.	Simulation flight endurance results at throttle speed (100% - 50%).....	128
Table 26.	Simulation flight endurance results at throttle speed (100% - 55%).....	129
Table 27.	Simulation flight endurance results at throttle speed (100% - 60%).....	130
Table 28.	Simulation flight endurance results at throttle speed (100% - 65%).....	131
Table 29.	Simulation flight endurance results at throttle speed (100% - 70%).....	132
Table 30.	Simulation flight endurance results at throttle speed (100% - 75%).....	133
Table 31.	Simulation flight endurance results at throttle speed (100% - 80%).....	134
Table 32.	Simulation flight endurance results at throttle speed (100% - 85%).....	135
Table 33.	Simulation flight endurance results at throttle speed (100% - 90%).....	136
Table 34.	Simulation flight endurance results at throttle speed (100% - 95%).....	137
Table 35.	Simulation flight endurance results at throttle speed (100%).....	138
Table 36.	Simulation flight endurance results—with and without solar array incorporated.....	140

EXECUTIVE SUMMARY

Unmanned aerial vehicle (UAV) systems have been used by many armed forces worldwide for the past 60 years, and these systems have progressed into advanced and highly capable machines to support reconnaissance, surveillance, and target acquisition (RSTA); surveillance for peacetime and combat synthetic aperture radar (SAR); maritime operations and battle damage assessment (BDA) missions. UAV systems can be broadly classified by their performance characteristics such as engine type, weight, speed, and endurance. In regards to RSTA, UAVs support missions at the strategic, operational, and tactical levels for decision-making in battle. Extension of the endurance of electric mini-UAVs at the tactical decision-making level is the focus of this thesis.

The concept and design of the mini-UAV class has been fine-tuned to an unmanned system that is lightweight, man-portable, hand-launchable, and capable of carrying video and data transmission payloads. Because of these specific features, a mini-UAV must be lightweight and made of tough materials and designed for quick assembly and disassembly during field deployment. The low radar cross-section area, low infrared signature, low acoustic signature, superior relative performance insensitive to operating altitude and temperature, and stealthy signature of mini-UAVs make them suitable for most missions. Nevertheless, one of the main drawbacks faced today is the flight endurance, which is directly limited by the on-board battery capacity. The other key drawbacks are the weight and size of the mini-

UAV, which restrict the mounting of larger payloads or extra batteries. Since mini-UAVs are mainly used for RSTA missions, it is not advisable to add extra weight to the ground reconnaissance team and carry more batteries intended for mini-UAV operations.

Related thesis work has demonstrated the extension of flight endurance through the implementation of thin-film photovoltaic cells. The objective of this thesis is to further investigate the viability of extending flight endurance by complementing the battery source on-board the mini-UAV using advanced thin-film photovoltaic (TFPV) cells, which are made of Copper-Indium-Gallium Di-Selenide semiconductor materials. The TFPV cells used are theoretically rated at 13% efficiency, which is the highest for a single-junction photovoltaic cell based on current technology.

In order to achieve a higher efficiency, a "2-in-1" DC-to-DC converter with a maximum power point tracking (MPPT) device or function is incorporated in the system. This provides a desired output voltage and delivers maximum power from the TFPV cells to the battery and load. The DC-to-DC converter is required to convert the generated photovoltaic cells' output DC voltage to a suitable level for charging the battery. The charging process is then optimized by using the MPPT as a power-conditioning unit that automatically operates the photovoltaic cells at their maximum power point under all conditions when charging the battery. Beyond the application of existing TFPV cell technology, we have also extended our research on new high power/energy density batteries and fuel cells technologies,

as well as the potential benefit of applying less mature, high-efficiency photovoltaic cells to military UAVs.

The improvement of flight endurance will greatly benefit military units that use mini-UAVs for RSTA and BDA missions. First, the extended on-site mission time will allow a mini-UAV to monitor the targets-of-interest and their movement without losing contact. Next, the number of UAV takeoffs and landings will be reduced; hence, minimizing the risk of damaging the mini-UAV. This translates to lower operational cost and shorter operational turn-around time. Damage is reduced mainly because the flexible photovoltaic cells do not break easily during the hard landing associated with mini-UAV recovery, as compared to brittle rigid cells. Last, the other spare aircraft wing covered with TFPV cells can be used to charge up any small electronic handheld equipment or the exhausted mini-UAV's battery after flight.

THIS PAGE INTENTIONALLY LEFT BLANK

LIST OF ACRONYMS AND ABBREVIATIONS

AFC	Alkaline Fuel Cell
AH	Amperes-Hour
AM	Air mass
AM0	Air mass 0
AM1.5	Air mass 1.5
a-Si	Amorphous Silicon
C/E	Capacity/Energy
CdS	Cadmium Sulfide
CdTe	Cadmium Telluride
CIGS	Copper-Indium-Gallium Di-selenide
COTS	Commercial Off-The-Shelf
DC	Direct-Current
DoD	Department of Defense
DLC	Double Layer Capacitor
DMFC	Direct Methanol Fuel Cell
EO	Electro-Optical
FES	Flywheel Energy Storage
FF	Fill Factor
GCS	Ground Control Station
HAE	High Altitude Endurance
IAI	Israel Aerospace Industries
IDF	Israel Defense Force
ISC	Short-Circuit Current
ISR	Intelligence, Surveillance, and Reconnaissance
Li-Ion	Lithium Ion
Li-Po	Lithium Polymer
Li-S	Lithium Sulfur Battery
LO	Low-Observable
Mo	Molybdenum

MP	Maximum Power
MCFC	Molten Carbonate Fuel Cell
m-PEFC	Micro-Polymer Electrolyte Fuel Cells
Mini-UAV	Miniature Unmanned Aerial Vehicle
MOUT	Military Operations in Urban Terrain
MPPT	Maximum Power Point Tracker
Na	Sodium
Ni-Cd	Nickel-Cadmium
NI-MH	Nickel-Metal-Hydride
NRL	Naval Research Laboratory
PAFC	Phosphoric Acid Fuel Cell
PEM	Polymer Electrolyte Membrane
PV	Photovoltaic
RC	Radio-Controlled
RFC	Regenerative Fuel Cell
S	Sulfur
SOC	State-of-Charge
SOFC	Solid Oxide Fuel Cell
TFPV	Thin-Film Photovoltaic
TFSC	Thin-Film Solar Cell
UAV	Unmanned Aerial Vehicle
Vo	Output Voltage
VOC	Open-Circuit Voltage
WH	Watt-Hour

ACKNOWLEDGMENTS

First, I would like to express my utmost gratitude to the most important person in my life, my wife Gloria. Thank you for your unwavering support throughout the long hours and difficult times. Because of your support, this journey has been an enjoyable experience.

Second, I am thankful to my thesis advisor, Dr. Sherif Michael for imparting valuable knowledge and guiding me through my research. His thorough knowledge on this subject was definitely vital to the successful accomplishment of this thesis work. I would also like to express my appreciation to my second reader, Dr. Rudolf Panholzer. His expertise on this subject was indeed helpful to accomplish my thesis.

I would like to thank Dr. James Calusdian, Mr. Ronald Phelps, Jeff Knight, Warren Roger, George Jaksha, and Jim Scrofani for their help and support to complete my thesis.

Additionally, I would like to thank Mr. Samuel Thompson and members of the Science & Technology Advanced Systems Unmanned Systems Activity at the Naval Air Warfare Center Weapons Division in China Lake, California, for funding the project.

Finally, I would like to thank the Singapore Defence Science & Technology Agency for giving me this opportunity for professional development and pursuing higher education at the Naval Postgraduate School.

THIS PAGE INTENTIONALLY LEFT BLANK

I. INTRODUCTION

A. BACKGROUND

Unmanned Aerial Vehicles (UAVs) have been widely accepted and incorporated into the armed forces of most nations. The application of UAV systems has proven to have a great impact and has resulted in significant mission utility in reconnaissance, surveillance, and target acquisition (RSTA) and battle damage assessment (BDA). One of the salient advantages of UAVs is that they can be flown without an on-board pilot during military exercises or operations. In addition, UAVs have distinctive traits that make them highly effective in specialized operations where risks to pilots are high. Due to this very fact, UAV systems are generally much less expensive and less complex for production, and this also makes equipping the troops with UAVs more viable at the battalion level and below. Besides procurement costs, training costs are much less expensive, and the scope of training soldiers to operate UAV systems has also been streamlined and made simpler in comparison to manned aircraft systems.

In general, UAVs can be classified as shown in Table 1. It is noted that the category Tier I is also known as Tactical UAV, Tier II as Operative UAV, Tier II Plus as Strategic High Altitude Endurance (HAE) UAV, and Tier III Minus as Strategic Low-Observable (LO) HAE UAV [1].

Table 1. UAV tier classification and characteristics.
(After [1])

Category	Designation	Max Alt	Radius	Speed	Endurance
Tier I	Interim Medium Altitude, Endurance	Up to 15,000 ft	Up to 250 km	60-100 knots	5 to 24 hrs
Tier II	Medium Altitude, Endurance	3,000 ft to 25,000 ft	900 km	70 knots cruise	More than 24 hrs
Tier II Plus	High Altitude, Endurance	65,000 ft max	Up to 5,000 km	350 knots cruise	Up to 42 hrs
Tier III Minus	Low Observable - High Altitude, Endurance	45,000 ft to 65,000 ft	800 km	300 knots cruise	Up to 12 hrs

Pertaining to this thesis, we focus on extending the endurance of electric mini-UAVs, which are considered in the Tier I category.

Mini-UAVs are well accepted and regularly deployed at the company level. Their light weight and small size offer full man-portability, which affords easy, quick assembly and launch for surveillance missions. However, one of the upsetting limitations is the flight endurance, capped by the battery capacity on-board. This endurance is usually limited between 60 to 90 minutes, after which the aircraft must be retrieved to recharge or replace the exhausted battery. To preserve the traits of an organic and highly portable mini-UAV system, it is not feasible to extend the flight endurance by adding more batteries. Therefore, as a

technology demonstration, solar cells are considered to extend the flight endurance by augmenting the existing on-board battery.

B. OBJECTIVE

To extend the flight endurance of a mini-UAV, the focus of this thesis is on using Thin-Film Photovoltaic (TFPV) cells made of Copper-Indium-Gallium Di-Selenide (CIGS) semiconductor materials to augment power on board the mini-UAV. Being flexible in nature, the CIGS TFPV cells are also light weight with a high efficiency. Without having to increase the overall aircraft take-off weight significantly, the solar cells are capable of providing an alternative source of power for flight missions. In addition, a direct-current (DC) to direct-current power converter which includes a Maximum Power Point Tracking (MPPT) device or function will be incorporated to optimize the output power from the solar cells. The MPPT achieves its objective by tracking the maximum operating power point and converting the varying input DC voltage (due to varying sunlight irradiance level at different times of the day) to match the output battery voltage.

Various energy storage and fuel cell technologies are also explored and possible options to maximize energy stored on-board and to achieve optimal output performance in a cost-effective way are considered.

One of the paramount tasks carried out in this thesis is software simulation. Simulation models are developed and

used to estimate the overall flight duration based on different throttle speed settings and output solar power levels.

Finally, the use of alternate UAV designs that incorporate larger wing surface area would clearly benefit from this approach due to the increase in the output power, along with better lift capability. With an improved lift-to-drag ratio, the mini-UAV requires lesser power to achieve a better climb and cruising performance. This in turn attributes to better power economy, hence extending the flight endurance.

C. RELATED WORK

A very recent solar-powered UAV, QinetiQ's Zephyr, beat the UAV endurance record on 17 July 2010, with an unmanned flight of 83 hours, 37 minutes. It was powered by the sun during the day and used its rechargeable lithium-sulphur batteries for night flight [2]. The aim of this research is to implement a similar concept using flexible solar cells to extend flight endurance for military operations. This is an extension of previous work conducted at the Naval Postgraduate School where flexible solar cells were implemented for mini-UAV applications [3].

D. APPROACH

First, the suitability and advantages of various new and existing energy storage and fuel cell technologies are explored. The intent is to optimize energy storage and usage on-board through the identification of highly efficient energy storage and fuel cell systems for mini-UAV applications.

Next, the aim is to maximize the capture of solar energy through the use of solar cells. Prior to actual implementation of the final solar array, the efficiency of existing CIGS TFPV cells are ascertained through experiments conducted under natural sunlight. With the experimental CIGS TFPV cell data, a full-scale solar array is designed and customized. This solar array is subjected to final simulation and testing before mounting onto a modified Raven mini-UAV wing.

E. ORGANIZATION

The various types of mini-UAV systems, focusing on system capabilities and the possibility of implementing solar cell applications to these systems, are covered in Chapter II.

The various energy storage technologies are explored in chapter III. It is highly desirable to identify suitable and highly efficient energy storage systems that offer both high specific energy and power density to extend and sustain UAV flight missions.

Various fuel cell technologies are explored and suitable high energy and high power density sources for extending the flight endurance of UAV missions are identified in Chapter IV.

Greater detail on applicable solar cell technologies and power devices, including the working principles of solar cells, maximum power point trackers, and DC-to-DC power converters, is presented in Chapter V.

Experimental testing methods and preliminary test results are presented in Chapter VI. It also covers the design and customization work of the final solar array, as well as presenting the final system integration for simulation and testing, are also presented.

The simulation and testing methods and results are presented in Chapter VII.

The conclusions, and makes recommendations for future research are presented in Chapter VIII.

II. MINI-UAV SYSTEMS

Mini-UAVs have been used by many armed forces, mainly for RSTA and BDA missions. These missions involved deploying mini-UAVs where important video imagery and data telemetry are transmitted from the mini-UAV back to the main headquarters via the ground reconnaissance team. These missions usually require the mini-UAVs loiter on-site as long as possible to perform surveillance. Because of limitations in weight and size, the energy source on-board must provide sufficient power to sustain flight for every mission.

The different types of mini-UAVs, namely the Tracker, Raven RQ-11B, Desert Hawk, Draganfly Tango, Aladin, Skylark, Scan-Eagle, Skylite B, Puma, and Skyblade III are reviewed in this chapter. The key intention is to identify their system capabilities and the importance of using large wings surface area for solar cell applications to extend flight endurance by complementing the on-board battery power. In the next few chapters, topics on energy storage, fuel cells, and photovoltaic cell technologies are discussed.

A. TRACKER

The Tracker, which is also known as Drone de Renseignement Au Contact (DRAC), is a hand-launched mini-UAV system that can be quickly assembled and made ready for operation within 15 minutes. The Tracker mini-UAV system can be transported in a man-portable backpack and deployed by two men. To maximize the flight endurance, the mini

aircraft uses a twin-boom sail-plane configuration and is powered by a small electric motor located in a pod over the wing. In regards to mission, the mini-aircraft is capable of performing over-the-hill intelligence, surveillance and reconnaissance (ISR), battle damage assessment, tracking, identification, and classification tasks. Each system is comprised of two mini-aircrafts with payloads, a data link and a portable ground control station. The mini-aircraft can remain on-station up to 1.5 hours at a maximum range of 10 km away from the ground control station. It is flown autonomously using GPS-based navigation, and real-time telemetry data can be continuously transmitted back to the ground control station. One of the main advantages of this system is the mini aircraft's ability to perform auto landing during recovery, and this minimizes human mishandling during landing [4].

On 25 January 2010, EADS Defence & Security delivered 35, specially modified, new UAV DRAC systems to the French Army to enhance its capabilities in mountainous terrain. The new batch follows a first batch of 25 DRAC systems delivered to the Ministry of Defence in July 2008 [5]. A brief overview of the Tracker mini-UAV system capabilities is shown in Table 2. A photograph of the mini-UAV is shown in Figure 1.

Table 2. Overview of Tracker mini-UAV system capabilities.
(After [4])

Wingspan	3.4 m
Length	1.4 m
Maximum take-off weight (MTOW)	8.3 kg
Maximum operating altitude	1980 m (6500 ft)
Maximum flight endurance	75-90 minutes
Maximum operating speed	60 to 90 km/h
Maximum operating range	Up to 10 km



Figure 1. Tracker mini-UAV. (From [6])

B. RAVEN RQ-11B

The Raven RQ-11B is an organic mini-UAV system that is tactically operated at the US Army battalion, company and platoon levels. The mini-UAV system is highly man-portable, and each system is comprised of three mini-aircrafts, a ground control station, video and telemetry antenna systems, batteries and other ground support equipment. Weighing only 2 kg, the mini-aircraft can be easily hand-launched after a quick ground assembly of a few minutes by a two-man team. The mini-aircraft can be manually operated or programmed for autonomous flight operation via the ground control station. In regards to missions, the Raven is capable of performing reconnaissance, surveillance, and

target acquisition, force protection and convoy security, battle damage assessment, and Military Operations in Urban Terrain (MOUT), which provide crucial and direct support to battalion-level activities and below. The maximum operating range is 10 km, and the mini-aircraft can be recovered via belly landing by going into a deep stall mode [7].

The Raven RQ-11B mini-UAV has proven its combat capabilities in supporting the U.S. operations in Iraq and Afghanistan and other areas of conflict. It is also in service in all of the U.S. military services and the U.S. Air Force is also procuring the Raven mini-UAV to replace the Desert Hawk mini-UAV [8]. A brief overview of the Raven RQ-11B capabilities is shown in Table 3. A photograph of the mini-UAV is shown in Figure 2.

Table 3. Overview of Raven RQ-11B mini-UAV system capabilities. (After [7])

Wingspan	1.4 m (4.5 ft)
Length	0.9 m (3 ft)
Power plant	Electric Motor, rechargeable lithium ion batteries
Maximum take-off weight (MTOW)	1.91 kg (or 4.2 lbs)
Maximum operating altitude	14000 ft
Maximum flight endurance	Approximately 90 minutes (using rechargeable battery)
Maximum speed	32-81 km/h (or 17-44 knots)
Maximum operating range	10 km



Figure 2. Raven RQ-11B mini-UAV. (From [9])

C. DESERT HAWK

Desert Hawk III is an autonomous mini-UAV system deployed for real-time, operational day/night, situational awareness and airborne intelligence, surveillance and reconnaissance, including covert missions. The system is comprised of a mini-aircraft, a portable touch-screen ground control station, payloads and a remote video terminal. The system is mainly designed for man-portability with quick, real-time mission planning and flight profile re-tasking capability. Due to its lightweight, the mini-aircraft can be hand-launched after a quick assembly of 10 minutes and can be recovered using skid landing. The current model has a greater operational range and longer endurance than its predecessor versions.

One of the main advantages of the Desert Hawk mini-UAV system is its low aural and visual signature. When airborne, the mini-aircraft is almost inaudible from a range of 150 meters, which is ideal for covert operations, without compromising surveillance techniques or endangering the safety of the ground reconnaissance team. Additionally,

the mini-aircraft is able to focus on a target without having to alter course for re-targeting as it uses a 360-degree rotating electro-optical or infrared camera sensor payload. A brief overview of Desert Hawk III mini-UAV system capabilities and a picture of the mini-UAV are shown in Table 4 and Figure 3, respectively [10].

Table 4. Overview of Desert Hawk III mini-UAV system capabilities. (After [10])

Wingspan	137 cm (54 in)
Length	91 cm (36 in)
Maximum take-off weight (MTOW)	4 kg (8.5 lbs)
Maximum operating altitude	731 m (2400 ft)
Maximum flight endurance	90 minutes
Maximum speed	30-50 knots
Maximum operating range	Up to 15 km



Figure 3. Desert Hawk III mini-UAV. (From [11])

D. DRAGANFLY TANGO

The Draganfly Tango is a radio-controlled (RC) mini-UAV capable of shooting high-resolution video and photographs over large areas for surveillance missions. The mini-aircraft is quickly assembled, can either be hand launched or bungee launched, and can be flown manually by

an external pilot. An enhanced model allows the mini-UAV to fly with a GPS-guided autopilot for long range and high altitude missions and includes real-time telemetry data that can be transmitted back to the ground control station. This mini-aircraft is probably one of the lowest cost systems in this class due to the simplicity of its system design and its basic RC operation mode [12].

The main advantages of this system are its large surface area (double) wings, low cost and light weight, which make it a suitable candidate for this thesis research. The maximum flight endurance for the basic model is approximately 50 minutes. A brief overview of Draganfly Tango mini-UAV system capabilities and a picture of the mini-UAV are shown in Table 5 and Figure 4, respectively.

Table 5. Overview of DraganFly Tango mini-UAV system capabilities. (From [12])

Wingspan	1.5 m
Length	1.2 m
Wing area	5625 cm ²
Motor	500 Watt brushless DC electric motor
Maximum take-off weight (MTOW)	3.94 kg (inclusive of maximum payload weight 1.14 kg)
Maximum operating altitude	731 m (2400 ft)
Maximum flight endurance	50 minutes (at 2.8 kg) using one Li-Polymer battery. Possible 4 hours using extremely efficient brushless motor and high capacity Li-Po battery.
Maximum speed	60 mph (100 km/h)
Cruising speed	25 mph (40 km/h)
Stall speed	15 mph (24 km/h)
Maximum operating range	Up to 10 miles (autonomous flight control)

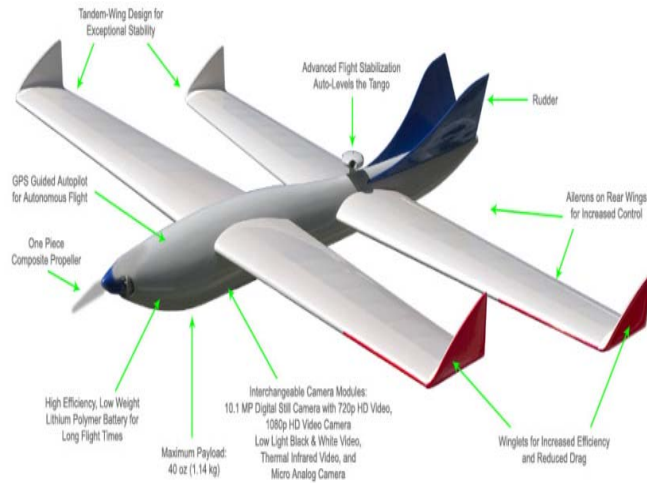


Figure 4. DraganFly Tango mini-UAV. (From [12])

E. ALADIN

The Aladin is an easy to operate, high performance mini-UAV system developed by EMT in Germany. The system is comprised of two mini-aircrafts that can be flown autonomously via a ground control station. For deployment, the mini-aircraft is quickly assembled within a few minutes and can either be hand or bungee launched. The maximum flight endurance is approximately 60 minutes. The mini-aircraft is well-suited for immediate, on-demand reconnaissance flights providing detailed intelligence, surveillance and reconnaissance data for real-time missions. In regards to flight intelligence, the mini-aircraft flight position is permanently monitored by an autonomous collision avoidance system in the ground control station using digital mapping either in 2-dimensional or 3-dimensional mode.

One of the key advantages of the mini-aircraft is its low detectability. It is difficult to detect the aircraft visually, aurally or by radar due to its small size,

noiseless electric engine and composite material structure. A brief overview of mini-aircraft system capabilities and a picture of the mini-aircraft are shown in Table 6 and Figure 5, respectively [13].

Table 6. Overview of Aladin mini-UAV system capabilities.
(From [14])

Wingspan	1.46 m
Length	1.57 m
Battery	Lithium-Ion Polymer battery, 14 V, 9 Ah
Maximum take-off weight (MTOW)	3.18 kg (7 lbs)
Maximum operating altitude	4500 m
Maximum flight endurance	30-60 minutes
Maximum speed	70 km/h
Maximum operating range	5-10 km



Figure 5. Aladin mini-UAV. (From [15])

F. SKYLARK

The Skylark mini-UAV system is comprised of three aircrafts, a ground control station, and both day and night payloads. The system is man-portable and can be operated by two soldiers. The mini-aircraft, which weighs only 4.5 kg, can be hand-launched, and it is exceptionally quiet due to its electric propulsion system. During recovery, the mini-

aircraft performs a deep stall maneuver to land safely on a small inflatable cushion located on the belly to protect the payload.

The Skylark mini-UAV is well suited for many missions such as close range, over-the-hill surveillance and reconnaissance and law enforcement. The mini-aircraft is flown autonomously, and real-time continuous video and telemetry data can be continuously fed back to the ground control station. Skylark is capable of achieving a flight endurance of approximately 1.5 hours with a maximum range of 5-10 km.

In December 2008, the Israel Defense Force (IDF) selected an enhanced version of Elbit System's Skylark mini-UAV, called the Skylark 1LE, for operation at the battalion level [16].

The new Skylark 1LE configuration offers many enhancements over the original Skylark. First, the maximum flight endurance has increased from 1.5 hours to 3 hours. Next, the operational altitude can range between -700 ft to +3000 ft above or below the takeoff point, the operational service ceiling capped at 15,000 ft, and the extended mission radius has also increased by 50-100% to maximum range of 15 km. In addition, the wingspan has increased from 2.2 meters to 2.9 meters.

Skylark II is an outgrowth of the Skylark mini-UAV system, currently operational with several armies. The 35 kg vehicle has a wingspan of 4.2 meters and is designed to perform 6-hour missions at a maximum range of up to 50 km. The vehicle is powered by a new 4-kilowatt electrical motor

and driven by a battery pack contained in the payload pod underneath the main boom. The propulsion system is comprised of a dual-channel permanent magnet brushless motor and a driver/controller [17]. A brief overview of Skylark, Skylark 1LE, and Skylark II mini-UAV system capabilities and a picture of the Skylark mini-UAV during system setup are shown in Table 7 and Figure 6, respectively.

Table 7. Overview of Skylark mini-UAV system capabilities. (From [18], [19])

	Skylark	Skylark 1LE	Skylark II
Wingspan	2.4 m	2.9 m	4.2 m
Length	2.2 m	Not Available.	Not Available.
Maximum take-off weight (MTOW)	5.5 kg	6.1 kg (day configuration) 6.3 kg (night configuration)	43 kg (95 lbs), including payload 10kg (22 lbs)
Maximum operating altitude	Not Available.	15000 ft	15000 ft
Maximum flight endurance	1.5-2 hours	3 hours	6 hours by 4 kW electric engine
Maximum speed	20-40 knots	37-54 knots (70-100km/h)	Not Available.
Maximum operating range	5-10 km	Up to 15 km	Up to 50 km



Figure 6. Skylark mini-UAV. (From [20])

G. SCAN-EAGLE

The Scan-Eagle mini-UAV is powered by a tail-mounted, two-stroke, gasoline-fueled, commercial off-the-shelf (COTS) model aircraft engine and carries a maximum of 4.3 kg of fuel. Due to its 18 kg take-off weight, it must be launched from a pneumatic catapult and can be recovered automatically by a "SkyHook" system, where a rope hanging from a 15 m pole catches the mini-aircraft. An alternate conventional land recovery can be used in an open area of 100 ft by 600 ft. Equipped with an on-board differential GPS-based navigation system, the mini-aircraft is capable of performing autonomous waypoint navigation, object tracking and in-flight route mapping. The ground control station can control up to eight mini-UAVs for full force operation. Because the mini-aircraft is powered by a gasoline engine, it is able to achieve an endurance of more than 15 hours while operating at a maximum altitude of 4880 meters.

The entire mini-aircraft can be disassembled and packed into a single man-portable bag (1.71 m x 0.45 m x 0.45 m) prior to transition to a new area of operation. One of the key strengths is its ability to operate in cold environments. This is because the mini-aircraft is equipped with carburetor heating and an ice-phobic wing covering. The nose, which carries the pilot tube, can also be fitted with an anti-precipitation system for cold weather operation. With regard to missions, the Scan-Eagle mini-UAV is capable of performing intelligence, surveillance and reconnaissance, special services operations, escort operations, sea-lane and convoy protection, and protection of high-value and securing installations. A brief overview of the Scan-Eagle mini-UAV system capabilities and a picture of the mini-UAV operating from land or sea are shown in Table 8 and Figure 7, respectively [21].

Table 8. Overview of Scan-Eagle mini-UAV system capabilities. (From [22])

Wingspan	3.1 m (10.2 ft)
Fuselage diameter	0.18 m (7 in)
Length	1.19 m (3.9 ft)
Propulsion	3W 2-stroke piston engine; 1.1 kW (1.5 hp)
Empty weight	12 kg
Maximum take-off weight (MTOW)	18 kg (40 lbs)
Maximum operating altitude	16,000 ft (4876 m)
Maximum fuel	4.3 kg
Payload plus fuel weight	6 kg
Maximum flight endurance	20+ hours
Speed	55-80 mph



Figure 7. ScanEagle mini-UAV. (From [21])

H. SKYLITE B

The Skylite B mini-UAV is a follow-up design of its predecessor, the canister-launched Skylite A UAV. The new enhanced version is redesigned with a V-tail shape, a larger wingspan, and more powerful batteries. The SkyLite B mini-UAV is launched using a lightweight catapult and can be deployed to support field units at the battalion level and below, including special forces. With regard to aircraft recovery, the mini-aircraft is retrieved by soft landing with the assistance of a parachute and inflatable airbag to minimize hard landing impact. After landing, the mini-aircraft can be returned to an immediate flying condition by replacing the exhausted battery and parachute and folding the airbag. By using lithium-polymer batteries as the only source of on-board power, the flight endurance time can be extended up to 90 minutes. Controlled by the ground control station, the Skylite B can perform autonomous flight operations based on planned course missions. From a system perspective, the mini-UAV is

capable of providing real-time, quality intelligence, continuous tracking of static targets, and even directing a combat force to its target [23].

The SkyLite B mini-UAV system is designed to meet a variety of operational requirements by switching between different aircraft configurations. The mini-UAV system has an enhanced version where extended endurance is achieved by modifications to the battery and the wing tips of the basic UAV design. One of the key strengths of the SkyLite B is its ability to perform under harsh weather conditions and at high winds speed of up to 30 knots. A brief overview of SkyLite B mini-UAV system capabilities and a picture of the mini-UAV are shown in Table 9 and Figure 8, respectively [24].

Table 9. Overview of Skylite B mini-UAV system capabilities. (After [24])

	Standard Version	Enhanced Version
Wingspan	2.4 m (7.9 ft)	2.4 m (7.9 ft)
Fuselage diameter	12 cm (4.7 in)	12 cm (4.7 in)
Length	1.25 m (4 ft)	1.25 m (4 ft)
Maximum take-off Weight (MTOW)	6.4 kg (13.6 lbs)	8 kg (17.6 lbs)
Maximum operating altitude	100-600 m (300 to 2000 ft)	100-600 m (300 to 2000 ft)
Maximum flight endurance	>90 minutes	>150 minutes
Maximum speed	37-54 knots (70-100 km/h)	37-54 knots (70-100 km/h)
Maximum operating range	10 km (7.5 miles)	>35 km (>21.7 miles)



Figure 8. Skylite B mini-UAV. (From [23])

I. PUMA

The Puma mini-UAV is a man-portable system that is slightly larger than the Raven. Due to its light weight, the mini-UAV can be hand launched. The mini-aircraft is typically flown autonomously, controlled by the ground control station. The mini-aircraft is deployed to support a variety of missions, such as extended duration surveillance, light infantry military operations on urbanized terrain. The innovations with the most impact of the Puma mini-UAV are its ability to land on both land and water and the ability to survive near-vertical deep stall landing approaches.

The Aqua Puma mini-UAV is an innovated version of the Puma system for use in salt water environments. It can be landed directly onto the sea surface and recovered using any small watercraft. It is approximately 1 kg heavier than the original Puma model, and the flight endurance is approximately 30 minutes shorter. This capability greatly benefits special operations involving river infiltration and where the landing zone is constrained to very tight areas on land. Additionally, with these landing

capabilities, the Puma mini-UAV is capable of being deployed from various watercraft without modification or installation of extra landing gear on-board the deployment vessel. Another big innovation is its sensor system. Other mini-UAV systems tend to have micro-cameras that can be moved by the operator to pan, tilt, or zoom, but the Puma has a camera that is fully stabilized to fix on a designated point and provide a steady, constant image that compensates for aircraft movement [25][26]. A brief overview of Puma mini-UAV system capabilities and a picture of the mini-UAV operating from land or sea are shown in Table 10 and Figure 9, respectively.

Table 10. Overview of Puma mini-UAV system capabilities.
(After [27],[28])

Wingspan	2.8 m
Length	1.4 m
Propulsion	600 W DC electric motor
Maximum take-off weight (MTOW)	5.9 kg
Maximum operating altitude	12,500 ft
Maximum flight endurance	2 hours
Maximum speed	25-60 km/h
Maximum operating range	15 km



Figure 9. Puma mini-UAV. (From [29])

J. SKYBLADE III

The Skyblade III mini-UAV system is designed for rapid mission deployment to support both military and civilian applications. In terms of military applications, the Skyblade III mini-UAV is mainly used for reconnaissance, surveillance, and target acquisition and battle damage assessment missions. Like other mini-UAVs, the Skyblade III has an advanced surveillance capability and is capable of delivering quick and accurate real-time intelligence, supporting both day and nighttime missions. One of the key advantages of this system is its modularity, which allows it to incorporate a variety of payloads [30].

The Skyblade III mini-UAV is a fully autonomous aircraft. The mini-aircraft is hand launched and can be controlled by both an external pilot (for close range flight) and a ground control station. For pre-flight planning, the ground control station offers maximum convenience, allowing the ground reconnaissance team to upload pre-planned routes and has the flexibility of altering route commands on the fly as required. The maximum operating range is 8 km with a flight endurance between 60 and 90 minutes. A brief overview of the Skyblade III mini-UAV system capabilities and a picture of the mini-UAV are shown in Table 11 and Figure 10, respectively.

Table 11. Overview of Skyblade III mini-UAV system capabilities. (After [30])

Wingspan	2.6 m
Length	1.4 m
Maximum take-off weight (MTOW)	5 kg
Maximum operating altitude	300 - 1,500 ft (90- 460 m)
Maximum fuel	5.4 kg
Maximum flight endurance	>60 minutes
Maximum speed	35 knots
Maximum operating range	8 km



Figure 10. Skyblade III mini-UAV. (From [31])

K. CHAPTER SUMMARY

Various mini-UAV systems such as the Tracker, Raven RQ-11B, Desert Hawk, Draganfly Tango, Aladin, Skylark, Scan-Eagle, Skylite B, Puma, and Skyblade III were discussed in this chapter. For each system, generic system capabilities were tabulated as well as the physical dimensions of each aircraft. In determining the optimal system for this thesis research, an aircraft with large wing surface area must be chosen. Also, to provide adequate

flight endurance, a system with adequate solar cell output power must be chosen to complement the on-board battery.

In the next chapter, the different types of energy storage technologies are discussed.

III. ENERGY STORAGE TECHNOLOGIES

For UAV systems, it is imperative to consider all possible options to maximize the energy stored onboard and achieve the optimal output performance in a cost-effective way. Any weight that can be shed from the system aids in extending the endurance of the UAV by requiring less power for flight. This additional energy can either be diverted to provide propulsion power or provide power for onboard avionics operations, such as video imagery and modem telemetry transmission to the ground control station.

Energy storage devices provide the ability to store some form of energy that can be drawn upon at a later time to carry out some useful operation. There are currently more than ten types of energy storage technologies that have been discovered and employed. Typically, each energy storage technology includes a power conversion unit to convert the energy from one form to another.

There are two primary factors that characterize the application of an energy storage technology. The first factor is the amount of energy that can be stored in the device. This is a characteristic of the storage device itself. The second factor is the rate at which energy can be transferred into or out of the storage device. This mainly depends on the peak power rating of the power conversion unit, and is also impacted by the response rate of the storage device itself [32].

The advantages and essentiality of utilizing energy storage systems outweigh the disadvantages and technical

challenges associated with them. One of the key benefits of storing energy is that it allows people to balance the supply and demand of energy in their daily lives, especially when energy availability is limited. A relevant example is the battery used for providing propulsion power and avionics on-board a mini-UAV. It is highly desirable to have a battery source that offers both high specific energy and power density to sustain UAV flight missions for extensive periods of time.

Several common energy storage technologies that can be considered for mini-UAV applications, such as sodium-sulfur batteries, lithium-sulfur batteries, lithium-ion and lithium-polymer batteries, nickel-cadmium batteries, nickel-metal hydride batteries, flywheels, and ultra-capacitors are identified in this chapter. Additionally, a review of the advantages and drawbacks for each of the technology is presented.

A. SODIUM-SULFUR BATTERY (NA-S)

The sodium-sulfur battery is a type of molten metal battery constructed from sodium (Na) and sulfur (S). The sodium-sulfur battery has a high energy density, up to three times that of a lead-acid battery, high efficiency (89-92%) and does not suffer from self-discharge. Additionally, it has a long cycle life, more than 2500 full charge/discharge cycles, a shelf life of up to 15 years, and a peak pulse power capacity up to five times nominal.

Though the sodium-sulfur battery has a high energy density, a major drawback is that the battery operates at temperatures between 300C and 350C. This temperature range

is well beyond the operating temperature range for UAV applications [33]. The internal composition of a sodium sulfur battery is shown in Figure 11.

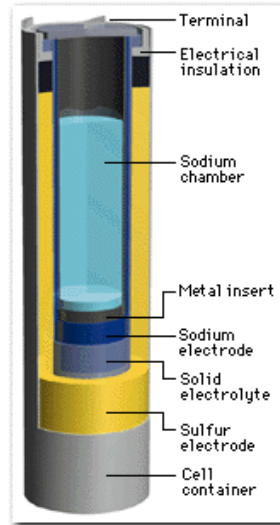


Figure 11. Sodium sulfur battery. (From [34])

B. LITHIUM SULFUR BATTERY

The lithium sulfur battery (Li-S) is a rechargeable galvanic cell with a very high energy density and Li-S cells may succeed lithium-ion cells because of their higher energy density and the low cost of sulfur. Research conducted at the University of Waterloo has produced lithium sulfur cells with 84% of the theoretical maximum energy density, potentially offering four times the gravimetric energy density of lithium-ion cells [35]. A common type of lithium sulfur battery is shown in Figure 12.

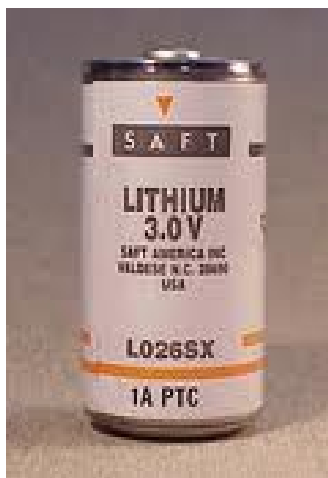


Figure 12. Lithium sulfur battery. (From [36])

1. Advantages and Drawbacks of Lithium-Sulfur Cells

The energy density of lithium-sulfur cells is estimated to be about 1200 Wh/kg, and that is about three to five times greater than a conventional lithium-ion battery. Another advantage is that the production of the raw materials used for lithium-sulfur batteries is cheaper than that for lithium-ion batteries.

One of the key issues faced by lithium-sulfur cells is capacity fading, which is also coupled with lower volumetric energy. Additionally, the final cost of production is also highly dependent on the optimization of materials and battery configuration.

A major drawback of lithium-sulfur batteries is in terms of safety. Lithium-sulfur batteries typically employ a negative electrode comprised of metallic lithium. If the electrode is not adequately protected by a passivating

layer, there could be safety concerns [37]. Also, lithium-sulfur batteries are typically limited to a maximum of 100 charging cycles.

Despite these drawbacks, QinetiQ's Zephyr has recently beat the record for an unmanned flight of 83 hours, 37 minutes flown as a solar-powered UAV where it powers off the sun during the day and prepares its rechargeable lithium-sulfur batteries to last for the night flight due to the high energy density [2].

C. LITHIUM ION (LI-ION) AND LITHIUM POLYMER (LI-PO) BATTERY

Lithium-ion and lithium polymer batteries are essentially the same, except that the lithium-polymer battery is technologically more advanced than the lithium ion battery. Cells sold today as lithium polymer batteries are pouch cells, and unlike, lithium-ion cylindrical cells, which have a rigid metal case, pouch cells have a flexible, foil-type (polymer laminate) case.

It is of great interest not to overcharge a lithium polymer battery. Charging voltages of more than 4.235 volts per cell (when used in a series combination), may cause explosion or fire. Similarly, during a load discharging cycle, the load has to be removed as soon as the voltage drops below approximately 3.0 volts per cell (when used in a series combination). If the load is not removed, the battery will subsequently no longer accept a full charge and may experience problems holding voltage under load in the future. Fortunately, this can be avoided by incorporating circuitry that prevents overcharge and deep

discharge [38]. To prolong the lifespan of the battery pack with multiple cells, it is necessary to incorporate cell balancing during the charging cycle; otherwise, the capacity of the battery pack will be limited to the capacity of the weakest cell. Balance charging means that the charger monitors the voltage of each cell in a pack and varies the charge on a per-cell basis so that all cells are brought to the same voltage. It is also important to note that trickle charging is not acceptable for lithium batteries.

Lithium polymer batteries are becoming more popular due to their lower weight and greatly increased cycle life. However, lithium polymer batteries have a greater cycle life degradation rate than lithium ion batteries, such that their charging cycles are typically capped at 100. For storage purpose, lithium polymer batteries can be stored for one or two months without significantly losing charge as compared to other types of batteries where significant loss of charge occurs during similar storage conditions. For long-term storage it is recommended that the battery be discharged to 40% of its full charge. A common type of lithium polymer battery is shown in Figure 13.



Figure 13. Lithium polymer battery. (From [39])

1. Advantages and Limitations of Lithium Battery

Lithium batteries have a high cell voltage of 3.6 volts, a high energy density (about four times greater than lead acid), and a high power density. They are small in size, low in weight, and can be easily optimized for specific capacity ratings. Lithium batteries also have a low self-discharge rate, and they can be kept in storage for a very long time. Another added advantage is that they are not subject to memory effects.

In general, individual lithium polymer cells are more than 20% lighter than equivalent lithium ion cells due to the absence of a strong metal casing. Additionally, they are approximately three times lighter than nickel cadmium and nickel-metal-hydride batteries.

Despite the many advantages, internal resistance increases with both cycling and age. This causes lithium batteries to have higher internal impedance than nickel cadmium or nickel-metal hydride batteries. Similar to other batteries, lithium cell capacity diminishes over time. Increases in internal resistance reduce the cell's ability to deliver output current, thus older batteries do not charge as much as new ones. Lithium batteries also degrade at high temperatures and serious degradation occurs when the cell is discharged below two volts. When overcharged, they will experience capacity loss or thermal runaway [40].

D. NICKEL-CADMIUM (NI-CD) BATTERY

The nickel-cadmium battery was invented in 1899, and at that time materials were expensive compared to those of other battery types; therefore, the use of the nickel-

cadmium battery was limited to special applications. Eventually, enhancements were made to the nickel-cadmium battery, and these advances led to the modern sealed nickel-cadmium battery that is in use today. Nickel-cadmium batteries work better with a fast charge as opposed to a slow charge or with a pulse charge (to facilitate fast charging and prevent overheating during charging process) as opposed to a DC charge. In fact, nickel-cadmium is the only battery type that performs well under rigorous working conditions. All other batteries work better with a shallow discharge and moderate load currents. The nickel-cadmium battery should not dock in a charger for multiple days and is not well-suited for brief periods of occasional use. A periodic full discharge is so important that, if omitted, large crystals will form on the cell plates (also referred to as memory), and the nickel-cadmium battery performance will gradually degrade. Among rechargeable batteries, nickel-cadmium remains a popular choice for two-way radios, emergency medical equipment and power tools. There is a shift towards batteries with higher energy densities and less toxic metals, but alternative chemistries cannot always match the superior durability and low cost of nickel-cadmium [41]. A common type of nickel-cadmium battery is shown in Figure 14.



Figure 14. Nickel-cadmium battery. (From [42])

1. Advantages and Limitations of Nickel-Cadmium Battery

Nickel-cadmium batteries make use of fast and simple charge, even after prolonged storage. Additionally, they typically last longer than other rechargeable batteries and can provide up to 1000 charge/discharge cycles if properly maintained. When compared to lead-acid batteries, nickel-cadmium batteries offer a much higher energy density. They are also considerably smaller and lighter than comparable lead-acid batteries. In cases where size and weight are important considerations, as in the case of UAV applications, nickel-cadmium batteries are preferred over cheaper lead-acid batteries. They are also one of the most rugged rechargeable batteries, able to tolerate deep discharge for long periods of time. For long-term storage purposes, nickel-cadmium batteries are usually stored fully discharged.

In contrast to lithium ion batteries, nickel-cadmium batteries are less stable and are permanently damaged if discharged below a minimum voltage [43].

Nickel-cadmium batteries have a higher capacity, are less toxic, and are more cost effective than nickel-metal hydride batteries. Nickel-cadmium batteries are also more economically priced and are lowest in terms of cost per charging cycle. They also come in a wide variety of sizes and performance options. Although nickel-cadmium cells may cost more and have a lower capacity than that of alkaline cells, they have a significantly longer total lifetime because of the non-reversible chemical reaction in alkaline batteries.

The primary disadvantage of nickel-cadmium batteries is their high cost when compared to lead-acid batteries. This is because they are composed of costly nickel and cadmium materials. Another disadvantage is that nickel-cadmium batteries exhibit a high negative temperature coefficient. The result is that as battery cell temperature rises, the internal resistance falls. The reduction in the battery internal resistance poses considerable charging problems. Another major disadvantage is that nickel-cadmium batteries suffer from memory effects if they are discharged and recharged to the same state of charge hundreds of times. The memory effect manifests itself when the battery remembers the point in its charge cycle where recharging began and exhibits a sudden drop in voltage at that point after subsequent use, as if the battery had been discharged. In a mini-UAV, the consequence of this memory effect may result in the sudden loss of power and control, possibly leading to an unintended crash. To prevent memory effect build-up, the battery must be periodically exercised through full discharge/charge cycles. These batteries are also considered environmentally unfriendly because they contain toxic metals. Finally, a major limitation is this type of battery's high self-discharge ability, which requires recharging after storage.

E. NICKEL-METAL-HYDRIDE (NI-MH) BATTERY

The research on nickel-metal-hydride system started in the 1970s as a means of storing hydrogen for the nickel hydrogen battery, and nickel hydrogen has been mainly used for satellite applications in today's technology. Technology advancements in 1980s permit the development of

new stable hydride alloys for use in a cell, and since then, nickel-metal hydride batteries have steadily improved [41]. A common type of nickel metal hydride battery is shown in Figure 15.



Figure 15. Nickel-metal-hydride battery. (From [44])

High energy density and the use of environmentally friendly metals have driven the success of nickel-metal-hydride batteries. Modern nickel-metal-hydride batteries offer up to 40% greater energy density than standard nickel-cadmium batteries. Although there is potential for higher capacities, there are some negative side effects associated with this increase where cycling under heavy load and storage at high temperature reduces service life, which makes them less durable than nickel-cadmium batteries. They also suffer from high self-discharge, which is higher than that of nickel-cadmium batteries.

Limitations remain, although nickel-metal-hydride batteries have made significant improvements over the years. In fact, most shortcomings are native to nickel-based battery technologies and are shared with nickel-cadmium batteries. Based on technological advancements in

nickel-metal-hydride battery performance, it is widely accepted in industry that nickel-metal-hydride is an interim step to lithium-based battery technologies.

1. Advantages and Limitations of Nickel-Metal-Hydride Battery

Nickel-metal-hydride batteries typically have 30-40% higher capacity than standard nickel-cadmium batteries and the potential for higher energy densities is technically feasible. Nickel-metal-hydride batteries are also less prone to the memory effect as compared to nickel-cadmium batteries and require fewer exercise cycles to prevent this effect. Nickel-metal-hydride batteries are also environmentally friendly and only contain mild toxins which can profitably be recycled.

However, nickel-metal-hydride batteries have limited service life, and their performance starts to deteriorate after 200-300 cycles if repeatedly deep-cycled. The storage life is relatively short, lasting only up to three years. The discharge current is usually limited to prevent reduction in the battery's cycle life, despite the fact that it is capable of delivering high discharge currents to heavy loads. To maintain a healthy battery status, the battery must not be overcharged; hence, trickle charge settings become critical and charging algorithms also become more complex. Due to its chemical properties, nickel-metal-hydride batteries suffer from a high self-discharge phenomenon, which is approximately 50% higher than in nickel-cadmium batteries and nearly ten times worse than lead-acid or lithium batteries. Nickel-metal-hydride batteries are also sensitive to external temperatures and

should be stored in a cool place at 40% state-of-charge. At elevated temperatures, performance begins to degrade [41].

F. FLYWHEEL

The basic working principle behind flywheel energy storage (FES) is accelerating a flywheel to extremely high speeds and subsequently maintaining the energy in the system as rotational energy. The stored energy is given by $E = 0.5I\omega^2$ and is proportional to the flywheel's mass moment and the square of its rotational speed. The moment of inertia is given by $I = kmr^2$ and depends on the initial constant, radius, mass, and height (or length) of the flywheel (rotor). In the charging state, the flywheel is usually spun up by a motor supplied with external electrical energy (which can come from an AC source, battery source or solar panel), and during discharge (slowing of the flywheel), the same motor acts as a generator, whereby it produces electricity from the rotational energy of the flywheel and supplies power to the load. When energy is required and extracted from the system, the flywheel's rotational speed is reduced due to the principle of energy conservation.

Technology advancements have led to the development of micro-energy storage systems using a flywheel energy storage system with a high temperature superconductor bearing. Currently, micro flywheel technology is not fully mature. Recently, a micro flywheel with a diameter of 50 mm was shown to achieve a maximum rotational speed of

51,000 rpm at 12 V and 0.68 A. At this speed, the flywheel stored a rotational kinetic energy of 337 J, which is close to 0.093 WH [45].

Most flywheels are capable of several hundred thousand full charge-discharge cycles, enjoying a much better cycle life than battery technologies. Flywheels also offer very high cycle efficiencies, reaching over 90%. Since the stored energy in a flywheel system is dependent on the size and speed of the rotor, and the power rating is dependent on the motor-generator, power and energy can be determined independently. Some common types of flywheels are shown in Figure 16.



Figure 16. Example of Flywheels used in energy storage systems. (From [46])

1. Advantages and Limitations of Flywheel

DC flywheel energy storage systems are generally more reliable than batteries. They typically cost more than batteries but have significantly longer equipment lives and lower annual operation and maintenance expenses. Flywheel energy storage systems also exhibit a much higher power density than batteries, typically by a factor of five to ten [47].

Flywheel energy storage systems can also operate over a wide temperature range, between 0C and 40C, and are neither temperature dependent nor affected by temperature changes as compared to chemical rechargeable batteries. They do not suffer from memory effect and can also be recharged quickly after use. Another advantage of flywheel energy storage systems is that it is possible to calculate the exact amount of energy stored by a simple measurement of the rotational speed [48].

The amount of energy a flywheel can store is limited by how fast it can rotate. However, a flywheel is restricted such that it cannot rotate at a speed faster than its material's density and strength can support. The strength of the material divided by the density of the material is known as specific strength. It is important to note that when the tensile strength of a flywheel is exceeded, it can cause the flywheel to shatter and release all of its stored energy immediately. This phenomenon is known as "flywheel explosion" since wheel fragments can reach a kinetic energy that is comparable to that of a bullet. Fortunately, composite materials used for construction of flywheels tend to disintegrate quickly once broken instead of producing large chunks of high-velocity shrapnel. The next limitation is that traditional flywheel systems require strong containment vessels as a safety precaution, which increases the total mass of the device.

G. ULTRA-CAPACITOR OR SUPER-CAPACITOR

An electrochemical capacitor has components related to both a battery and a capacitor. Ultra-capacitors, also known as super-capacitors are being developed as an

alternative to pulse batteries. An attractive alternative, super-capacitors have a higher power and much (at least one order of magnitude higher) longer shelf and cycle life than batteries. The downside is that super-capacitors have a much lower energy density than batteries, and their low energy density, in most cases, is the factor that determines the feasibility of their use in a particular high power application.

Super-capacitors are different than normal capacitors, because they are able to hold a much greater charge. Therefore, the potential is greater, and the total energy stored can be much higher. Super-capacitors resemble regular capacitors except that they offer very high capacitance in a small package. There are three types of electrode materials suitable for super-capacitors. They are high surface area activated carbons, metal oxide, and conducting polymers. The high surface area electrode material, also called a double layer capacitor (DLC), is the least costly to manufacture and is the most common. The lifetime of super-capacitors is virtually indefinite, and their energy efficiency rarely falls below 90% when kept within design limits [49]. Some common types of super-capacitors are shown in Figure 17.

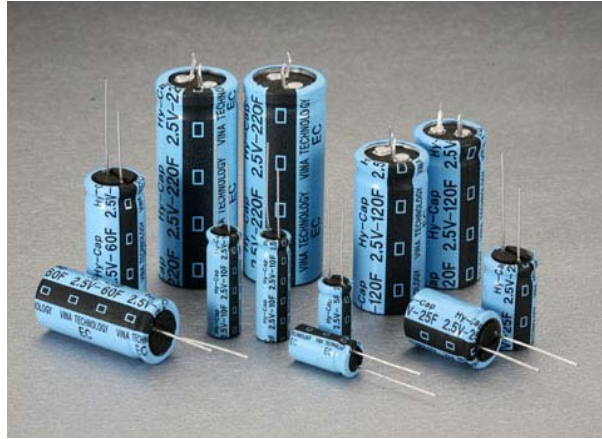


Figure 17. Super-capacitors. (From [50])

1. Advantages and Limitations of Super-Capacitors

Super-capacitors can be charged and discharged almost an unlimited number of times, and each charge or discharge can last milliseconds, tens of seconds or as long as several minutes [51]. Typically, a super-capacitor with a larger capacitance value can store more energy but requires a longer duration charge and discharge. A larger capacitance also corresponds to a larger and heavier size and weight. Super-capacitors have high power density (ranging from 10 to 100 kW/kg) but suffer from low energy density (ranging from 1 to 5 Wh/kg). The energy density is high in comparison to a regular capacitor but only one-tenth that of a nickel-metal-hydride battery. A super-capacitor does not release any thermal heat during discharge, and there is no danger of overcharging. When a super-capacitor reaches a fully charged state, it simply quits accepting a charge. Additionally, unlike a chemical battery, it is not affected by deep discharges, and, hence, enjoys a long lifetime, which reduces maintenance costs.

The operating temperatures for super-capacitors range between -50C and 85C, and storage capacity increases as temperature decreases below rated temperature. Similar to a standard capacitor, the voltage varies with the energy stored. The effective storage and recovery of energy in a capacitor requires complex electronic control and switching equipment, which will result in consequent energy loss. Evidence suggests that super-capacitors usually lose about 80% of their storage capacity after 10 years, with a lifetime estimated to be 20 years. It is also estimated that the DC-DC round-trip efficiency is 80-95 percent in most applications. However, the self-discharge of a super-capacitor is substantially higher than that of an electro-chemical battery. In about 40 days, the capacity can decrease from full charge to 50 percent. In comparison, a nickel-based battery discharges about 10 percent during that time. However, linear discharge voltage prevents use of the full energy spectrum, and because of this, super-capacitors are unable to deliver their full charge. For example, a 6 V battery is allowed to discharge to 4.5 V before the equipment cuts off; the super-capacitor reaches that threshold within the first quarter of the discharge cycle. The remaining energy slips into an unusable voltage range. Although a DC-to-DC converter could correct this problem, introducing such a regulator would add cost and incur a reduction of 10 to 15 percent in output efficiency [52]. It is also important to note that super-capacitor cells generally have low voltages, and serial connections are needed to obtain higher output voltages. Voltage balancing is further required if more than three super-capacitors are connected in series.

H. CHAPTER SUMMARY

Existing energy storage technologies such as sodium-sulfur batteries, lithium-sulfur batteries, lithium-ion and lithium-polymer batteries, nickel-cadmium batteries, nickel-metal-hydride batteries, flywheels, and ultra-capacitors were discussed in this chapter. The advantages and drawbacks were reviewed for each type of energy storage technology. From this review, it is evident that lithium-ion and lithium-polymer battery technologies are well suited for mini-UAV applications. This is primarily due to the high specific energy density and the reasonable specific power density exhibited by these batteries. A summary and comparison of these energy storage technologies is shown in Table 12.

In the next chapter, the different types of fuel cell technologies are discussed.

Table 12. Comparison table between various types of energy storage systems. (After [53],[54])

Energy Storage	Charge / Discharge Time	Operating Temperature	Operating Voltage	Capacitance	Life	Specific Power Density	Specific Energy Density	Efficiency	Self-Discharge Rate
Sodium sulfur battery	Not Available.	300C to 350C	Voc: 2.08V per cell	Not Available	More than 2500 cycles	Up to 0.05 kW/kg	Typical 90-120 Wh/kg. As high as 250 Wh/kg.	0.89-0.92	No self discharge
Lithium sulfur battery	1.5 to 2hours	-60C to +60C	Nonlinear in the range 2.5-1.7V per cell	Not Available	Up to 100 cycles	TBC	350 - 600 Wh/kg	0.65	< 15% per month
Li-Ion	3 to 5hours	-20C to +60C	3.6 / 3.7 V per cell	Not Available	400-1200 cycles	~0.25~0.34 kW/kg	100-250 Wh/kg	0.8-0.9	8% -31% per month (temperature dependent)
Li-Po	~1.5hours	-20C to +60C	3.7 V per cell	Not Available	>1000 cycles	Up to 7.1 kW/kg	130-200 Wh/kg	0.998	Up to 5% per month
Ni-Cd	8hours	-40C to +60C	1.2V per cell	Not Available	Up to 2000 cycles	0.15 kW/kg	40-60 Wh/kg	0.70-0.90	High, 20% per month
Ni-Mh	6hours	-20C to +60C	1.2V per cell	Not Available	Up to 1000 cycles	0.25 - 1.0 kW/kg	30-80 Wh/kg	0.66	High, 30% per month

Supercapacitors	Milliseconds to Seconds	-40C to +85C	2.3V - 2.75V per cell	100 mF to >2F	>500,000 cycles	10 to 100 kW/kg	1 to 10 Wh/kg	0.85-0.98	Much higher than rechargeable batteries
Flywheel	Not Available.	0C to +40C	Not Available.	Not Available	No limits, long overall life time	To Be Confirmed	Approx. 0.01 kWh/kg	>0.95	To Be Confirmed

THIS PAGE INTENTIONALLY LEFT BLANK

IV. FUEL CELL TECHNOLOGIES

One of the major technical challenges encountered by UAVs today is increasing flight endurance, which is directly limited by on-board battery or fuel capacity. Since additional batteries cannot be added or refuelling cannot occur during flight operations, it is necessary to incorporate high energy density power sources to extend the flight endurance of UAVs.

In the preceding chapter, various energy storage systems were discussed. Energy storage systems based on fuel cell technologies are focused on in this chapter. Broadly, fuel cells can be described as either primary or not rechargeable, or secondary or regenerative. The primary fuel cells discussed in this chapter are polymer electrolyte membrane, direct methanol, alkaline, phosphoric acid, molten carbonate, and solid oxide fuel cells. Besides these, the latest developments in regenerative fuel cell technologies are explored. Additionally, the advantages and drawbacks associated with both the primary and secondary fuel cells are discussed.

Similar to a battery, a fuel cell uses stored chemical energy to generate power. It produces electricity from an external fuel supply as opposed to the limited internal energy storage capacity of a battery. In simple terms, a fuel cell is an electrochemical device that converts hydrogen fuel directly into electricity and heat without combustion. A typical fuel cell contains an anode and a cathode insulated by an electrolyte situated between them. Hydrogen is supplied to the anode while oxygen is supplied

to the cathode. These two gases are attracted to one another, but because of the electrolyte, the hydrogen atoms are split into protons and electrons. The protons pass freely through the electrolyte. The electrons take a different path, creating an electric current before recombining with the hydrogen and oxygen, creating water molecules. This chemical process generates electrical and thermal energy but produces pure water as a by-product [55].

The significant advantage of a fuel cell is that it combines the clean and quiet attributes of a battery with the refueling capabilities of an internal combustion engine. The typical power output from a single fuel cell is between 0.5-0.7 V under load with power operating densities of more than 300-400 mW/cm². Additionally, a number of fuel cells can also be connected in series to achieve optimal power output. A diagram showing the basic operation of a common type of fuel cell is shown in Figure 18.

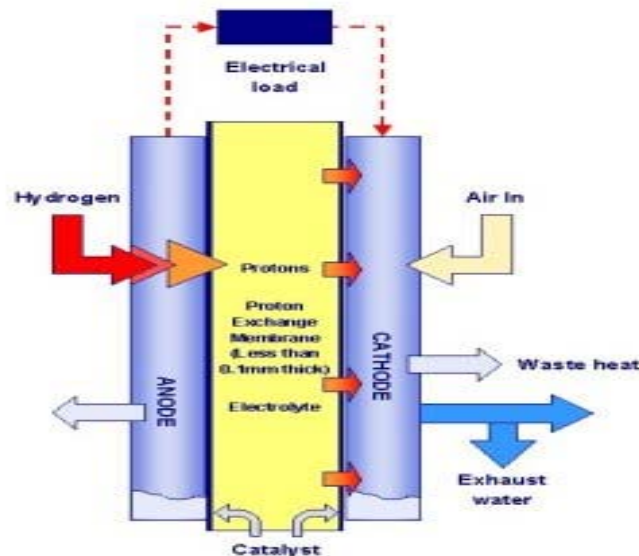


Figure 18. Basic operation of a fuel cell. (From [56])

Fuel cells offer numerous advantages over conventional power generation systems, such as high energy density, high efficiency, low noise, low pollution, minimum transmission losses, modularity and fuel flexibility [57].

A. POLYMER ELECTROLYTE MEMBRANE (PEM) FUEL CELLS

Polymer electrolyte membrane fuel cells, also called proton exchange membrane fuel cells, are capable of delivering high-power density and offer the advantages of low weight and volume compared with other fuel cells. These cells need only hydrogen, oxygen from the air, and water to operate. This fuel cell's chemistry requires no corrosive materials as in other fuel cell types. PEM fuel cells are typically fueled with pure hydrogen supplied from storage tanks. Due to their fast start-up time, high efficiency of 40-60%, and favorable power-to-weight ratio, conventional PEM fuel cells are well suited for use in transportation and stationary applications.

Despite these superior properties, PEM fuel cells operate at around 80C, which is considered high for typical mini-UAV's operation. PEM fuel cells also have low energy densities. Because PEM fuel cells run on hydrogen, problems of fuel storage and refueling must be considered, which discourage their use in UAV applications despite their low cost, efficiency and reliability. The other drawback is that there are some instances where 80C is not high enough to perform useful cogeneration. Additionally, for more effective operations, the electrolyte must be saturated with water, which may be considered "dead weight" on-board a mini-UAV. These limitations must be carefully considered prior to using PEM fuel cells.

On 23 August 2010, Israel Aerospace Industries (IAI) successfully integrated a hydrogen proton exchange membrane fuel cell system into the Bird-Eye 650 mini-UAV. This extended the flight endurance of the system to six hours, more than doubling its endurance with lithium batteries [58]. The benefits of using hydrogen fuel cells to power UAVs have also been shown by the Naval Research Laboratory (NRL) with its Ion Tiger UAV. With this system, NRL set an unofficial flight endurance record of 26 hours, 1 minute while carrying a 5-pound payload [59]. These cases of extended flight endurance demonstrate that hydrogen PEM fuel cells are extremely efficient and capable of meeting and surpassing the performance of traditional power systems. This makes PEM fuel cells an attractive solution in extending the flight endurance of mini-UAVs.

Recently research on the development of micro-polymer electrolyte fuel cells (m-PEFC) was evaluated in terms of power, energy and efficiency [60]. Although fabricated micro PEM fuel cells deliver a limited power density of 92 WL^{-1} and an overall efficiency of 263 WL^{-1} , they can be assembled compactly and operate at low temperatures. Because of these major advantages, micro polymer electrolyte fuel cells may meet the stringent operating criteria, in terms of physical size and volume, of mini-UAV operations. A picture of a PEM fuel cell stack is shown in Figure 19.

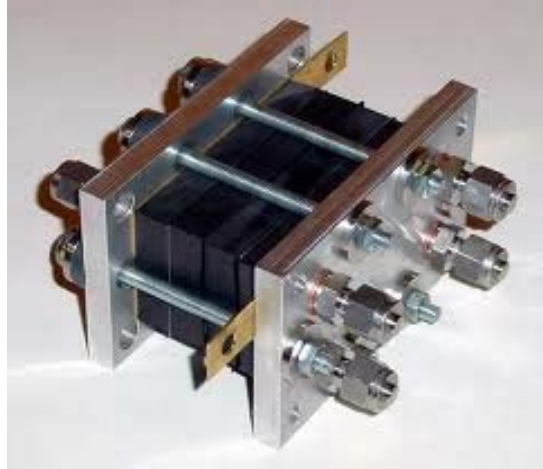


Figure 19. PEM fuel cell stack. (From [61])

B. DIRECT METHANOL FUEL CELLS

The direct methanol fuel cell (DMFC) is a type of proton-exchange fuel cell in which methanol is used as the fuel. DMFCs use methanol fuel to carry the reactant into the cell with typical operating temperatures in the range of 50C to 120C. A DMFC works by relying on the oxidation of methanol on a catalyst layer to form carbon dioxide, where water is consumed at the anode and subsequently produced at the cathode. Protons are then transported across the proton exchange membrane to the cathode where they react with oxygen to produce water. Electrons are transported through an external circuit from anode to cathode, thus providing power to connected devices [62]. Of secondary note, the efficiency of DMFCs is fairly low when operating at low temperatures.

Methanol has a lower energy density than gasoline or diesel fuel but has a higher density than hydrogen. Therefore, direct methanol fuel cells have less significant fuel storage problems than other fuel cell types. Also,

methanol is easier to transport. Because DMFCs use liquid fuel for power, the requirement for fuel reforming and on-board hydrogen storage is eliminated in contrast to PEM fuel cells. With a higher energy density than hydrogen, DMFCs use a simpler system design, with the potential for lower fuel volume and lightweight packaging. This translates into lower overall system weight and volume. Due to the chemical reaction process, DMFCs are near zero-emission power systems, with only small amounts of water and carbon dioxide as output products.

Despite the many advantages of DMFCs, there are some limitations and drawbacks associated with this fuel cell technology. First, the efficiency is lower than that of PEM fuel cells due to the slower methanol reaction rate and multi-stage reaction process. Because methanol is a liquid, it also poses a higher fire risk in open spaces when compared to hydrogen. Also, DMFCs are fueled by methanol which is considered toxic. In fact, exposure to methanol can cause blindness and birth defects as it attacks the optic nerve and destroys fetal tissue. It is of particular concern to humans because it can enter the body through ingestion, inhalation, or absorption through the skin; therefore, those handling methanol without gloves or respiratory protection risk exposure that may cause permanent damage. Furthermore, chronic exposure over time can be fatal [63].

The fabrication and characterization of silicon-based direct methanol micro fuel cells was reported in [64]. These fuel cells were able to achieve power densities up to 2.65 mW/cm² at open circuit voltage of 0.15 V, with a concentration of 2M methanol solution under lab test

conditions. Although there has been steady progress in advancing direct methanol micro fuel cell technologies, the limitations and risks associated with using methanol fuel have not been fully addressed. A picture of a micro direct methanol fuel cell is shown in Figure 20.

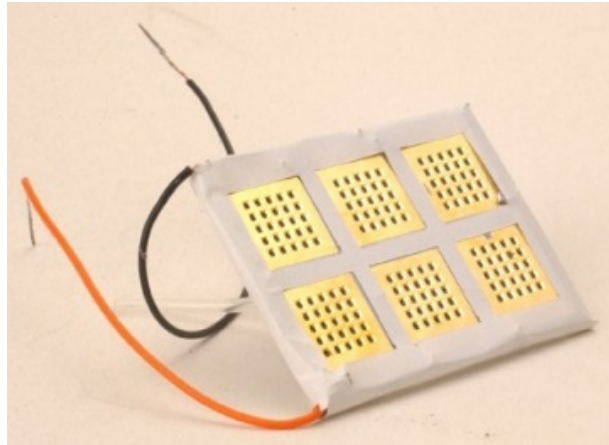


Figure 20. Micro direct methanol fuel cell. (After [65])

C. ALKALINE FUEL CELLS

Like PEM fuel cells, alkaline fuel cells (AFC) operate on pure hydrogen but have a lower power density. The theoretical efficiency of alkaline fuel cells is better than that of PEM, where an alkaline fuel cell can have an electrical efficiency ranging from 50% to 60% (for space applications). Alkaline fuel cells also demonstrate very high performance because of the fast chemical reaction that takes place in these fuel cells. However, typical alkaline fuel cells operate at high temperatures, between 100C and 250C. Fortunately, newer AFC designs operate at lower temperatures, from approximately 23C to 70C, which is more suitable for mini-UAV applications.

One key disadvantage of this fuel cell type is that alkaline fuel cells are very susceptible to carbon dioxide

contamination. In fact, a very small amount of carbon dioxide can contaminate and significantly degrade a cell's operation. For these fuel cells to operate properly, carbon dioxide must be removed from the fuel cell reaction. Hence, the decontamination process of purifying the hydrogen and oxygen can drive up the fuel cell system cost [66].

D. PHOSPHORIC ACID FUEL CELLS

Phosphoric acid fuel cells (PAFC) are considered the "first generation" of modern fuel cells. Although phosphoric acid fuel cells are one of the most mature cell types and the first to be used commercially, they may not be suitable for mini-UAV applications due to their high operating temperature. They have an operating temperature of approximately 150C to 200C. At this high operating temperature, these fuel cells are typically used for stationary power generation, but some are also used to power large vehicles, such as city buses. The electrical efficiency for phosphoric acid fuel cell ranges from 37% to 42%, while the efficiency of co-generation of electricity and heat can be as high as 85% [67].

Phosphoric acid fuel cells are only slightly more efficient than combustion-based power plants. Also, they are less powerful than other fuel cells having the same weight and volume. Therefore, these fuel cells are typically large, heavy and expensive.

E. MOLTEN CARBONATE FUEL CELLS

Molten carbonate fuel cells (MCFC) are high-temperature fuel cells that use an electrolyte composed of a molten carbonate salt mixture suspended in a porous, chemically inert ceramic matrix of beta-alumina solid electrolyte [68].

In terms of operation, molten carbonate fuel cells are not susceptible to contamination by carbon monoxide or carbon dioxide. This enables molten carbonate fuel cells to make use of carbon oxides as fuel sources, making them suitable for fueling with gases made from coal. As such, molten carbonate fuel cells are currently being developed for natural gas and coal-based power plants for electrical utility, industrial, and even military applications. These fuel cells are capable of achieving about 60% efficiency, which is much higher than the 37% to 42% efficiency of phosphoric acid fuel cells.

Despite a high efficiency, MCFCs are disadvantaged by their high operating temperature of 650C and above, which renders them unsuitable for mini-UAV applications. Other disadvantages of MCFCs are their poor durability and limited lifespan. These are due to high operating temperatures and the use of corrosive electrolytes, both of which accelerate component breakdown and corrosion [69].

F. SOLID OXIDE FUEL CELLS

A solid oxide fuel cell (SOFC) is made up of four layers, three of which are ceramics. A single cell consisting of these four layers stacked together is

typically only a few millimeters thick. Hundreds of these cells are then connected in series to form a "SOFC stack" [70].

Similar to MCFCs, solid oxide fuel cells operate at very high temperatures, typically between 500C and 1000C. Due to these high operating temperatures, hydrogen is produced through a catalytic reforming process, eliminating an external reformer for hydrogen production. High operating temperatures also pose challenges to the fuel cell materials' durability. Other disadvantages are slow startup operation and the requirement for significant thermal shielding to retain heat and protect personnel. Further, these temperatures make SOFCs unsuitable for mini-UAV applications. However, there is utility for these cells as auxiliary power units in vehicles and in stationary power generation applications.

Additionally, SOFCs are resilient to carbon monoxide catalyst poisoning, enabling them to use gases made from coal [71]. Although SOFCs are sulfur-resilient, they are still vulnerable to sulfur poisoning at higher sulfur concentrations. For proper operation, sulfur must be removed before entering the cell. The theoretical efficiency of converting fuel to electricity of a solid oxide fuel cell device can reach 60%.

G. REGENERATIVE OR REVERSIBLE FUEL CELLS

Regenerative fuel cells (RFC), also known as reversible fuel cells, are capable of producing electricity directly from the chemical reaction between hydrogen and oxygen. The by-products of the reaction are mainly heat and water. As

the name suggests, reversible fuel cell systems are capable of carrying out electrolysis, where electrical power harnessed from solar power or other energy sources is used to electrically split water into oxygen and hydrogen fuel [72]. The hydrogen gas is then stored and used to generate electricity when the renewable energy is not available. In a typical reversible fuel cell system, each cell is capable of operating both as a fuel cell and as an electrolyzer. The two-way chemical reaction process of a reversible fuel cell system is shown in Figure 21.

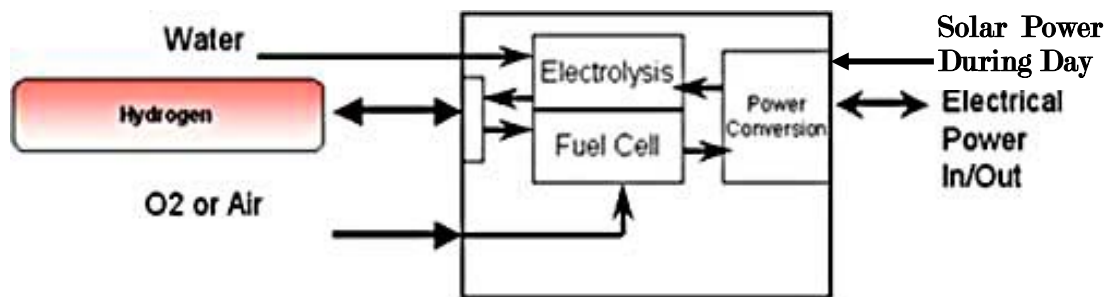


Figure 21. Electrolyzer and reversible fuel cell.
(After [73])

The main challenge of using regenerative fuel cells for mini-UAVs applications is space and weight constraints for on-board water storage, hydrogen production and hydrogen storage. Therefore, the entire regenerative fuel cell system becomes more complex than a typical primary fuel cell system.

Typically, RFCs exhibit a packaged specific energy density of 400 Wh/kg or more and are not susceptible to the self-discharge (near-zero) phenomenon. There are also no practical limitations on the depth of discharge, unlike rechargeable batteries. Due to the nature of regenerative

operation, the life span for these fuel cell systems is virtually unlimited. Additionally, the ability to electrically recharge RFCs by water electrolysis eliminates the need for fuel supply logistics [74].

H. CHAPTER SUMMARY

Both primary and regenerative fuel cell technologies and their advantages and disadvantages were reviewed in this chapter. Promising test results on micro polymer electrolyte membrane and micro direct methanol fuel cells were also presented. Further research and development on regenerative fuel cells could lead to useful mini-UAV applications but, when compared to primary fuel cell development, are still in their infancy. Some of the remaining challenges are meeting the size, space and weight constraints for water and hydrogen storage on-board these mini-aircraft.

In the next chapter, a basic introduction on solar cells and power devices is discussed.

V. SOLAR CELLS AND POWER DEVICES

A. INTRODUCTION

The idea of using natural energy, such as sun, wind, geothermal, and hydro power, and converting it into useful energy for commercial activities has been studied extensively over the last few decades. Currently, there is greater emphasis on the development of renewable energy sources for defense applications, especially with the depletion of fossil fuel supplies and the exponential growth in power demand.

Solar power, being the most readily available form of renewable energy is discussed at greater depth in this chapter, and includes discussion of p-n junctions, band-gap energy, the photovoltaic effect, factors affecting cell efficiency and the performance, degradation and encapsulation of flexible CIGS solar cells. Further discussions include topics on power devices such as DC-to-DC converters, maximum power point trackers, and battery balancer chargers.

There are three main elements necessary to understand solar cell manufacturing technologies. First, a semiconductor material is required to absorb incident light and convert the light energy into electron-hole pairs through chemical reaction. Next, a p-n junction is required to be formed in the semiconductor, where electrons diffuse from the n-type material to the p-type material and recombine with holes and vice versa. Third, electrical contacts are constructed at the top and bottom of the cell

to facilitate current flow to external circuits. Solar cells can be made of crystalline silicon in a wafer form and thin films of other materials [75].

Due to the high cost of crystalline silicon wafers, cheaper materials are being explored to construct solar cells. Copper-Indium-Gallium Di-selenide (CIGS), which is a type of semiconductor material, has become a realistic choice in the construction of low cost solar cells capable of providing reasonable power conversion efficiency. Other than its low cost and adequate power efficiency, CIGS solar cells exhibit flexibility, have high tolerance to sun radiation and are light weight, which make them well-suited for mini-UAV applications. However, CIGS solar cells are highly sensitive to air and water vapor, which degrade the efficiency of the cells over time.

In [76], scientists at the Swiss Federal Laboratories for Material Science and Technology demonstrated a record efficiency of 17.6% using flexible thin-film solar cells on polymer film. A single CIGS thin-film solar cell from Global Solar is shown in Figure 22.

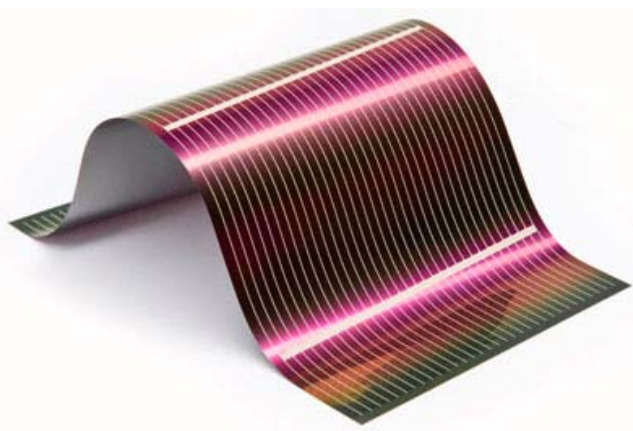


Figure 22. CIGS TFPV cell. (From [77])

B. SOLAR SPECTRUM AND SOLAR RADIATION

The electromagnetic spectrum consists of the entire range of frequencies or wavelengths at which electromagnetic waves can travel. The electromagnetic spectrum contains many types of electromagnetic waves, including radio waves, microwaves, infrared radiation, visible light, ultraviolet radiation, X-rays and gamma rays. Each type of electromagnetic wave has a unique characteristic wavelength (λ) and frequency (ν) [78]. The electromagnetic wave spectrum is shown in Figure 23.

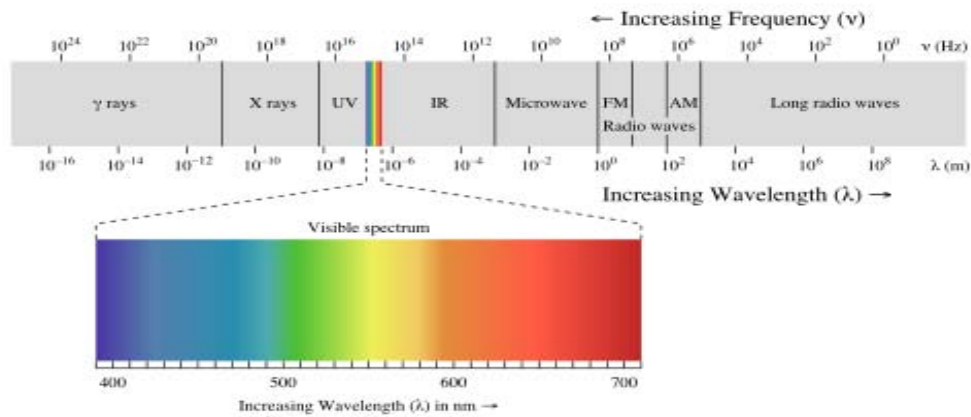


Figure 23. Electromagnetic spectrum. (From [79])

Solar energy, in the form of electromagnetic waves, is the solar radiation that traverses from the sun to the earth. This solar radiation is converted to useful energy by solar cells. Solar radiation, being part of the electromagnetic spectrum, consists of three components, visible light, infrared radiation, and ultraviolet light. Over 90% of solar radiation is visible light and near-infrared radiation, with the remaining being ultraviolet light.

1. Air Mass

Air mass (AM) refers to the distance light travels through the earth's atmosphere. When the sun is directly overhead (at zenith), the distance that light travels is assigned 1.0 (i.e., AM 1.0). When the angle of the sun increases from zenith, the air mass increases. When light travels a longer distance through the earth's atmosphere, there is more scattering and absorption of solar radiation by atmospheric constituents, such as air molecules, aerosols, and water vapor. Air mass zero (AM 0) which is considered the solar constant, describes solar irradiance in space that is unaffected by the atmosphere. It has a power density of approximately 1.350 KW/m^2 . The power density of AM 1.5 light is approximately 1.000 KW/m^2 (where solar zenith angle equals 48.19°). It is noted that the air mass and atmospheric conditions vary with specific geographic location and time of day and year. A diagram depicting air mass relative to incident angle of the sun is shown in Figure 24.

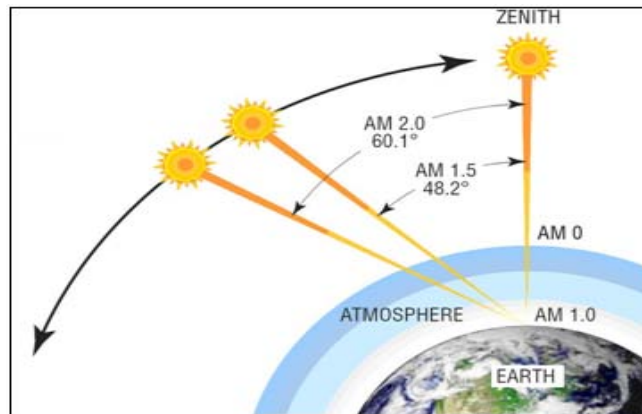


Figure 24. Air mass. (After [80])

C. SOLAR CELLS

A solar cell is a simple semiconductor device that converts light into electric energy. It is made from either a single crystal or crystalline or amorphous semiconductor materials. Solar cells consist of two types of material, usually a p-type silicon and n-type silicon. In fact, solar cells are semiconductor p-n junctions where light generates electron-hole pairs on both sides of the junction, i.e., in the n-type emitter and in the p-type base.

The power generated from a solar cell is determined by the type and area of the material used and the intensity and wavelength of the incident sunlight. For simplicity, the output power of a solar cell is considered directly proportional to the intensity of the sunlight.

Some important characteristics of solar cells include that cell output voltage is independent of cell size, is fairly constant with varying sunlight intensity, and decreases at a rate of 2 mV/C as temperature rises. On the contrary, cell current is relatively stable at high temperature and is directly proportional to sunlight intensity and cell-size. Therefore, in order to obtain a high output power, solar panels should be operated at lower temperatures with large cell-sizes connected individually. The best way to interpret the characteristics of a solar cell is to review its current-voltage (IV) curve, as shown in Figure 25.

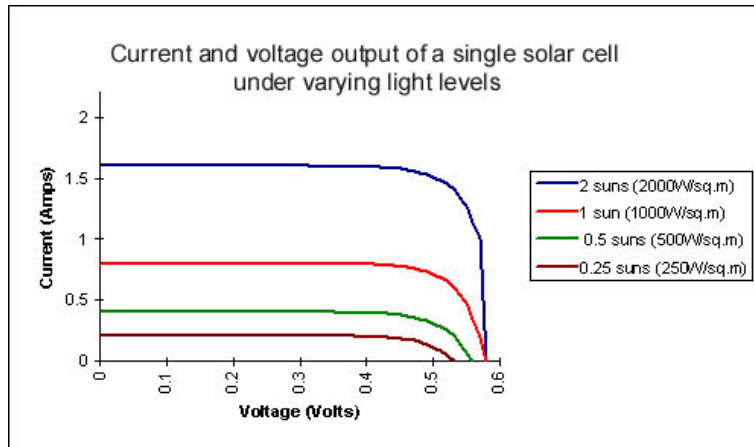


Figure 25. Current and voltage curve at different light intensities. (From [81])

The electrical characteristics of a solar cell are described by the following five parameters, namely the open-circuit voltage (VOC), short-circuit current (ISC), maximum power (MP), fill factor (FF), and energy conversion efficiency (η). The IV curve can be easily plotted by recording measurements of the VOC of a photovoltaic (PV) cell with an open circuit and the ISC with the end terminals of the cell electrically shorted. Load resistance is then connected to the cell and is varied from short to open circuit in order to characterize the complete IV response. It is important to note that the actual maximum power from a solar cell is less than the theoretical maximum power, which is the product of VOC and ISC. FF is defined as the degree to which the actual output is less than the theoretical maximum power and is computed from

$$FF = MP / (V_{oc} I_{sc}) = (V_{MP} I_{MP}) / (V_{oc} I_{sc}), \quad (5-1)$$

where V_{MP} and I_{MP} are the maximum voltage and current points whose product equals the maximum power.

Similarly, energy conversion efficiency measures the ability of a solar cell to convert electromagnetic light energy into electrical power. The maximum efficiency can be computed from

$$\eta = (V_{MP} I_{MP}) / (P_{incident_light} A), \quad (5-2)$$

where $P_{incident_light}$ is the power of incident photons (~ 100 mW/cm² for air mass 1.5), and A is the surface area of the solar cell (cm²).

1. P-N Junctions

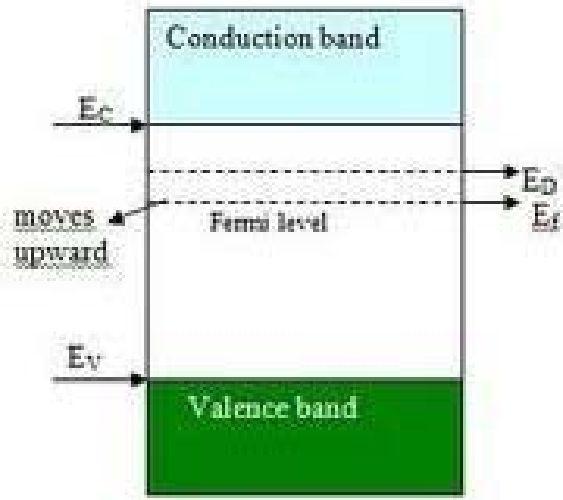
In the n-type silicon layer, free electrons are called majority carriers, whereas, the holes are called minority carriers. In the p-type silicon layer, holes are called majority carriers, whereas, the free electrons are called minority carriers. When the n-type and p-type silicon layers are joined, the majority free carriers (i.e., electrons and holes) diffuse across the layer and these majority carriers recombine with the minority carriers and are quickly swept away by the electric field, thereby creating a p-n junction.

The p-n junction is also called a depletion region because it is depleted of free carriers. When a free carrier electron or hole diffuses over to the p-type or n-type silicon layer, it leaves behind a positive charge or negative charge, thus, creating an electric field between the positive ion and the negative ion in the n-type layer and p-type layer, respectively. Therefore, the p-n junction separates carriers with opposite charges and transmits

electric current across the p-n junction when light hits the surface of the solar cell, thereby creating electron hole pairs.

2. Band Gap Energy

The band gap energy of a semiconductor is the minimum energy needed to free an electron from its bond in the crystalline structure. When a bond is broken, the electron gains sufficient energy to hop from the valence band to the conduction band. In order to free an electron, the photon energy must be at least equal to or greater than the band gap energy. However, photons with energy greater or equal to the band gap energy are required to free an electron. The valence band is the lower band of allowed states, and this band is almost fully occupied by electrons, especially at very low temperatures near 0 K where thermal activity ceases. These electrons will then absorb energy and leave the valence band and hop to the conduction band when temperature rises or if light photons are introduced. The conduction band is the upper band of allowed states, and this band is usually empty. It contains few or no electrons since energy is required for their transport from the valence band. Electrons in the conduction band are free carriers and they can move freely about the crystal [82]. A diagram of the band gap energy is shown in Figure 26.



E_D —→ Energy level of donor impurity

Figure 26. Band gap diagram. (After [83])

3. Photovoltaic Effect

The photovoltaic effect is the basic physical process through which a solar cell converts sunlight into electricity. When light photons strike the surface of a solar cell, the light may be reflected or absorbed, or it may pass through. The absorbed photons will generate electricity [84].

4. Factors Affecting Cell Efficiency

There are several factors affecting solar cell efficiency. The solar cell must be able to absorb a large part of the solar radiation. Dependent on the cell's absorption properties, most of the light is absorbed close to the surface. The surface of the solar cell is normally treated with an anti-reflection coating and surface texturing to reduce irradiance reflection. After treatment, only about 5% of the cell efficiency is lost as compared to 36% for an untreated cell. Low energy photons, which are

less than the energy gap, create heat instead of electron-hole pairs, and may also cause lower cell efficiency. However, photons with too much energy create electron-hole pairs but also increase cell temperature, which reduces the output voltage by 2 mV/C, leading to a reduction in cell efficiency. Additionally, internal recombination of electron-hole pairs reduces the output current and affects cell efficiency. Cell efficiency is further reduced by the resistance in the bulk of the base, surface, and junction contact and ohmic resistance in the metal contacts. Last, material defects and self-shading of electric conductors also reduces cell efficiency. A diagram of solar cell physical structure is shown in Figure 27.

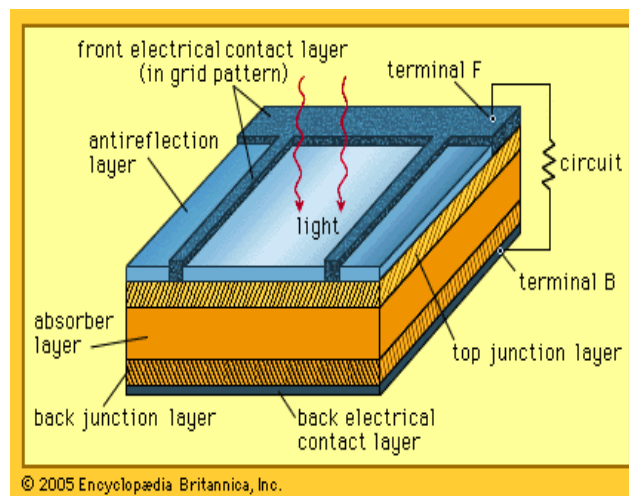


Figure 27. Solar cell structure. (From [85])

D. THIN-FILM SOLAR CELLS

Thin film solar cells consist of several layers of different materials in a thin-film form. These cells generally consist of five layers, namely the substrate, transparent conducting oxide, window layer, absorber layer

and the metal contact layer. Each of these component materials has different physical and chemical properties and each affects the overall performance of the solar cell.

For CIGS, the flexible substrate is a passive component in the solar cell. It provides mechanical strength to the solar cell, and it must match the thermal expansion coefficient of the next few layers.

For polycrystalline cadmium telluride (CdTe) and CIGS flexible cells, the back contacts are applied to the p-type semiconductor in both superstrate and substrate configurations. In order to form an ohmic contact, the metal used for contacts must have a work function greater than that of the p-type semiconductor. Molybdenum (Mo) is used as the contacting material in the substrate configuration of CIGS solar cells because of its relatively inert nature. During the highly corrosive CIGS deposition conditions, it forms an ohmic contact via the formation of a thin intermediate MoSe₂ layer formed during the CIGS deposition.

Generally, transparent conducting oxides are n-type degenerate semiconductors with good electrical conductivity and high transparency in the visible spectrum. This provides a low-resistance contact and ensures most of the incident light is absorbed by the absorber layer. The conductivity of a transparent conducting oxide depends on the carrier concentration and mobility.

The purpose of the window layer is to form a junction with the absorber layer while admitting the maximum amount of light into the junction region and absorber layer.

However, no photocurrent generation occurs in the window layer. CIGS solar cells typically use cadmium sulfide (CdS) for the window layer.

CIGS, which has a band gap energy of 1.53 eV, is considered an ideal material for photovoltaic application and is used for the absorber layer. It is one of the most absorbing semiconductor materials and makes an excellent junction and a solar cell [86]. A schematic of a typical process flow for preparing a monolithically integrated submodule CIGS flexible solar cell is shown in Figure 28.

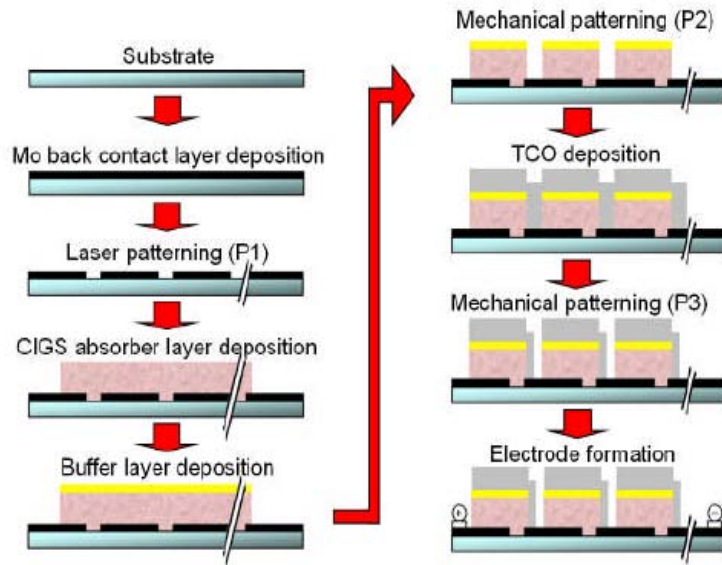


Figure 28. Typical process flow for preparing a flexible CIGS submodule cell. (From [87])

1. Performance of CIGS Solar Cells

CIGS-based cells are comprised of extremely thin layers of semiconductor material that are applied to low-cost backing materials, such as glass, stainless steel sheet, polyimide or metal foils. CIGS cells can also be prepared on flexible substrates, which are lighter than CIGS cells

prepared on rigid materials, and can be applied on uneven surfaces. Because of its flexibility, these cells can be rolled up when not in use.

CIGS cells exhibit the highest efficiency among flexible thin-film solar cells. A representative cell absorbs 99% of the available solar radiation in the first micron of the semiconductor material. In early 2008, US National Renewable Energy Lab developed a thin film CIGS solar cell with an efficiency of 19.9%, which set a new record for TFPV cells and approaches the 20.3% efficiency of silicon-based rigid cells [88]. Other than being lightweight, other key advantages include the ability to self-repair and operational stability over time. These advantages imply that CIGS cell performance may continue unabated over many years.

2. Degradation and Encapsulation of CIGS Solar Cells

Solar cells are used outdoors where they are continuously subject to harsh operating conditions, such as wind, sunlight, dust, snow, and water. Non encapsulated CIGS solar cells are known to be susceptible to degradation in performance when exposed to extreme temperatures, oxygen and moisture. Studies and experimental results show that these solar cells suffer from corrosion and exhibit smooth degradation at increasing temperature and humidity. There is a sharp increase in degradation rate at high humidity, even at low temperature conditions, down to 22C [89].

Encapsulation is a method to retard degradation and prolong the useful lifespan of solar cells. Both direct deposition and lamination approaches are used for

encapsulation. For direct deposition, a multi-layer coating is applied directly to the cell surface. Note that approaches used in encapsulation must be compatible with the flexible substrate [90].

Alternatively, lamination is a cheaper alternative and is a preferred choice as it serves as a protective layer over the flexible CIGS cells.

E. DC-TO-DC POWER CONVERTERS

A DC-to-DC converter is a class of power converter that converts a direct current source from one voltage level to another. When compared to a linear voltage regulator, an electronic switched DC-to-DC converter is more efficient than the former. The benefit of a DC-to-DC converter in a solar cell system is that it converts the varying input DC voltage (due to varying sunlight irradiance level at different times of the day) to match output battery voltage. Note that for solar applications, a DC-to-DC converter must work together with a maximum power point tracking device in order improve utility and effectiveness. Three basic types of DC-to-DC converters are considered in this chapter.

1. Buck Converter

A buck chopper is a step-down DC-to-DC converter. A diagram of a typical buck chopper is shown in Figure 29. The circuit consists of an inductor, a capacitor and two switches (usually a transistor and a diode). The operation of a buck converter is relatively simple. An input source voltage is connected to a load via an inductor when switch S closes. From a static operation point of view, the inductor acts as a virtual short circuit path, and the input voltage

is connected to the load. When switch S opens, the output voltage becomes zero. The capacitor must be large enough to maintain a consistent DC output voltage across the load. The buck chopper can operate either in the continuous conduction mode or discontinuous conduction mode. The operation of the buck chopper is governed by the duty cycle (D) and output voltage (V_o), which are determined by

$$D = \frac{t_{on}}{t_{on} + t_{off}}, \quad (5-3)$$

$$V_o = DV_i, \quad (5-4)$$

respectively, where V_i , t_{on} and t_{off} represent the input DC voltage periods when Switch S is closed and opened, respectively. From (5-3) and (5-4), it is clear that the maximum value for D is 1 and the maximum output DC voltage is equal to the input DC voltage.

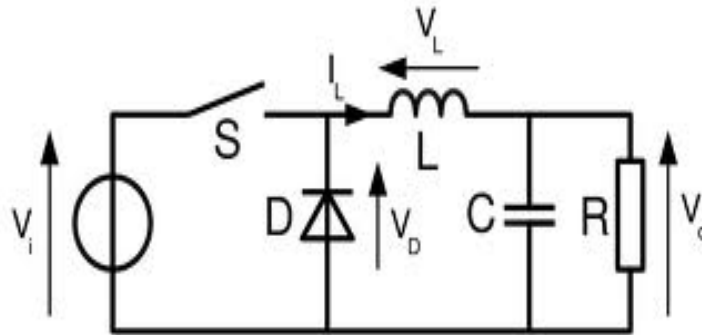


Figure 29. Buck chopper. (From [91])

2. Boost Chopper

A boost chopper is a step-up DC-to-DC converter and a diagram of a typical boost chopper is shown in Figure 30.

Similar to the buck chopper, the boost circuit consists of an inductor, a capacitor and two switches. However, the operation is slightly different. The load is always either connected to the source voltage or the capacitor voltage when the switch S is opened or closed, respectively. Again, the capacitor must be large enough to maintain a constant DC output voltage across the load. The boost chopper can also operate either in the continuous conduction mode or discontinuous conduction mode. The output voltage of the boost converter is determined by

$$V_o = \frac{V_i}{1-D}, \quad (5-5)$$

where the duty cycle D is given by (5-3).

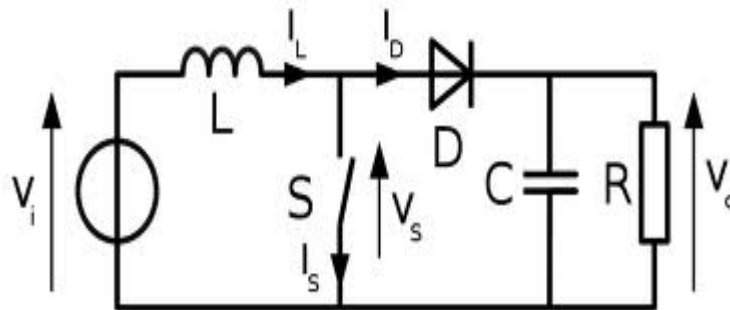


Figure 30. Boost chopper. (From [92])

3. Buck-Boost Chopper (Polarity Reversal)

A buck-boost converter is a step-up and step-down DC-to-DC converter, and a diagram of a typical buck-boost converter is shown in Figure 31. Similar to the previous two converters, the circuit consists of an inductor, a capacitor and two switches. The difference is the diode is now connected in the reverse direction. When switch S closes, the inductor is charged up by the input source, and the load

is connected only across the capacitor voltage. This is buck chopper operation mode. When switch S opens, the energy in the inductor is dissipated into the load and capacitor. This typifies boost operation. In either case, the polarity of the output voltage is reversed for this buck-boost converter configuration.

The buck-boost converter can also operate either in the continuous conduction mode or discontinuous conduction mode. While the duty cycle D is given by (5-3), the output voltage of the buck-boost converter is determined by

$$V_o = D\left(\frac{D}{1-D}\right)V_i \quad (5-6)$$

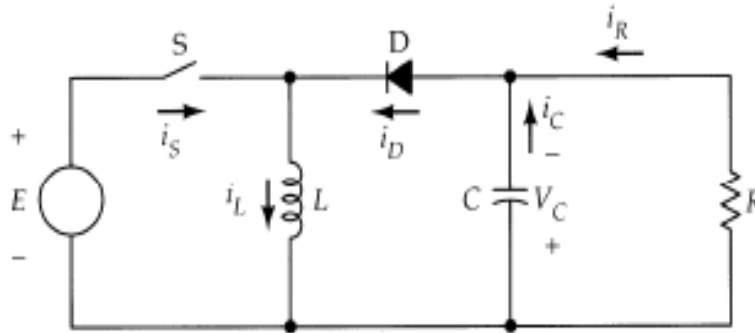


Figure 31. Buck-boost chopper (polarity reversal). (From [93])

F. MAXIMUM POWER POINT TRACKER

A DC-to-DC converter alone does not enable a solar panel to operate at its optimum point. A maximum power point tracker (MPPT) should be used in such a solar-electric circuit. The MPPT is a high efficiency electronic DC-to-DC converter that is capable of varying the electrical operating point of a solar panel so that it can deliver the maximum available power regardless of the prevailing battery

voltage. Without a MPPT, the power from a solar panel can possibly fall by 10 to 20 percent if a small surface area of the cell is in shadow. An MPPT may be designed based on either buck or boost topology. It is noted that a boost converter has higher energy efficiency than a buck converter [94].

With regard to MPPT algorithms, most are based on hill-climbing methods, and the maximum power point is found by changing the reference voltage of the solar panel. This ensures that the extracted power is always near or at its maximum based on the incident irradiation and operating temperature.

The MPPT adopts two common and simple tracking approaches for its operation; i.e., voltage-based and current-based maximum power tracking techniques. These two techniques are used because a solar panel's open-circuit voltage and short-circuit current are constant factors corresponding to the maximum power point [95].

Although the current-based tracking technique is preferred, the voltage-based tracking technique is simpler and more cost effective to implement. However, one of the main disadvantages of the voltage-based tracking technique is that the solar panel is disconnected from the load during sampling of its open circuit voltage, which results in unavoidable power loss and translates into lower efficiency [96].

G. BATTERY BALANCER CHARGER

Battery balancing is a technique that maximizes a battery's capacity so that it is only limited by the capacity of its weakest cell. A battery balance charger utilizes a uniform charging rate from a constant DC input power source, such as using a solar panel, to charge a battery. This ensures that all cells within the rechargeable battery pack are charged uniformly. By monitoring the individual cell voltages, none of the cells is either over-charged or under-charged. The advantage of using a balancer charger is the improvement in battery efficiency and increased capacity of the overall battery pack.

As the number of battery cells and load current increases, the potential for mismatch also increases. If a balancer charger is not used, two kinds of mismatches result in a battery pack: state-of-charge (SOC) and capacity/energy (C/E). Although SOC mismatch is more common, each problem limits the pack capacity to the capacity of the weakest cell. However, it is worth noting that the entire battery module will be balanced when all the cells exhibit the same state of charge [97].

H. CHAPTER SUMMARY

The chemistry and physics aspects of solar cells, such as the formation of p-n junctions, band gap energy, the photovoltaic effect, and factors affecting cell efficiency were discussed in this chapter. The performance of flexible CIGS solar cells, factors leading to CIGS cells degradation, as well as encapsulation method to slow down the degradation process were also considered.

The advantages of the CIGS solar cells are its light weight, flexibility, and its ability to maintain performance for substantial periods of time. These advantages meet the weight requirements, while generating extra solar power, for mini-UAV applications. Additionally, a maximum power point tracker is highly recommended in maximizing the output power extracted from a CIGS solar cell system to a load.

In the next chapter, the test plan for the solar array and the overall integrated system is presented.

VI. SOLAR PANEL TESTING, DESIGN AND ASSEMBLY

In this chapter, the test plan for the solar array is discussed. Further, its preparation, lamination and inter-cells connections work, as well as the overall system integration, are presented.

Prior to entering the design and assembly phase, it is important to verify the performance of the CIGS solar cells. This is accomplished by determining the average efficiency and the fill factor based on local Monterey, California climate conditions. Once the local data is determined, it is possible to obtain a good estimate of the solar array's output power prior to mounting onto the mini-UAV's wings.

A. TEST PLAN FOR EXPERIMENTAL SOLAR ARRAY CONFIGURATION

For the preliminary test, the solar cells' efficiency and fill factor are determined under sunlight conditions in the Monterey area. Two experimental solar arrays of 9-cells each are electrically connected in series and tested in two different manners: with a clear adhesive tape and without a transparent laminate. The first and second solar panels used for testing are shown in Figures 32 and 33, where each solar panel yields an effective surface area of 630 cm^2 and 1890 cm^2 , respectively.



Figure 32. First solar panel (630 cm²).

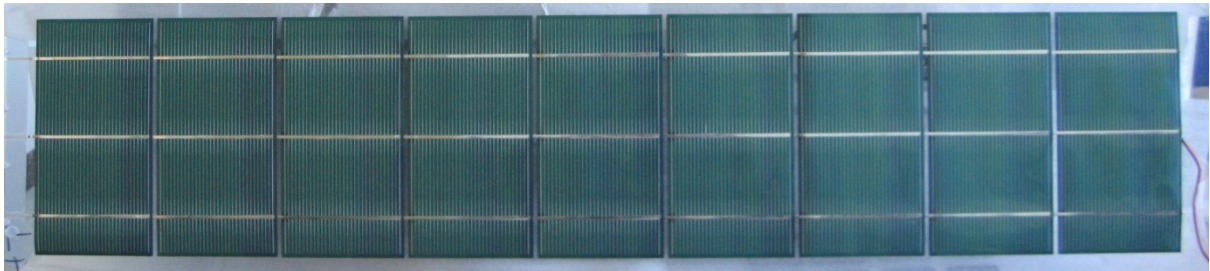


Figure 33. Second solar panel (1890 cm²).

The electrical circuit used for preliminary testing is shown in Figure 34. By disconnecting and shorting the variable resistor, the open circuit voltage and the short circuit current are determined, respectively. The entire solar panel IV curve response is subsequently obtained by varying the load resistor from its maximum to minimum value.

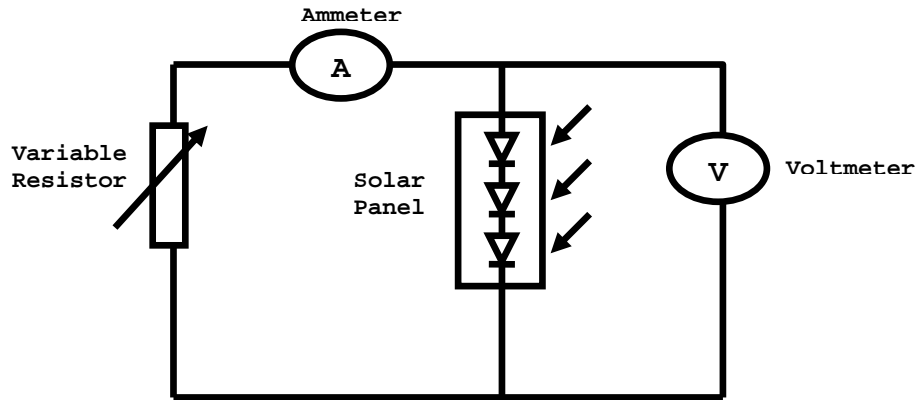


Figure 34. Solar array test setup circuitry.

In addition, the test results for each trial are verified by using a solar analyzer. This analyzer, the Amprobe Solar-600 Analyzer, is a professional analyzer for testing, troubleshooting and determining the efficiency of solar panels and is shown in Figure 35. It is capable of testing up to 60 VDC, rated at 12 A, with an accuracy resolution of $\pm 1\%$ [98].

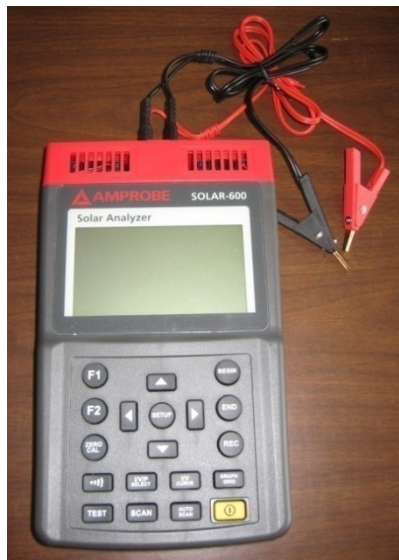


Figure 35. Amprobe Solar-600, Solar Analyzer.

Alongside the Amprobe Solar-600, a separate solar power meter, the Amprobe Solar-100, is used to measure sunlight irradiance to accurately determine the solar cell's efficiency. The Amprobe Solar-100 solar power meter is shown in Figure 36. It has a measuring range up to 2000 W/m^2 , a resolution within 0.1 W/m^2 , and accuracy typically within $\pm 10 \text{ W/m}^2$ [99].



Figure 36. Amprobe Solar-100, Solar Power Meter.

1. Preliminary Testing without Laminated Solar Panel

Based on the test circuit depicted in Figure 34, both solar panels are tested without lamination. In order to obtain more consistent test data, each solar panel is tested three times and average values were computed. Under this test trial, for the first solar panel, the average efficiency and fill factor is found to be approximately 9.68% and 55.57% (assuming sunlight irradiance at AM 1.5 conditions), respectively. Likewise, the average efficiency and fill factor for the second solar panel are approximately 5.50% and 43.04%, respectively. The IV curves for the first and second solar panel are shown in Figures 37 and 38, respectively.

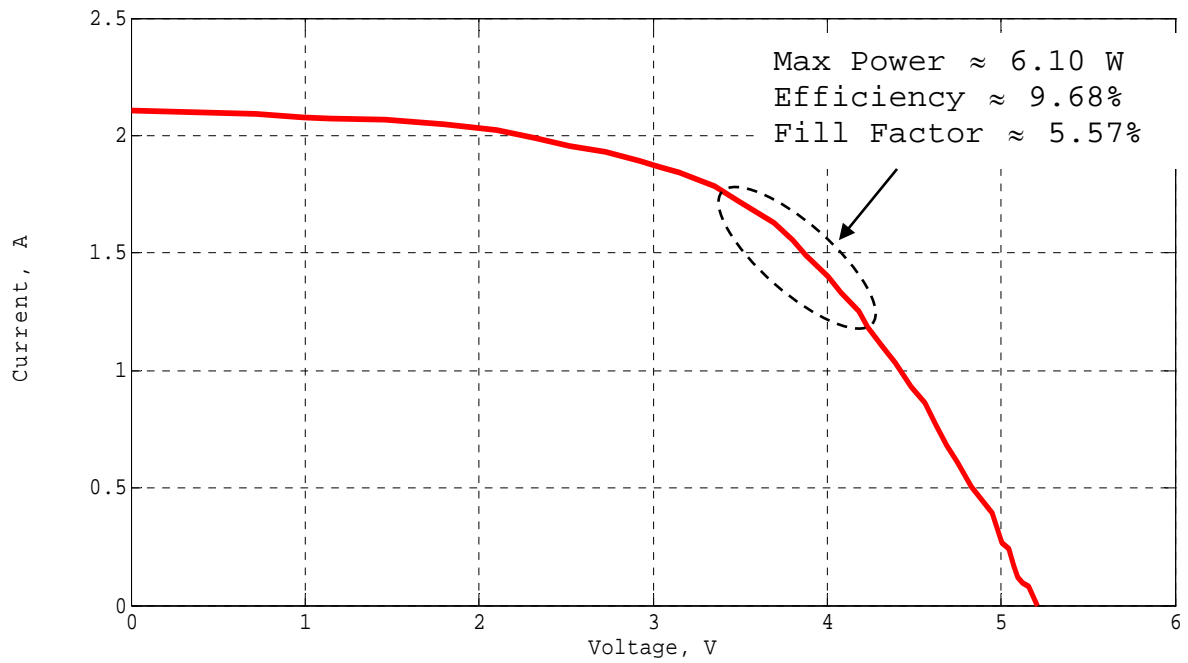


Figure 37. IV curve for first solar panel without lamination.

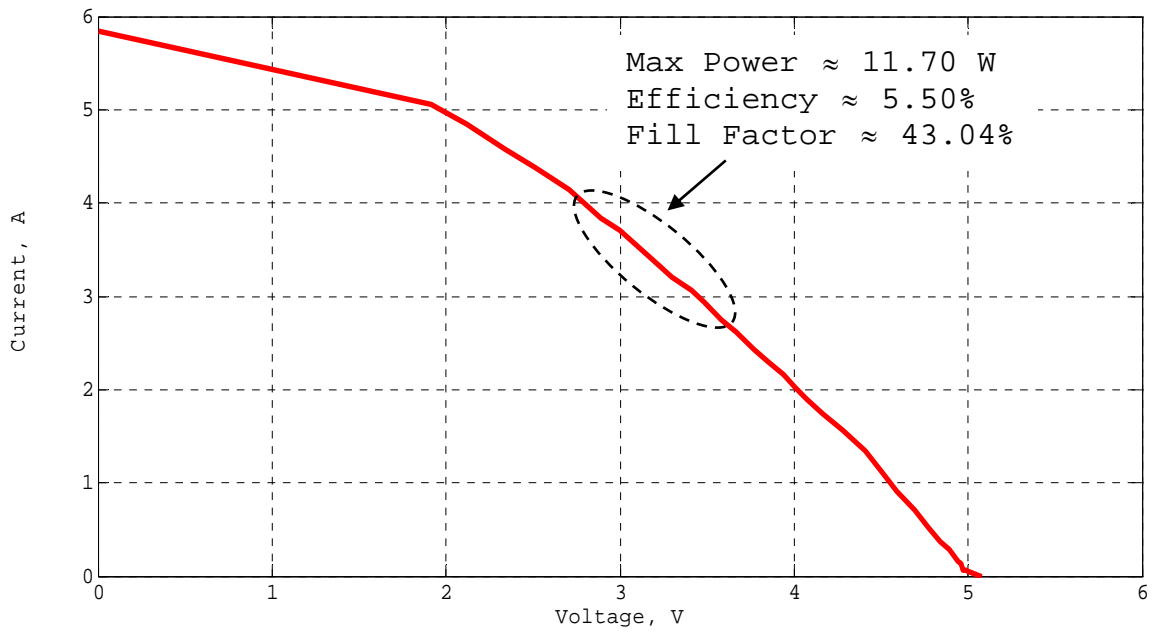


Figure 38. IV curve for second solar panel without lamination.

2. Preliminary Testing with Laminated Solar Panel

In this test trial, both solar panels are tested with lamination using clear adhesive tape. From the testing, the average efficiency and fill factor for the first solar panel are approximately 9.85% and 55.22%, respectively. The average efficiency and fill factor for the second solar panel are approximately 6.94% and 44.91%, respectively. The IV curves for the first and second solar panel are shown in Figures 39 and 40, respectively.

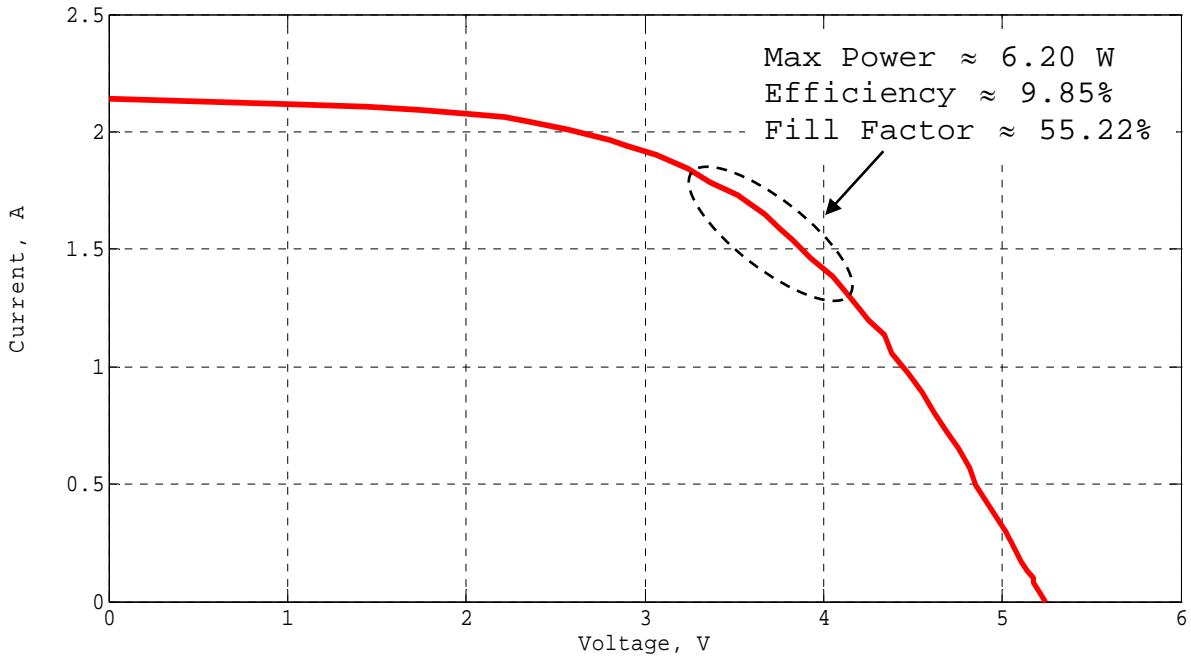


Figure 39. IV curve for first solar panel with lamination.

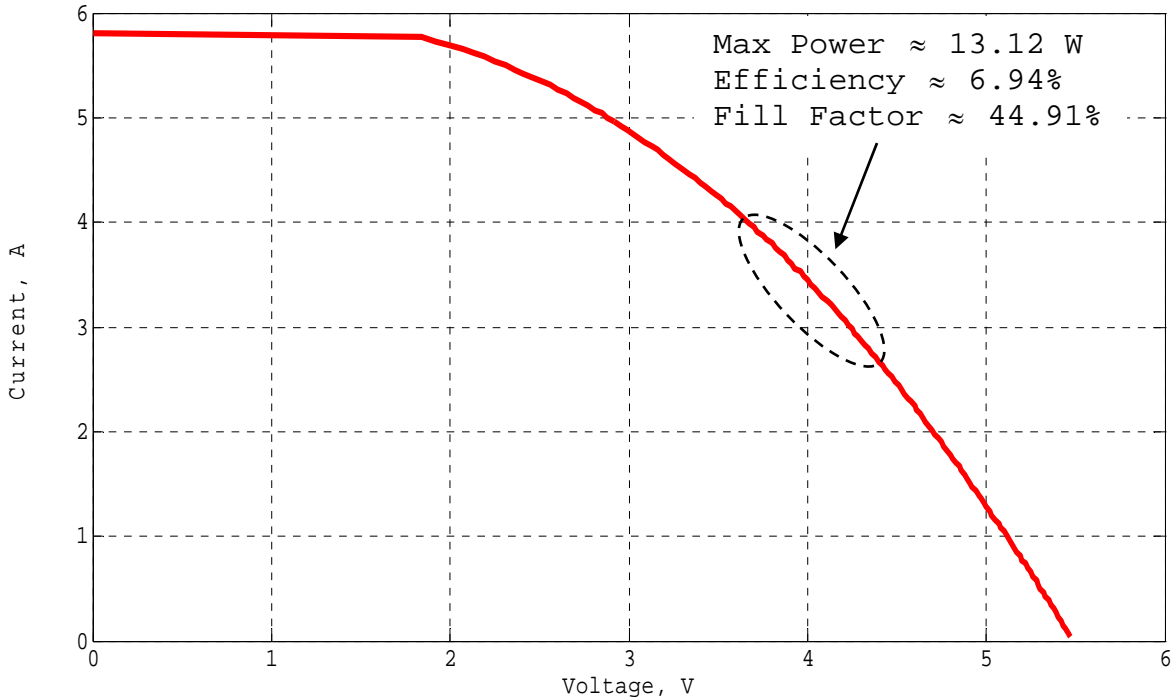


Figure 40. IV curve for second solar panel with lamination.

The accuracy of these test results is verified using the solar analyzer to independently determine the efficiency and fill factor of each of the panels. The measurements taken by Amprobe Solar-600 echoed the results computed in the earlier tests.

3. Test Conclusion

All test results are summarized in Table 13. The output power of the solar panels is then estimated based on average cell efficiency and fill factor, which ranged between 5.50% to 9.85% and 43.04% to 55.57%, respectively, under sunlight conditions in Monterey.

Table 13. Solar panels test measurement under sunlight conditions.

S/N	Description	Ave. Max. Output Power (W)	Ave. Efficiency (%) (Assume Input Power = 1000 W/m ²)	Ave. Fill Factor (%)
1	First Solar Panel (630 cm ²) without lamination	6.10 W	9.68%	55.57%
2	Second Solar Panel (1890 cm ²) without lamination	11.7 W	5.50%	43.04%
3	First Solar Panel (630 cm ²) with lamination	6.20 W	9.85%	55.22%
4	Second Solar Panel (1890 cm ²) with lamination	13.12 W	6.94%	44.91%
5	First Solar Panel (630 cm ²) with lamination using Amprobe Solar-600 for measurement	6.20 W	9.80%	53.50%
6	Second Solar Panel (1890 cm ²) with lamination using Amprobe Solar-600 for measurement	14.73 W	7.80%	47.28%

From the test results, we see that the experimental laminated solar panels exhibit a slight improvement in the average efficiency and fill factor. Note that an additional benefit of lamination is the slowdown of the cell degradation process due to environmental conditions.

It is also observed that the average efficiency and fill factor differ for both test trials despite the fact that the cells belong to the same manufacturing batch. Based on this observation, it is important to ensure that the solar cells used for the final solar array exhibit consistent voltage and current readings to prevent power

“choking” at the output. Note, for consistency purposes, AM 1.5 light conditions are used as a reference for all test measurements.

B. FINAL SOLAR ARRAY ARRANGEMENT

The original thin-film CIGS TFPV cells manufactured by Global Solar Energy are constructed in a single string of 18 cells connected in series. Each individual cell measures 21x10 cm as shown in Figure 41.

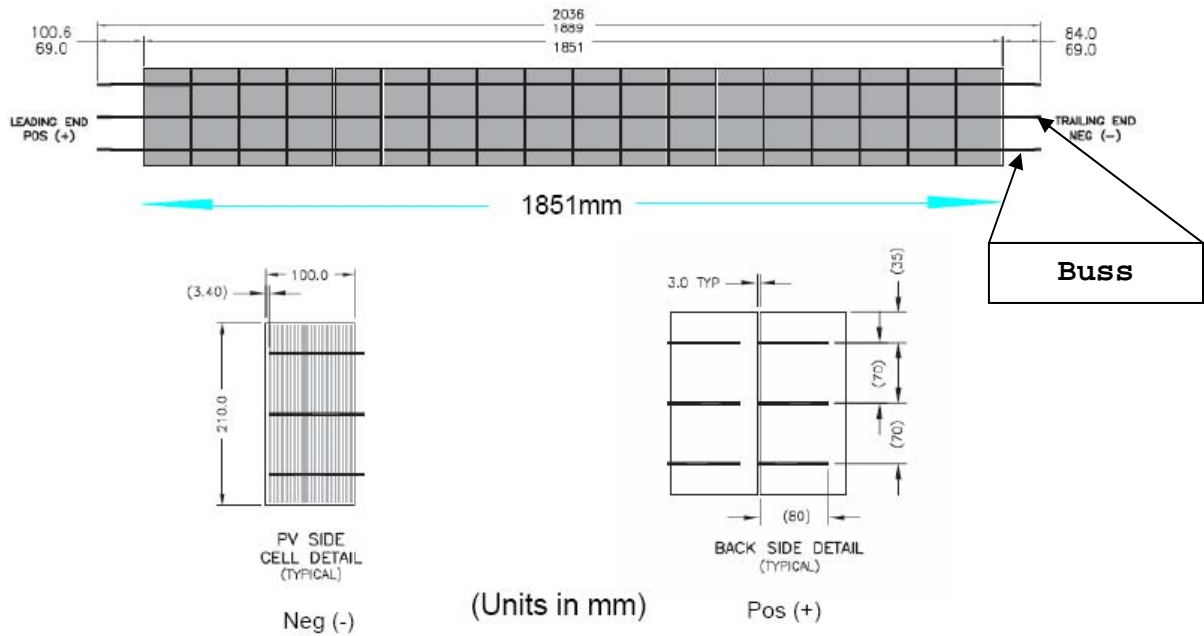


Figure 41. CIGS TFPV cells. (After [100])

Each cell gives an average 0.54 V output DC voltage regardless of the surface area. However, the maximum output current is directly restricted to the surface area of the smallest cell in a series connection. In other words, it is possible to achieve a higher DC voltage when smaller cells are connected in series, but the current is limited to the cell with the smallest surface area. Conversely, it is also possible to obtain a higher output current but a lower

voltage when larger cells are connected in series. In either case, the main objective is to achieve a high, optimized output power. In view of the design possibilities, a higher output voltage in series connection is preferred in order to minimize potential power losses in the entire circuit.

To maximize the available surface area on the wings, the final solar array consists of 48 solar cells connected in series. Each cell measures 10 cm in length and 7 cm in width, thereby yielding a total surface area of 3360 cm². The layout of the final solar array is shown in Figure 42. The Raven mini-UAV wings will also be modified and re-designed to offer better lift capability.

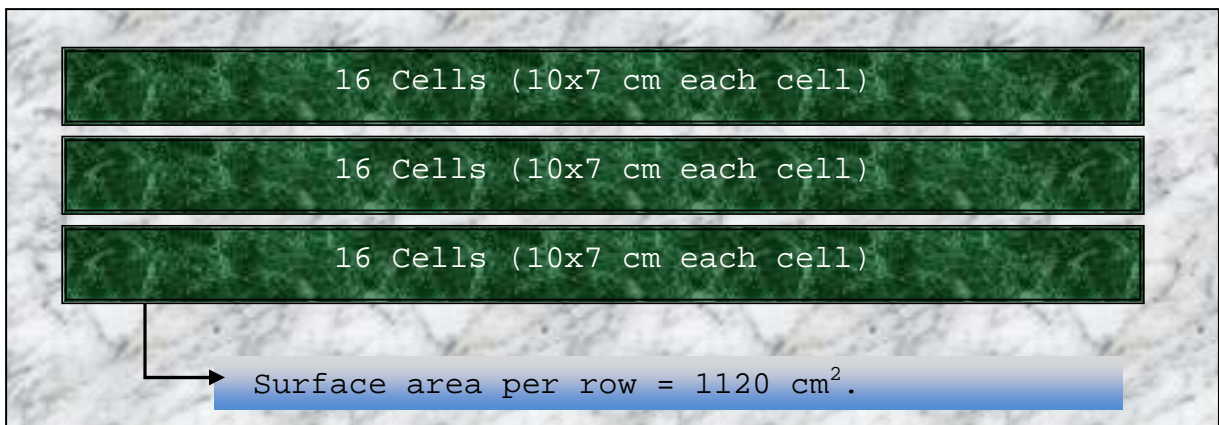


Figure 42. Solar array arrangement.

Under AM 1.5 (100 mW/cm²) sunlight irradiance conditions, it is theoretically possible for the solar array to obtain an input power of 336 W from the Sun. Taking the upper and lower range of cell efficiencies between 5.50%-9.85% (Table 13), and with a typical efficiency estimated at 98% for a DC-to-DC power converter (with MPPT algorithm), the expected upper and lower net output power from the final solar array are 32.44 W and 18.11 W, respectively, which are

given by input power = $(0.1 \text{ W/cm}^2)(3360 \text{ cm}^2) = 336 \text{ W}$, upper range output power = $(336 \text{ W})(0.0985)(0.98) = 32.44 \text{ W}$, and lower range output power = $(336 \text{ W})(0.055)(0.98) = 18.11 \text{ W}$. Note that both 32.44 W and 18.11 W characterize only the typical range of the output power and do not represent the absolute range. In other words, there may still be a possibility that the output power of the final solar array is higher than 32.44 W. Hence, for testing accuracy purposes, the output power of the final solar array will be measured and additional testing will be discussed in the next chapter.

C. PREPARATION WORK FOR FINAL SOLAR ARRAY

It is necessary to exercise extra caution when slicing the solar cells to their specific dimensions due to their flexible nature.

First, clean gloves must be worn during the slicing process to prevent moisture, oil and acid from bare hands to be in direct contact with the cells. In addition, gentle handling is required so that the cells are not distorted, twisted, scratched or stressed, reducing the number of physical defects.

A regular razor blade used with adequate hand pressure can slice the solar cells neatly. Because the tip of the razor blade is the only contact with the surface of the cell during slicing, this reduces the risk of short-circuiting or damaging the entire cell. The slicing technique is shown in Figure 43. As part of the preparation work, each sliced solar cell is tested to ensure its functionality by determining its IV curve.



Figure 43. Slicing CIGS TFPV cells.

D. LAMINATION OF FINAL SOLAR ARRAY

With the IV curves verified, the top surface of the solar array will be laminated with a clear tape to protect against environmental moisture, ill effects of solar radiation, handling stresses or even cell punctures. The lamination also adds strength and toughness to the solar array so that the cells do not rip or dent easily. Being transparent and self-adhesive in nature, the lamination material allows light photons to effectively penetrate through, which promotes electron-hole pair generation, producing electric power between the anode and cathode. Both the lamination tape and the lamination process are shown in Figures 44 and 45, respectively.



Figure 44. Clear adhesive tape. (From [101])



Figure 45. Solar array lamination.

The lamination process has a significant impact on performance. The solar array will be damaged if the clear tape is ripped off of it. For this reason, the lamination process requires careful workmanship.

E. ELECTRICAL CONNECTIONS

Based on data from Table 13, the solar array is expected to achieve an open circuit DC voltage of 25.92 V (total 48 cells; average 0.54 V per cell) with an output

power of $(3360 \text{ cm}^2/630 \text{ cm}^2) \times 6.2 \text{ W} = 33.10 \text{ W}$. The maximum potential current was then calculated to be $(33.10 \text{ W}/55.57\%)/25.92 \text{ V} = 2.30 \text{ A}$.

At 2.30 A, a wire gauge rating of 18 AWG and above is chosen to interconnect the solar cells. However, if a round conductor were to be used on the mini-UAV wings, it might affect the air flow and cause an increase in the overall aircraft weight, leading to a reduction in flight efficiency. To avoid this, two other options under consideration are either the 0.10 mm X 16 mm flat tinned copper buss material shown in Figure 41 or a self-adhesive flat copper tape shown in Figure 46. It is also necessary to solder the inter-cells connections so that they do not rip apart during flight.



Figure 46. Self-adhesive flat copper tape. (From [102])

As depicted in Figure 47, the inter-cells are connected in series with the top and bottom terminals represented by red and black color conductors, respectively. The top represents the cathode (negative) terminal, while the bottom represents the anode (positive) terminal.

Next, a blocking diode (Motorola diode model P/N: HEP170) has to be connected at the anode terminal to prevent a backflow of current from the battery to the solar array. An additional layer of clear tape is used to firmly secure the solar array onto the mini-UAV wings.

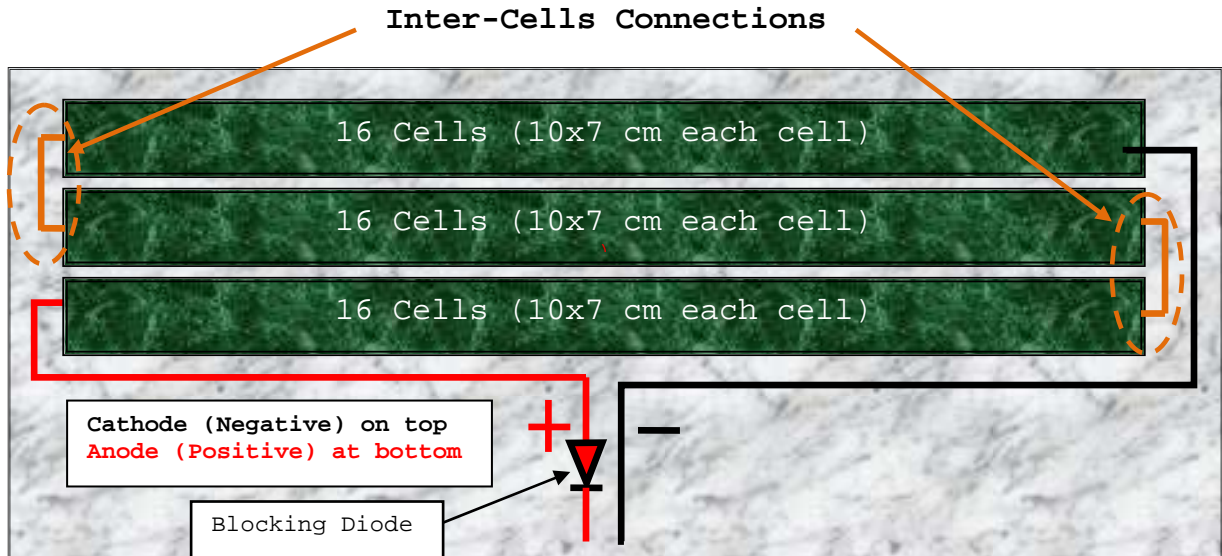


Figure 47. Solar array wiring.

F. SPV1020 DC-TO-DC BOOST CONVERTER WITH BUILT-IN MAXIMUM POWER POINT TRACKER ALGORITHM

A DC-to-DC power converter with MPPT algorithm will be added into the overall system circuitry to optimize the output power from the solar array and to minimize losses. Without this, varying factors such as sunlight irradiance, operating temperature, angle of sunlight incidence are likely to impede the solar array from producing a consistent output power.

The SPV1020 is a fully integrated, highly efficient, (up to 98%) DC-to-DC power (boost) converter integrated chip (IC) with a four-phase interleaved topology from ST

Microelectronics. It has an input voltage range from 6.5 V to 45 V, with a built-in MPPT algorithm. The power conversion is optimized and managed by a digital unit running the MPPT algorithm based on monitoring of voltage and current supplied by the solar array. The MPPT algorithm is assisted by a 10-bit precision analog-to-digital Converter (ADC) for current and voltage sensing. The electrical characteristics of the SPV1020 DC-to-DC power converter are shown in Table 14.

Table 14. SPV1020 electrical characteristics. (From [103])

Symbol	Parameter	Test Condition	Min	Typ	Max	Unit
Input Source Section						
VIN	Operating input voltage		6.5		45 V	
Iq	Quiescent current	ILOAD=0 mA, VOUT=36 V, SHUT=0 V, Tj=Tamb, PWM=5%		5		mA
ISD	Shut down mode current consumption	ILOAD=0mA, VOUT=36V, SHUT=5V, Tj=Tamb		1		mA
VUVLO	Under voltage lock-out threshold for turn ON	VIN increasing		6.5		V
	Under voltage lock-out hysteresis			-0.5		V
Power Section						
RDSON-LS	Power switch ON resistance			70		mΩ
RDSON-H	Synchronous rectifier ON resistance			70		mΩ
Control Section						
VOUT	Operating		Vin		45 V	V

	output voltage					
IOUT	Operating output current				8	A
Ilim	LX switch current limit		4	4.5	5	A
FPWM	PWM frequency (default value)		70	100	150	kHz
VREF	Constant voltage control loop internal reference voltage		1.18	1.23	1.27	V
Thermal Shutdown						
Tshutdown	Over temperature threshold for turn OFF	Temperature increasing	140	150	160	°C
	Over temperature hysteresis			-20		°C

1. Partitioning Input and Output Voltages

The existing SPV1020 DC-to-DC power converter evaluation pack, shown in Figure 48, is designed to work properly with a minimum input voltage of 30 to 36 V and capable of providing an output voltage of 40 V with a maximum power of 230 W.

Since the output voltage of the solar array is lower than the minimum input voltage of the SPV1020 DC-to-DC power converter evaluation pack (30 V), the input voltage must be partitioned and scaled by re-designing the input resistances (R1 and R2) on the SPV1020 electronic board for proper operation. Similarly, it is also necessary to re-design the output resistances (R3 and R4) in order to provide the desired output voltage. The equations used for partitioning

the input and output voltages can be found in the AN3272 Application Note. To optimize the efficiency of the whole system, the power dissipated by the input and output resistances must be taken into consideration [103].

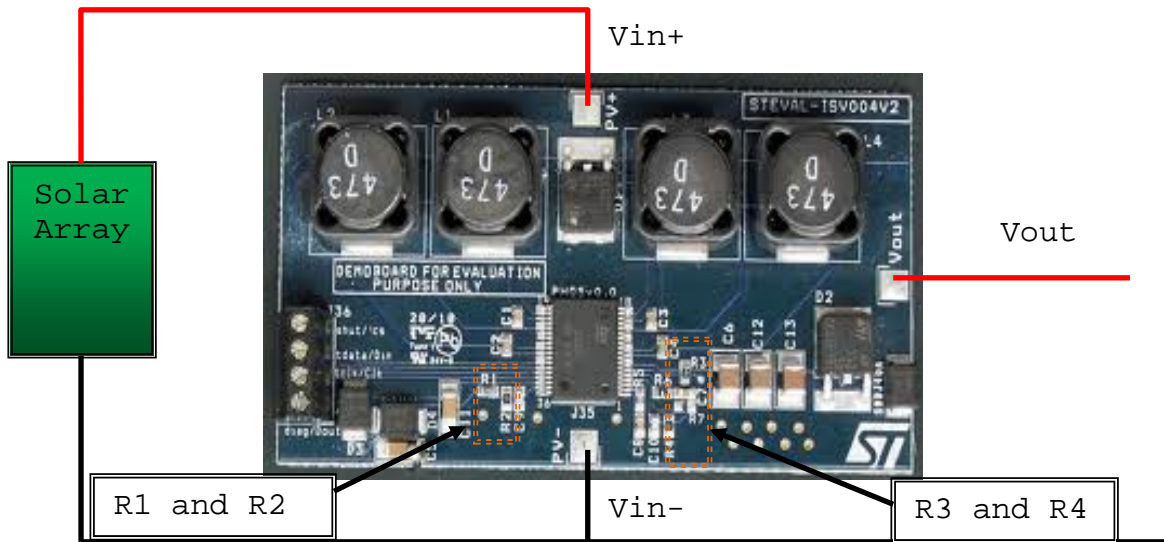


Figure 48. SPV1020 DC-to-DC boost converter evaluation pack. (After [104])

2. SPV1020 as a Battery Charger

The SPV1020 DC-to-DC power converter can double as a battery charger if it is properly connected with a constant current-constant voltage (CC-CV) controller, such as the ST SEA05 controller, which provides both voltage and current control. The functional block diagram of the ST SEA05 controller is shown in Figure 49.

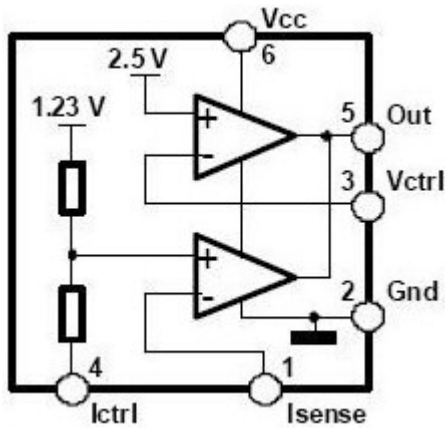


Figure 49. ST SEA05. (From [103])

As indicated in Figure 49, SEA05 provides two independent internal thresholds designed to separately control both the battery voltage and current control. These two thresholds are the reference voltages used for two comparators that have common outputs. If one of the two thresholds is triggered, then the common output is proportionally forced low. Thus, the output behavior of the SEA05 is perfectly compatible with the PZ_OUT pin of the SPV1020 [103].

Refer to SPV1020 and SEA05 datasheets for further instructions. The connection diagram using SPV1020 as a battery charger with output current control is shown in Figure 50.

Table 15. GV24-6 solar charge controller specifications.
(After [3])

Tracking Efficiency	99%
Electrical Efficiency (typical)	90-96%
Input Current (Maximum)	6 A
Panel Voltage (Voc)	0-63 V
Min. Panel Voltage for Charging	5V
Night Consumption	6 mA
Absorption Voltage	28.4 V
Float Voltage	27.6 V
Temperature Compensation	56 mV/°C
Compact and Light	5.5x2.5x1.2" (14x6.5x3.1 cm) /6.5 oz. (185 g)
Connections	4-pos. clamp-style terminal block for 10-30 AWG wire
Environmental	Stainless Hardware Nickel-Plated Brass Contacts
Additional Features	Multi-Stage Charging Temperature Compensation Can Charge from a DC Source Automatic Recovery from Fault Conditions LED Status Indicator Reverse Panel Protection Overload Protected (No blown fuses!) Over-Temperature Protected with Current Foldback Shade-Tolerant Tracking Suitable for Gel/AGM/Sealed Lead-Acid Batteries Surface-Mountable Box Reverse Battery Protection Custom Voltages Available for Lithium and Other Batteries

H. SYSTEM INTEGRATION

The schematic diagram for the final integrated system, comprised of the laminated solar array, SPV1020 DC-to-DC boost converter, battery and a load, is shown in Figure 52. The solar array is connected to the SPV1020 DC-to-DC power converter, and its output is used to charge the battery. The load, which represents the mini-UAV, draws energy from the battery during flight missions.

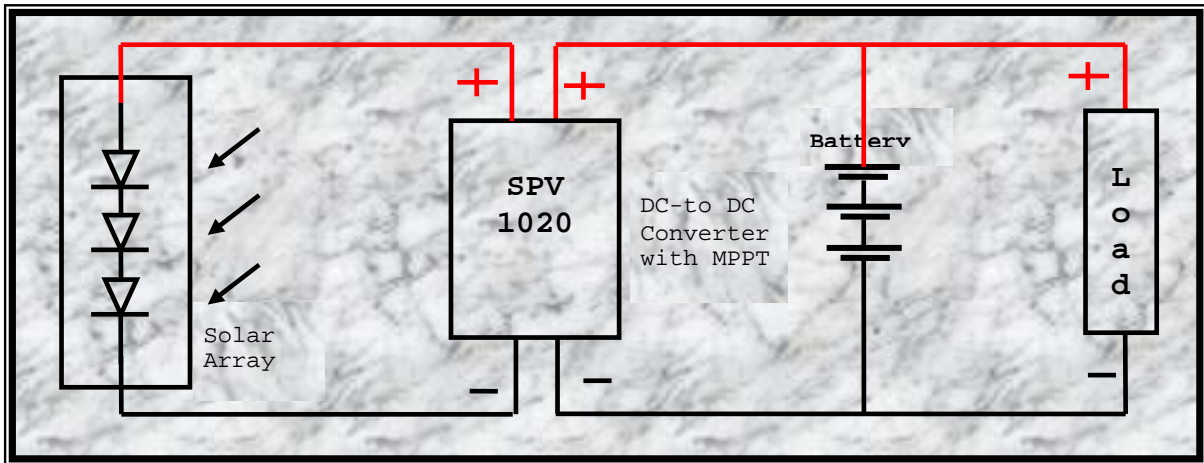


Figure 52. Schematic diagram for final system integration.

I. CHAPTER SUMMARY

The preliminary tests, under sunlight conditions, for two different solar panel configurations (with and without lamination) to determine the average cell efficiency and fill factor were discussed in this chapter. The results of the preliminary tests are important as they provide a good indication of the expected output power for the final solar array.

The preparation work for the final solar array configuration was also discussed. It is comprised of three rows of 16 cells each connected in series, yielding a total surface area of 3360 cm². The top surface of the solar array is laminated to obtain improvement in the average efficiency and fill factor and also to prevent cell degradation due to environmental conditions. The next chapter details additional testing and software simulation for the final solar array.

VII. TEST AND ANALYSIS

The testing and simulation of the final solar array will be discussed in this chapter. First, IV curves are plotted for the solar array (configured with and without lamination) to estimate the range of power that can be extracted from the final solar array and to confirm that the laminated configuration offers a higher output power.

Next, due to weather limitations, progress was impeded in carrying out actual testing under sunlight conditions. To overcome these limitations, simulation model are developed (using Matlab and Simulink program) to complement the actual testing. Suitable test models were developed to anticipate total flight endurance for both a battery alone and a battery with solar cells configuration running at different throttle speed settings (55%, 65%, 70% and 100%). These throttle speed settings are chosen by the Raven mini-UAV's operator from the Naval Air Warfare Center Weapons Division, in China Lake, California [3]. The simulation models are validated by comparing the simulated results with the findings obtained in previous thesis work [3].

Last, one of the validated simulation models is enhanced for simulation testing of the final solar array. The enhanced simulation model allows variation of the SPV1020 DC-to-DC power converter's efficiency, output power from the solar array, as well as the battery energy capacity.

A. SOLAR ARRAY TESTING

The IV curves for the final solar array, acquired using the Solar 600 Analyzer under sunlight testing, are shown in Figures 53 and 54, respectively.

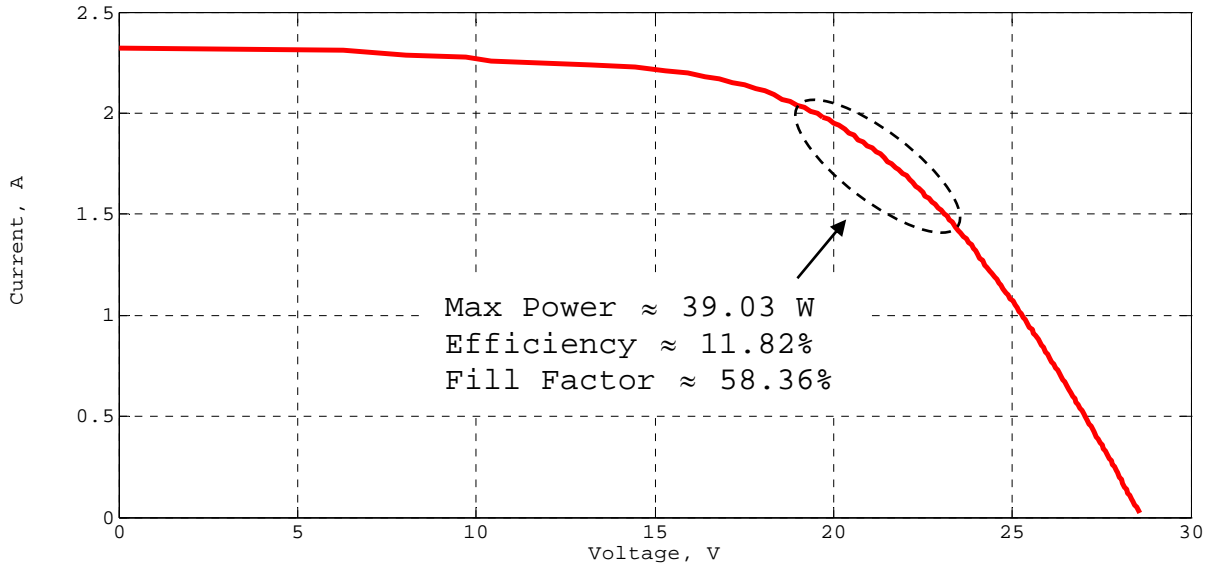


Figure 53. IV curve for final solar array without lamination.

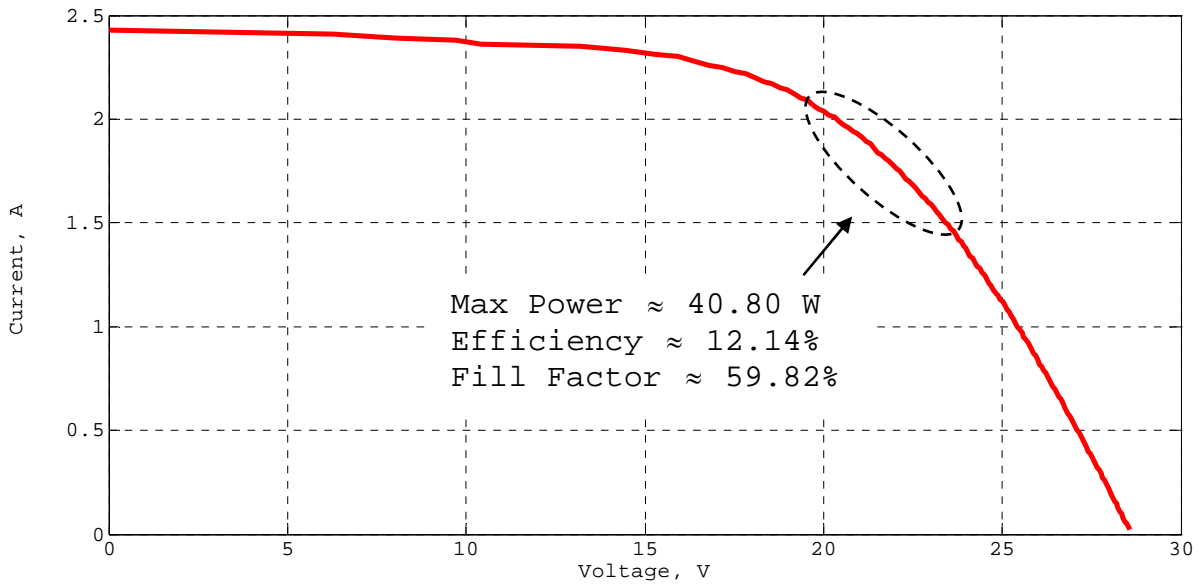


Figure 54. IV curve for final solar array with lamination.

Table 16. IV curves data for final solar array.

Type	Output Power (W)	Efficiency (%) (Assume Input Power = 1000 W/m ²)	Fill Factor (%)
Solar array without lamination	39.03 W	11.62%	58.36%
Solar array with lamination	40.80 W	12.14%	59.82%

From Table 16, it can be seen that the laminated solar array performed slightly better in terms of its output power, efficiency and fill factor. It is also important to note that the laminated solar array obtained a higher output power than the typical upper range of 32.44 W.

B. VALIDATION OF BASIC SIMULATION MODELS

The generic Simulink models, with and without the solar panel incorporated, are shown in Figures 55 and 56, respectively. The functionality for each section is explained next.

As indicated in Figures 55 and 56, the initial battery energy capacity and the energy consumed by the mini-UAV in the first ten minutes of operation at 100% throttle speed in order to reach its designated area-of-operation is shown in Section 1. The battery energy is easily modified to influence the total flight endurance. A negative ramp input is injected to simulate energy drained in the first ten minutes. The same amount of positive energy is compensated back to simulate a net zero energy consumption after ten minutes. The entire simulation is tied together using common clock timing as shown in Section 2, while the energy remaining after the first ten minutes is shown in Section 3.

The overall energy consumption for the entire simulation period is shown in Section 4, while a sub-model used to compare the existing energy level against the zero energy level is shown in Section 5. The comparison sub-model is useful for computation work. The constant net energy consumed per hour at a particular throttle speed setting is shown in Section 6. The net solar energy added back to the system after the initial ten minutes of flight is shown in Section 7 of Figure 55.

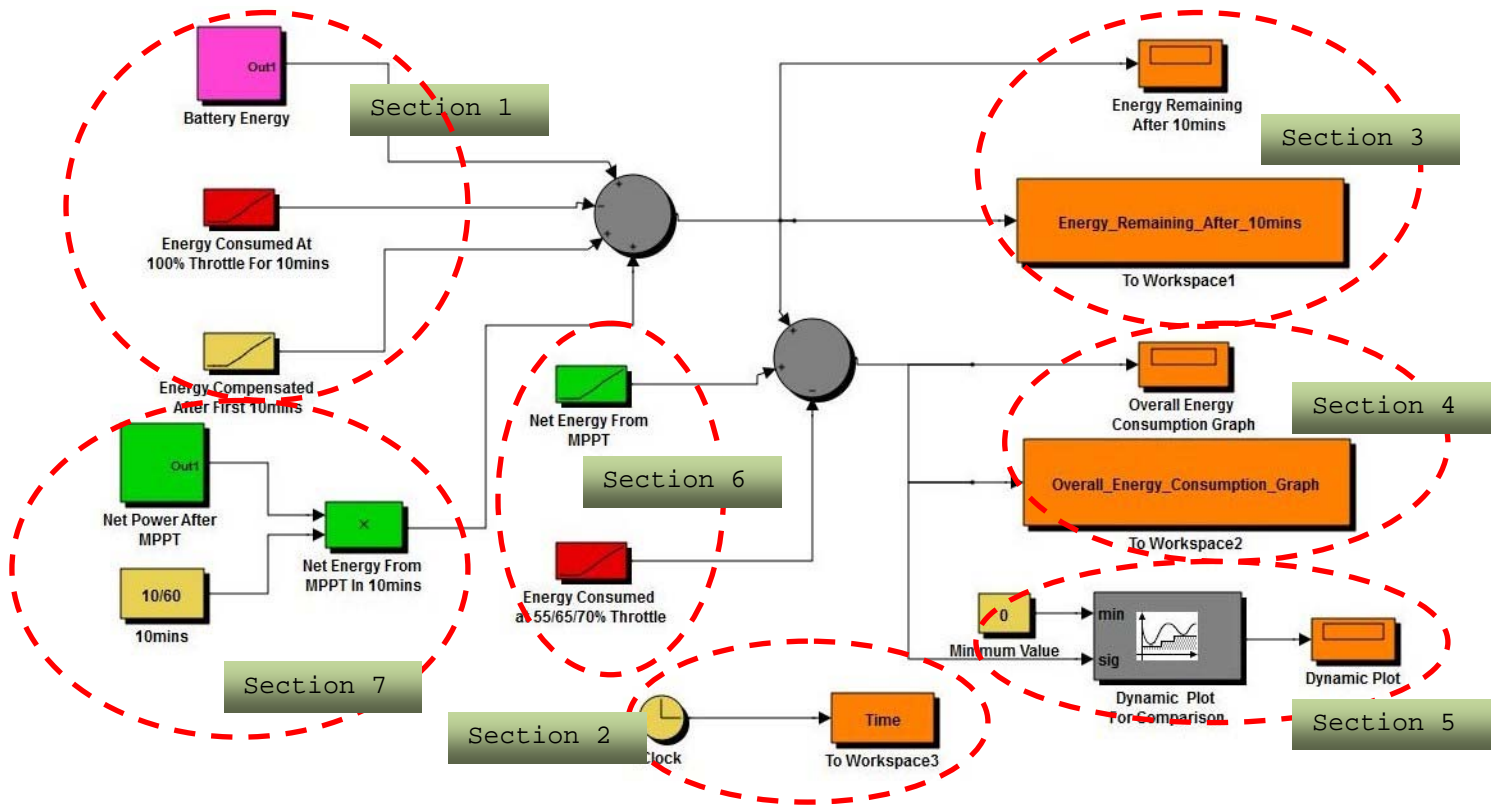


Figure 55. Simulation model with solar panel.

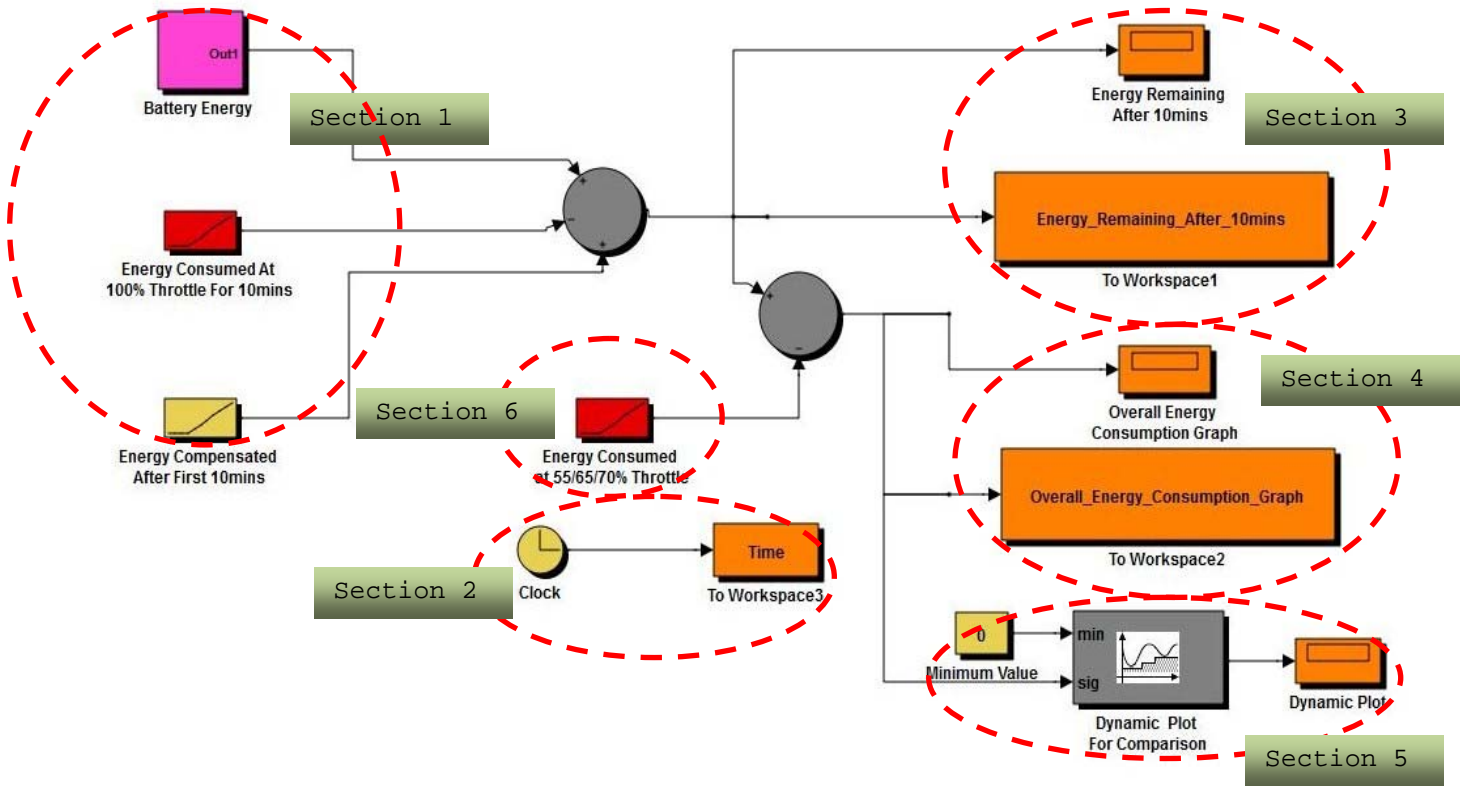


Figure 56. Simulation model without solar panel.

A 6-cell, 25 V, 4 AH (amperes-hours) lithium-ion battery pack is modeled for all simulations. This is equivalent to the battery voltage used in the Raven mini-UAV. The purpose of using a 25 V, 4 AH battery is to validate the accuracy of the simulation model's behavior by verifying the simulation results against the findings in previous thesis work [3]. The findings from [3] are shown in Table 17.

Table 17. Summary of actual Raven mini-UAV energy consumption and flight endurance test data. (After [3])

Throttle Speed (%)	55%	65%	70%	100%
Average current (A)	1.32	1.64	1.75	5.43
Average voltage (V)	22.70	22.96	22.40	21.72
Average resistance (Ω)	17.19	14.00	12.80	4.00
Energy consumption (WH)	30.23	37.56	40.08	129.78
Throttle Speed (%)	100%-55%	100%-65%	100%-70%	
Endurance lasted with battery alone (minutes)	113	94	86	
Endurance lasted with solar panel and MPPT (minutes) at 12 W output power	180	132	121	
Endurance lasted with solar panel and MPPT (minutes) at 17 W output power	243	163	146	

As mentioned in Chapter III, it is important not to overcharge the lithium battery in excess of 4.235 V or to discharge the voltage below 3.0 V per cell. If this occurs, the battery will no longer accept a full charge and may experience problems holding voltage under load. For this reason, the battery used will not discharge less than 85% of its nominal ratings (voltage and current). The rated battery capacity (C) and the rated battery energy capacity (E) can be computed from [105]

$$C = It \quad (7.1)$$

$$E = CV_{\text{avg}}, \quad (7.2)$$

respectively, where C is the battery capacity in amp-hours, I is the current in amperes, t is the time in hours, E is the battery energy capacity in watt-hours, and V_{avg} is the

average voltage during discharge. The battery energy capacity used for simulation is 100 WH, computed from Equation (7.2) by multiplying 25 V by 4 AH.

Since the simulation does not permit the battery to discharge below 85% of its rated energy capacity, the operating battery energy capacity is restricted to 72.08 WH, computed from the product of 84.9% of rated voltage and 84.9% of rated current. This is also the same battery energy capacity used in [3].

1. Simulation Results Using Battery without Solar Panel

Using the Simulink model depicted in Figure 56, simulations are conducted utilizing the battery without solar panel configuration at 55%, 65%, and 70% throttle speed settings. The resulting plots (Energy vs. Time) are shown in Figures 57 to 59, respectively. Note that all simulations involve operating at 100% throttle speed for the first ten minutes. The simulated results and the actual findings [3] are tabulated in Table 18 for ease of comparison.

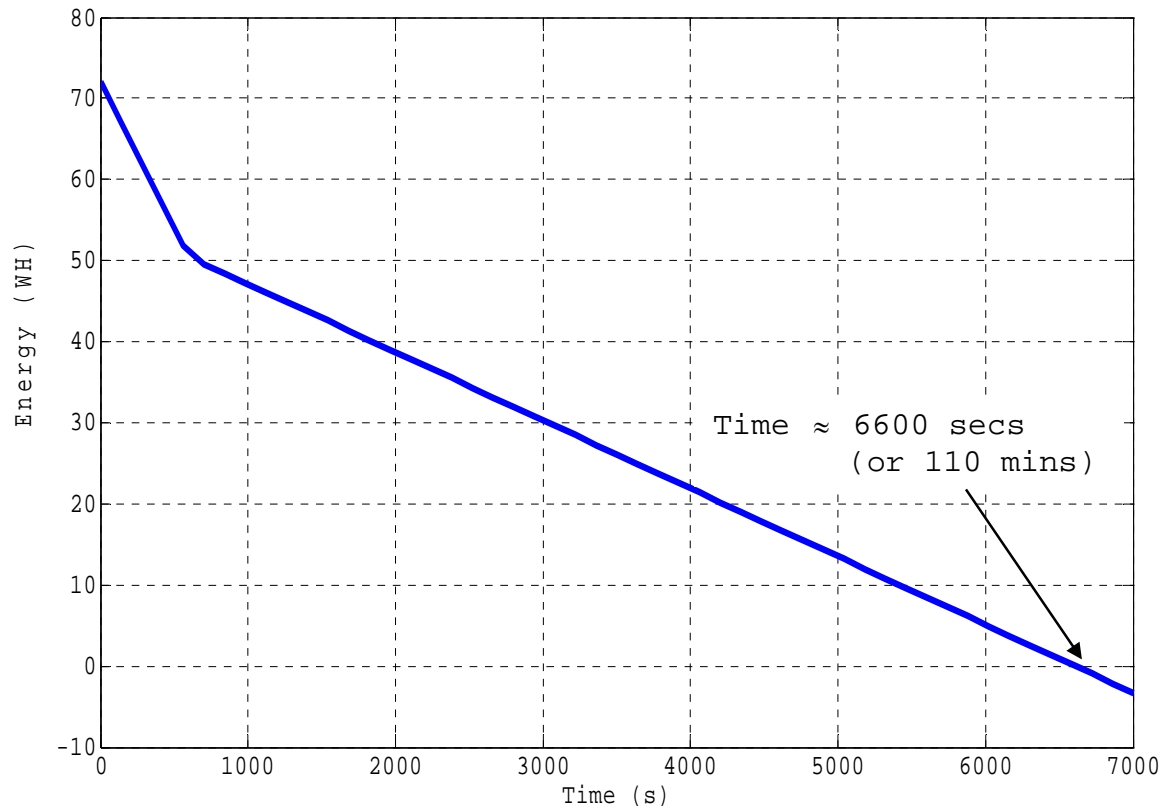


Figure 57. Simulation for battery energy consumption at throttle speed (100%-55%) without solar panel.

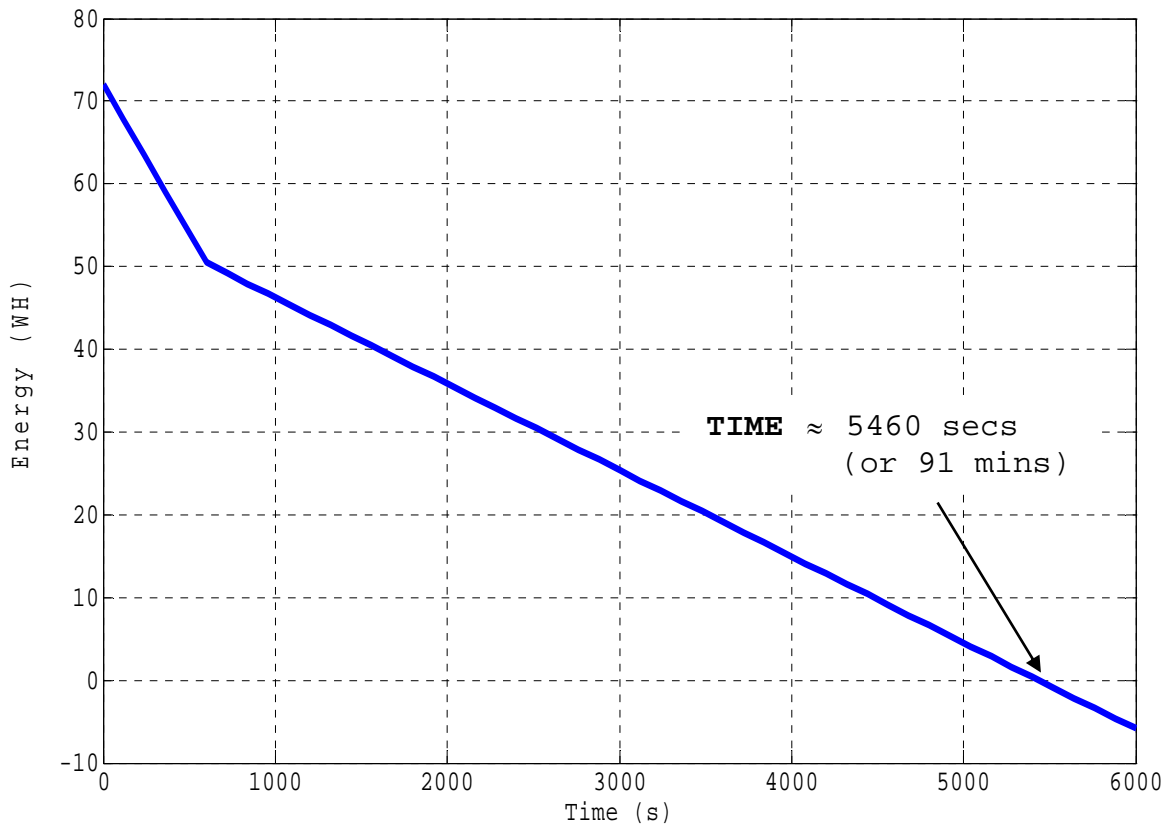


Figure 58. Simulation for battery energy consumption at throttle speed (100%-65%) without solar panel.

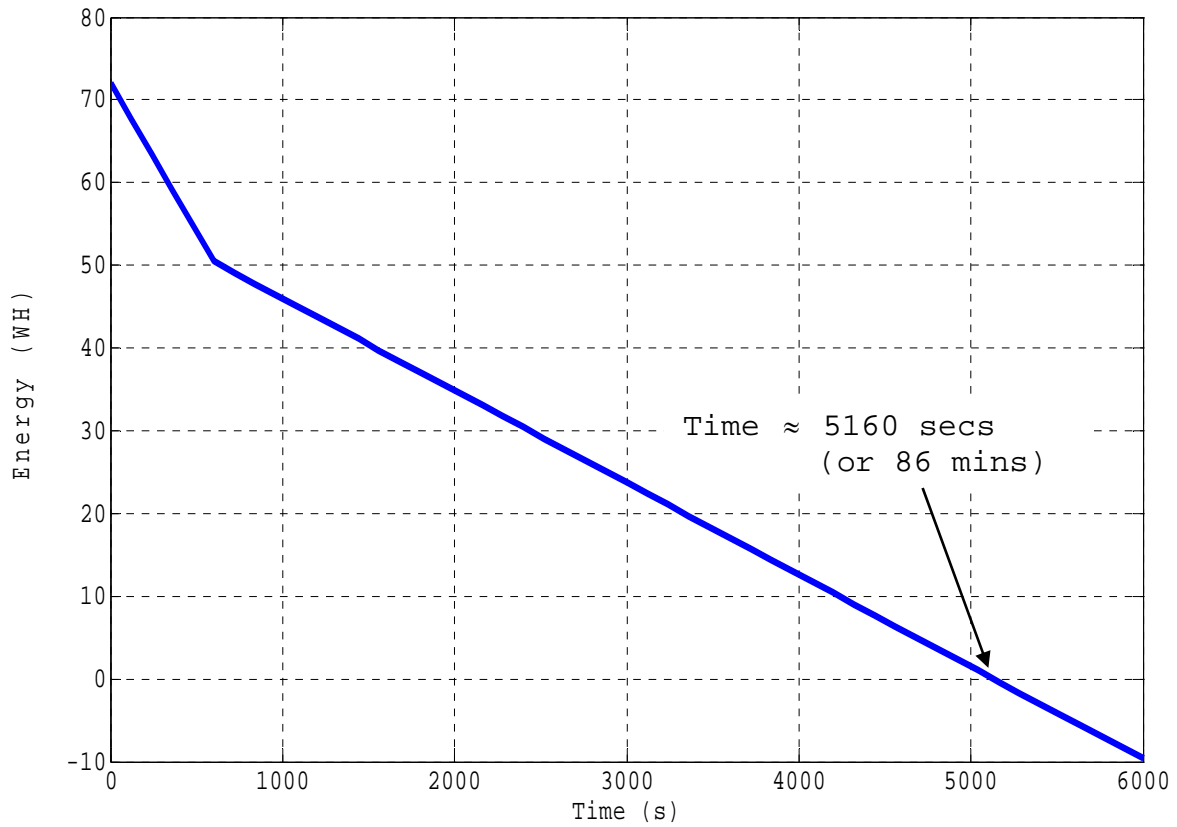


Figure 59. Simulation for battery energy consumption at throttle speed (100%-70%) without solar panel.

Table 18. Comparison between simulation results and actual flight endurance data [3] without solar panel incorporated.

Throttle Speed (%)	100%-55%	100%-65%	100%-70%
Actual endurance lasted with battery alone (minutes)	113	94	86
Simulation results with battery alone (minutes)	110	91	86
Difference in flight endurance (%)	2.65	3.20	0.00

It can be seen that the largest difference between the simulated results and actual flight endurance data is 3.20%, and this is considered acceptable for this thesis application. To further validate the accuracy of the simulation model, additional simulation tests will be conducted on the battery with solar panel configuration (including DC-to-DC power converter and MPPT) as explained in the following section.

2. Simulation Results Using Battery and Solar Panel

Using the Simulink model depicted in Figure 55, we conducted simulations utilizing the battery with solar panel configuration with constant output solar power of 12 W and 17 W at 55%, 65%, and 70% throttle speed settings. The resulting plots are shown from Figures 60 to 65, respectively. The simulated results and the actual findings [3] are tabulated in Table 19 for ease of comparison.

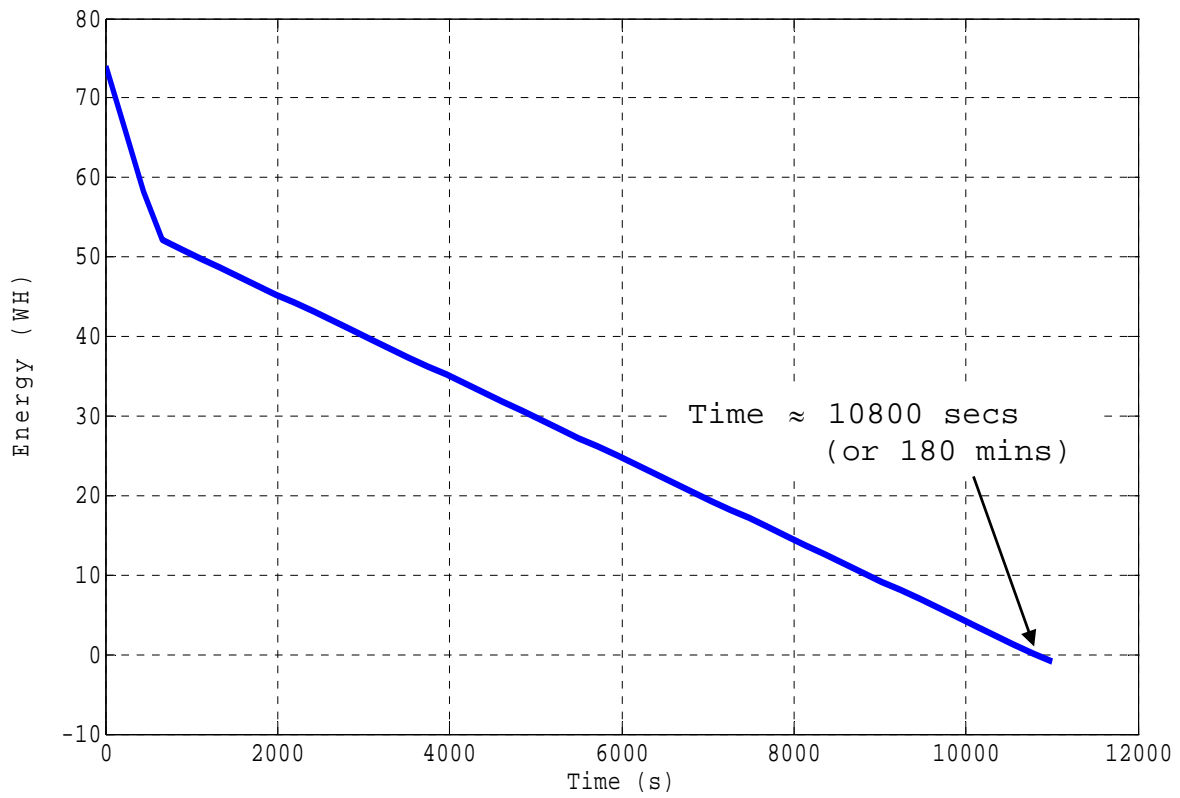


Figure 60. Simulation for battery energy consumption with solar panel (12 W) and MPPT at throttle speed (100%-55%).

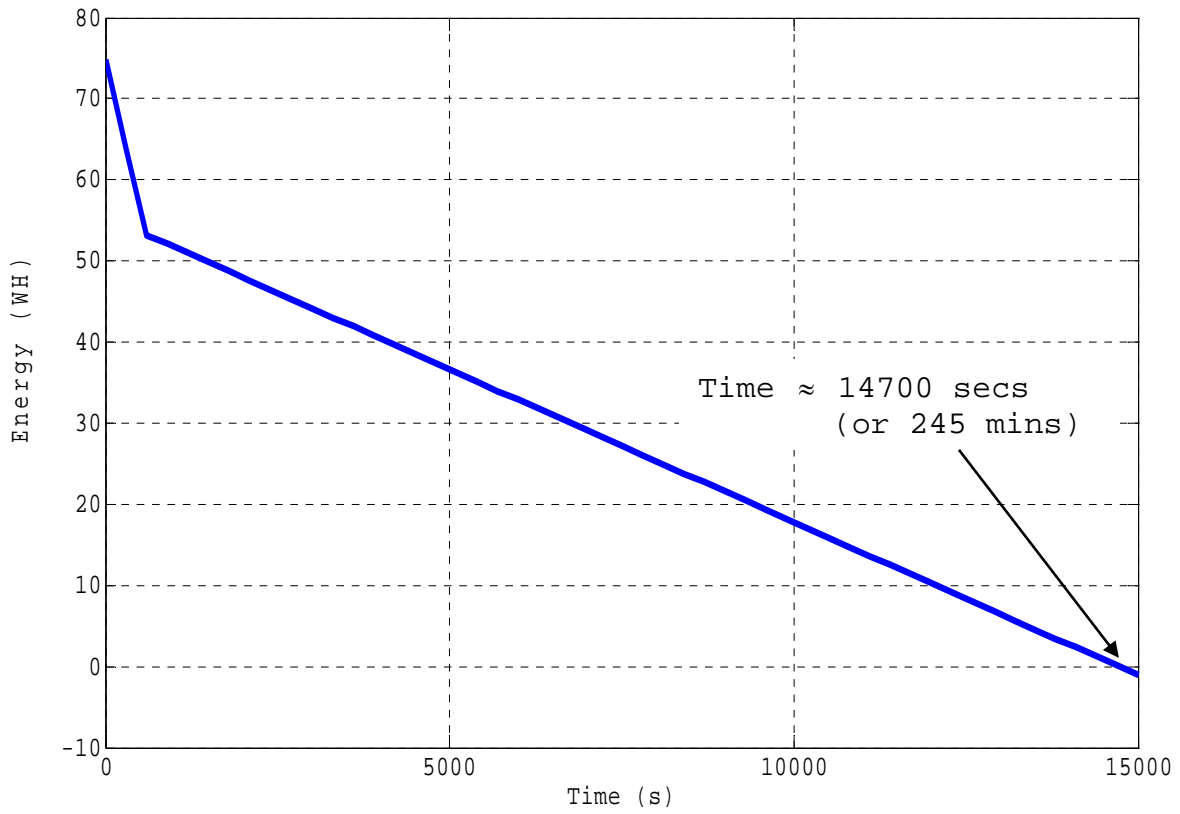


Figure 61. Simulation for battery energy consumption with solar panel (17 W) and MPPT at throttle speed (100%-55%).

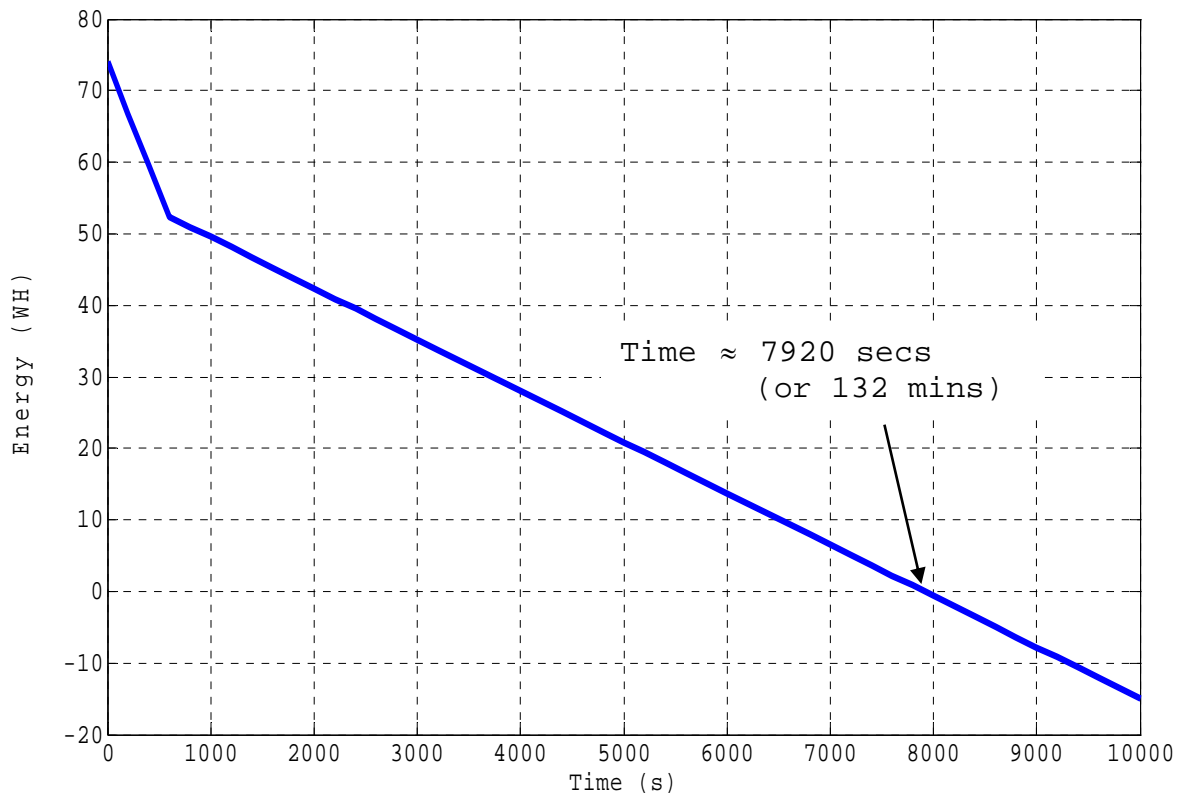


Figure 62. Simulation for battery energy consumption with solar panel (12 W) and MPPT at throttle speed (100%-65%).

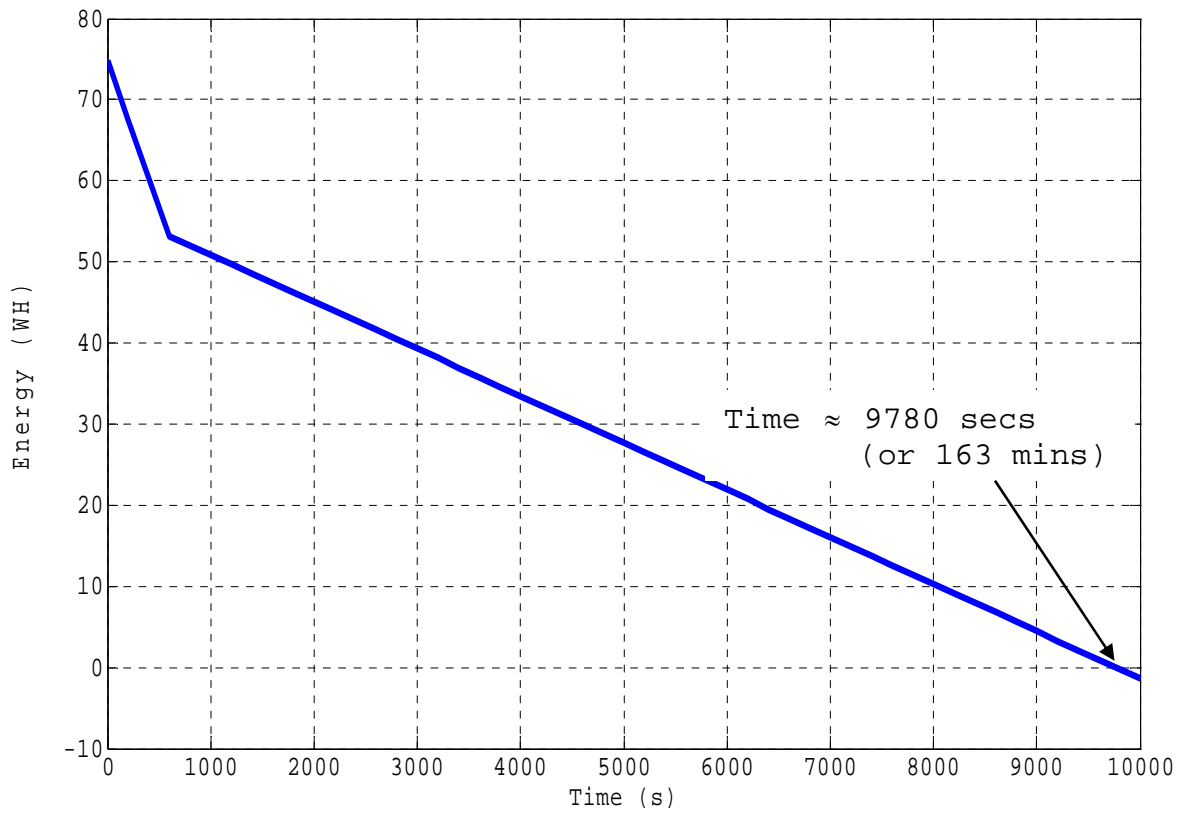


Figure 63. Simulation for battery energy consumption with solar panel (17 W) and MPPT at throttle speed (100%-65%).

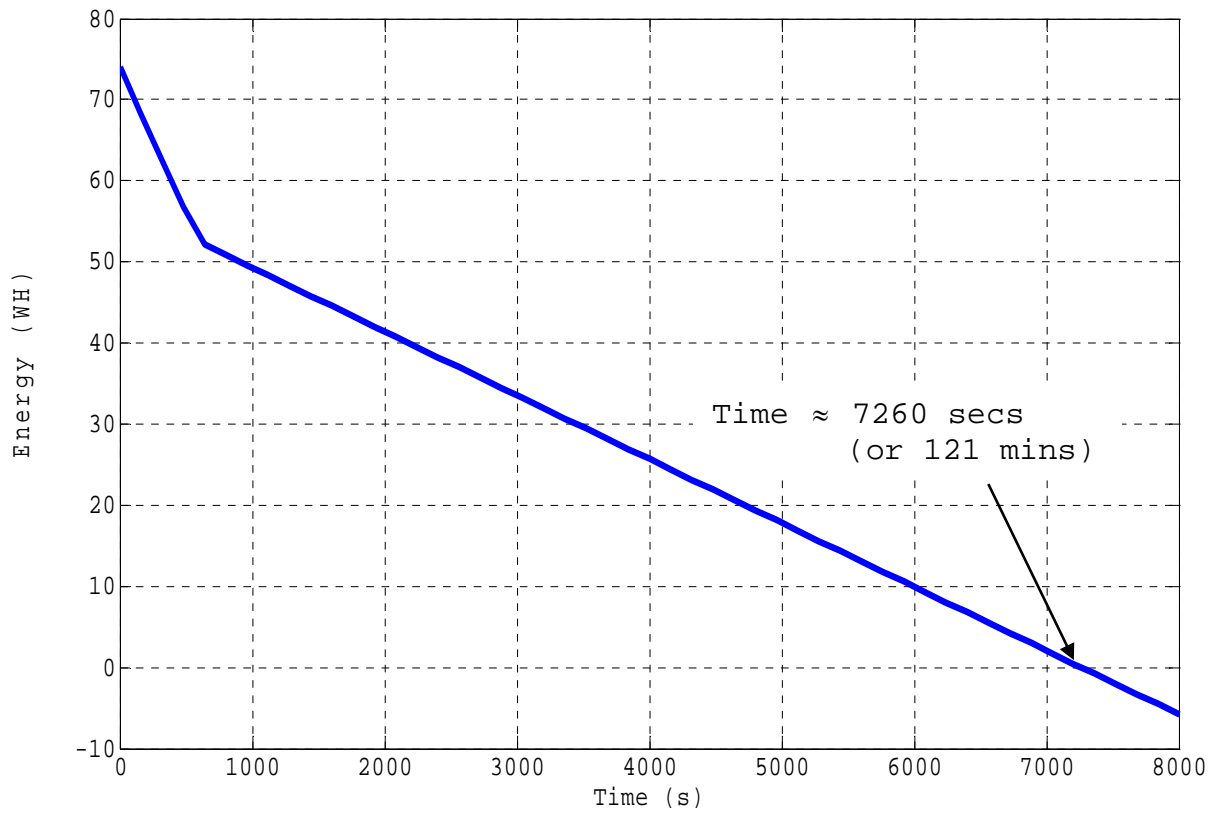


Figure 64. Simulation for battery energy consumption with solar panel (12 W) and MPPT at throttle speed (100%-70%).

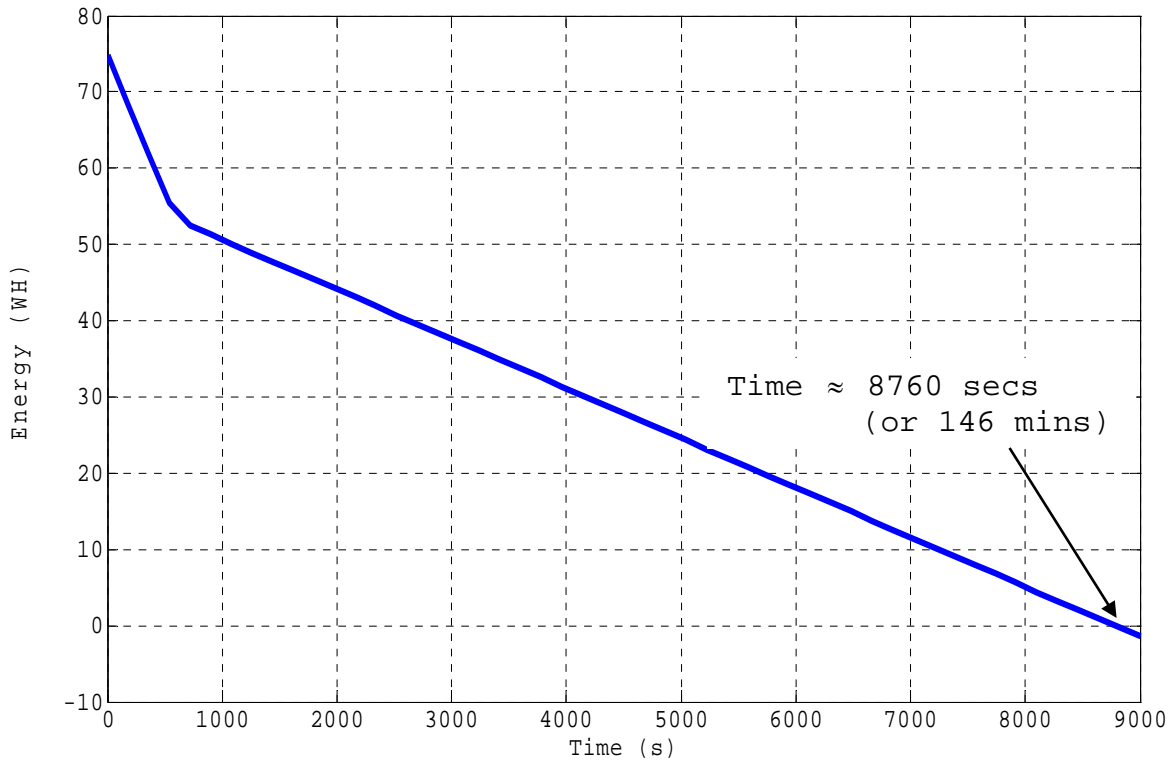


Figure 65. Simulation for battery energy consumption with solar panel (17 W) and MPPT at throttle speed (100%-70%).

Table 19. Comparison between simulation results and actual data [3] using battery and solar panel with MPPT.

Throttle Speed (%)	100%-55%	100%-65%	100%-70%
Actual endurance lasted with solar panel output power of 12 W (minutes)	180	132	121
Simulation results with solar panel output power of 12 W (minutes)	180	132	121
Difference in flight endurance (%)	0	0	0
Actual endurance lasted with solar panel output power of 17 W (minutes)	243	163	146
Simulation results with solar panel output power of 17 W (minutes)	245	163	146
Difference in flight endurance (%)	0.82	0	0

It is observed that the largest difference between the simulated results and actual flight endurance data is 0.82%, and this percentage difference is much lower compared to the previous result of 3.20%. Hence, in this case, it is safe to conclude that the Simulink models are highly accurate and suitable for this thesis application.

C. DETERMINATION OF AVERAGE ENERGY CONSUMED AT DIFFERENT THROTTLE SPEEDS

The data from [3] shown in Table 20 can be used to determine the throttle speed-equivalent resistance graph for the actual Raven mini-UAV. The plot for the throttle speed-equivalent resistance is shown in Figure 66.

Table 20. Throttle speed equivalent resistance. (After [3])

Throttle Speed	55%	65%	70%	100%
Average equivalent resistance	17.19	14.00	12.80	4.00

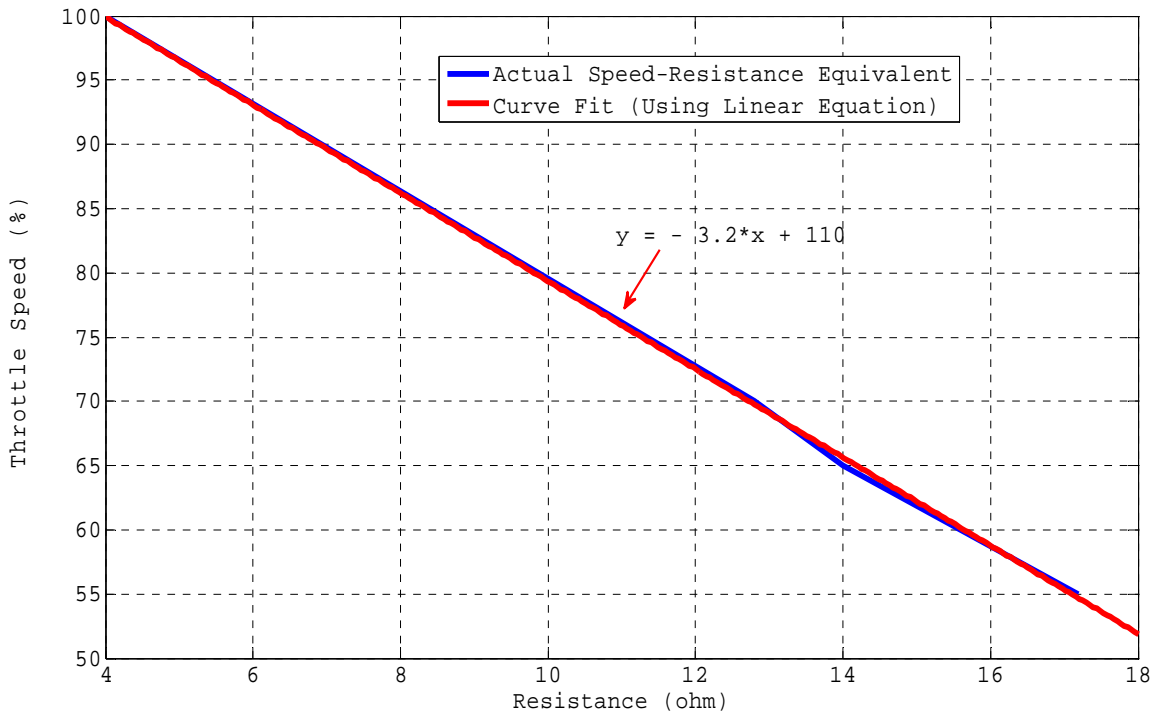


Figure 66. Raven mini-UAV throttle speed equivalent resistance.

From the measured throttle speed equivalent resistance data, an approximated straight line equation is obtained using Matlab tools. The resultant linearization is represented by the equation $y = -3.2x + 110$. The blue line represents the actual speed-equivalent resistance, while the red line represents the linearization.

With this equation, it is possible to estimate the equivalent load resistance at every throttle speed setting from 0% to 100%. With an average battery operating voltage of 22.9V (from [3]), the average battery capacity (AH) and battery energy capacity (WH) consumed at each throttle speed setting from 40% to 100% are determined and shown in Table 21.

Table 21. Average battery capacity (AH) and battery energy capacity (WH) consumption.

Throttle Speed	40%	45%	46%	47%	48%	49%	50%	51%	52%	53%	54%	55%
Average equivalent resistance (ohms)	21.88	20.31	20.00	19.69	19.38	19.06	18.75	18.44	18.13	17.81	17.50	17.19
Average battery operating voltage (V)	22.9											
Average operating current (A)	1.05	1.13	1.15	1.16	1.18	1.20	1.22	1.24	1.26	1.29	1.31	1.33
Average battery capacity (AH)	1.05	1.13	1.15	1.16	1.18	1.20	1.22	1.24	1.26	1.29	1.31	1.33
Average battery energy capacity (WH)	24.05	25.88	26.34	26.56	27.02	27.48	27.94	28.40	28.86	29.54	30.00	30.46
Throttle Speed	56%	57%	58%	59%	60%	61%	62%	63%	64%	65%	66%	67%
Average equivalent resistance (ohms)	16.88	16.56	16.25	15.94	15.63	15.31	15.00	14.69	14.38	14.06	13.75	13.44
Average battery operating voltage (V)	22.9											
Average operating current (A)	1.36	1.38	1.41	1.44	1.47	1.50	1.53	1.56	1.59	1.63	1.67	1.70
Average battery capacity (AH)	1.36	1.38	1.41	1.44	1.47	1.50	1.53	1.56	1.59	1.63	1.67	1.70
Average battery energy capacity (WH)	31.14	31.60	32.29	32.98	33.66	34.35	35.04	35.72	36.41	37.33	38.24	38.93

Throttle Speed	68%	69%	70%	71%	72%	73%	74%	75%	76%	77%	78%
Average equivalent resistance (ohms)	13.13	12.81	12.50	12.19	11.88	11.56	11.25	10.94	10.63	10.31	10.00
Average battery operating voltage (V)	22.9										
Average operating current (A)	1.74	1.79	1.83	1.88	1.93	1.98	2.04	2.09	2.15	2.22	2.29
Average battery capacity (AH)	1.74	1.79	1.83	1.88	1.93	1.98	2.04	2.09	2.15	2.22	2.29
Average battery energy capacity (WH)	39.85	41.00	41.91	43.05	44.20	45.34	46.72	47.86	49.24	50.84	52.44
Throttle Speed	79%	80%	81%	82%	83%	84%	85%	86%	87%	88%	89%
Average equivalent resistance (ohms)	9.69	9.38	7.81	6.25	4.69	3.13	7.81	7.5	7.19	6.88	6.56
Average battery operating voltage (V)	22.9										
Average operating current (A)	2.36	2.44	2.93	3.66	4.88	7.32	2.93	3.05	3.18	3.33	3.49
Average battery capacity (AH)	2.36	2.44	2.93	3.66	4.88	7.32	2.93	3.05	3.18	3.33	3.49
Average battery energy capacity (WH)	54.04	55.88	67.10	83.81	111.75	167.63	67.10	69.85	72.82	76.26	79.92
Throttle Speed	90%	91%	92%	93%	94%	95%	96	97	98	99	100%
Average equivalent resistance (ohms)	6.25	5.94	5.63	5.31	5.00	4.69	4.38	4.06	3.75	3.44	3.13
Average battery operating voltage (V)	22.9										
Average operating current (A)	3.66	3.86	4.07	4.31	4.58	4.88	5.23	5.64	6.11	6.66	7.32
Average battery capacity (AH)	3.66	3.86	4.07	4.31	4.58	4.88	5.23	5.64	6.11	6.66	7.32
Average battery energy capacity (WH)	83.81	88.39	93.20	98.70	104.88	111.75	119.77	129.16	139.92	152.51	167.63

D. SIMULATION TEST FOR FINAL SOLAR ARRAY

The basic simulation model shown in Figure 55 was enhanced to include multiple simultaneous simulations at specific throttle speed setting. The enhanced simulation model shown in Figure 67 is capable of predicting the overall flight endurance at three different output powers from the solar array based on different cell efficiencies.

Simulation results for the overall flight endurance plot with no power output from the solar array are depicted in Section 1 of Figure 67. The overall flight endurance with a net power output of 32.44 W (upper range), 40 W (actual output power from solar array), and 18.11 W (lower range), respectively, are simulated in Sections 2, 3 and 4. The net output powers used for these simulations are computed and shown in Table 22 below.

Table 22. Computation of output power for simulation.

Solar Panel Surface Area (cm ²)	Ave. Output Power (W) with Assuming 98% MPPT Efficiency	Remarks
3360 cm ²	$40.80 \times 0.98 = 40.0 \text{ W}$	Final solar array output power
3360 cm ²	$336 \times 0.0985 \times 0.98 = 32.44 \text{ W}$	Upper range output power
3360 cm ²	$336 \times 0.055 \times 0.98 = 18.11 \text{ W}$	Lower range output power

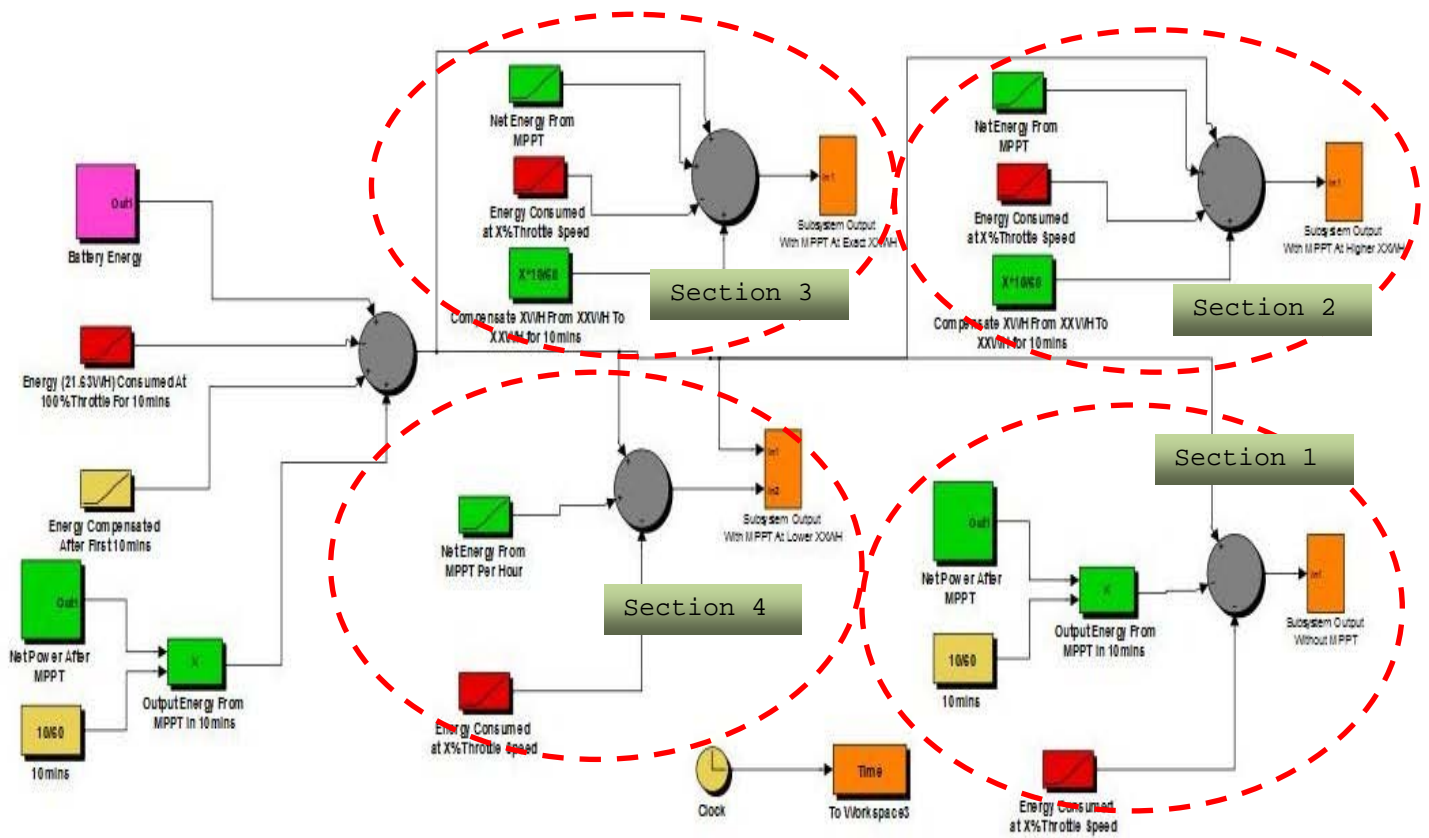


Figure 67. Enhanced simulation model with and without solar array.

The plots of each specific throttle speed setting for simulation starting from 40% to 100% at an interval of 5% are shown from Figures 68 to 80, respectively. The simulation results show that with a constant output power of 32.44 W or greater from the solar array, the battery energy capacity remains at full capacity when the UAV is operated below the 60% throttle speed setting.

1. Simulation for Battery Energy Consumption with and without Solar Array at Throttle Speed (100% - 40%)

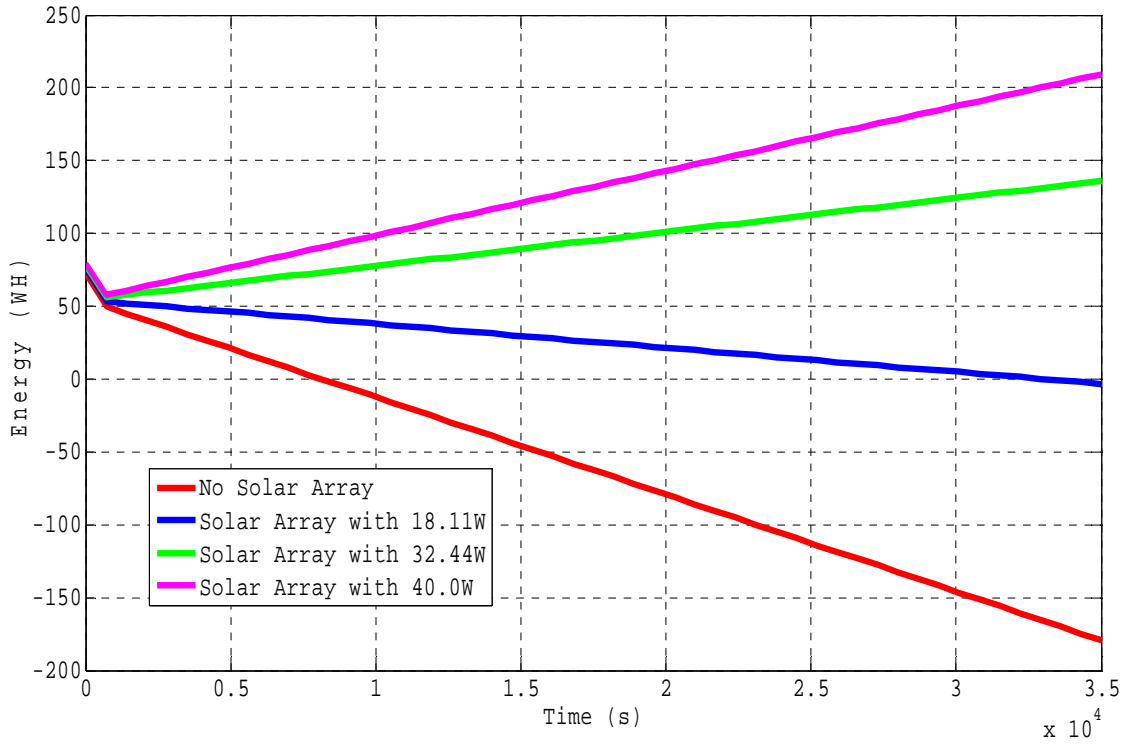


Figure 68. Simulation for battery energy consumption with and without solar array at throttle speed (100% - 40%).

The estimated flight endurance at 100% (first ten minutes) and 40% throttle speed setting for the respective output power from the solar array is shown in Table 23.

Table 23. Simulated flight endurance results at throttle speed (100% - 40%).

Throttle Speed	40%
Flight endurance without solar array (minutes)	135.9
Flight endurance with solar array output power of 18.11 W (minutes)	550.1
Flight endurance with solar array output power of 32.44 W (minutes)	∞
Flight endurance with solar array output power of 40 W (minutes)	∞

2. Simulation for Battery Energy Consumption with and without Solar Array at Throttle Speed (100% - 45%)

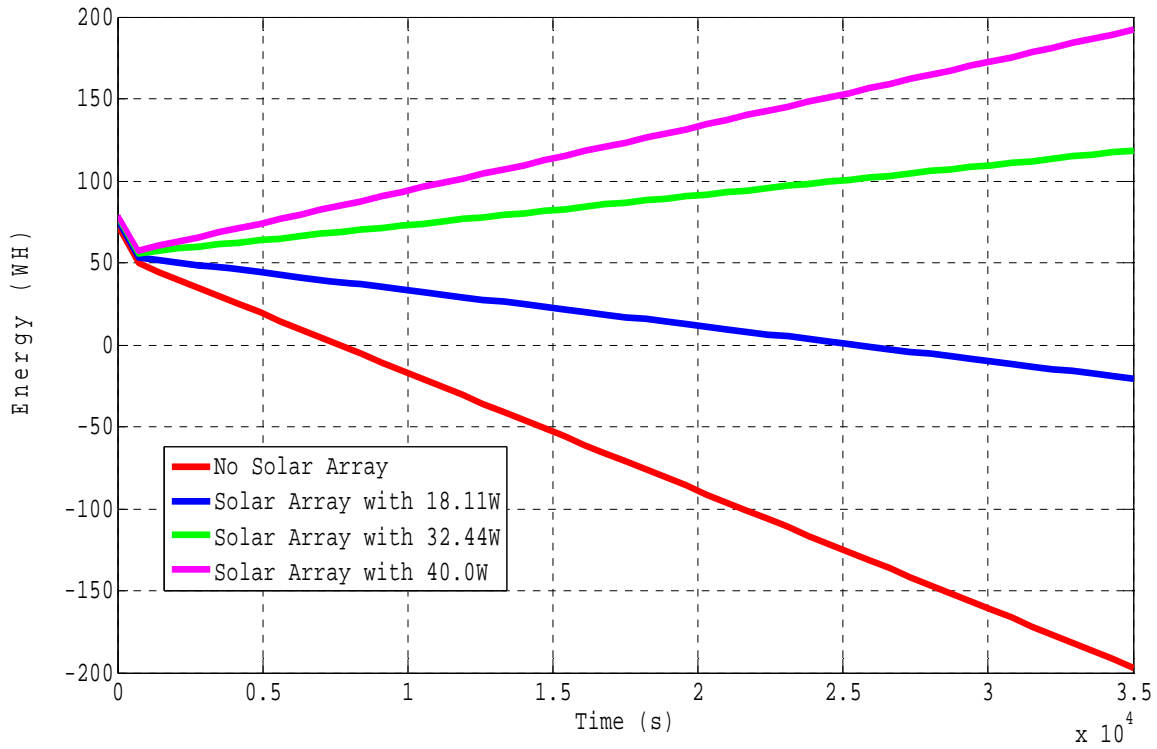


Figure 69. Simulation for battery energy consumption with and without solar array at throttle speed (100%-45%).

The estimated flight endurance at 100% (first ten minutes) and 45% throttle speed setting for the respective output power from the solar array is shown in Table 24.

Table 24. Simulation flight endurance results at throttle speed (100% - 45%).

Throttle Speed	45%
Flight endurance without solar array (minutes)	127.0
Flight endurance with solar array output power of 18.11 W (minutes)	422.9
Flight endurance with solar array output power of 32.44 W (minutes)	∞
Flight endurance with solar array output power of 40 W (minutes)	∞

3. Simulation for Battery Energy Consumption with and without Solar Array at Throttle Speed (100% - 50%)

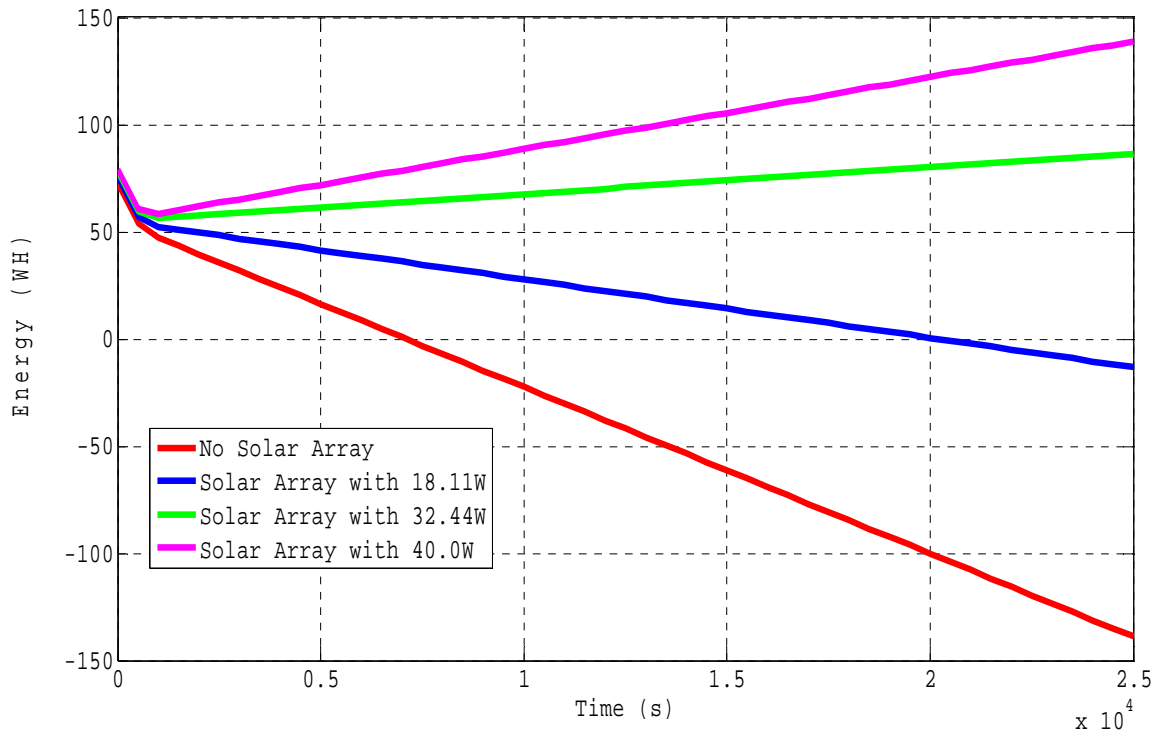


Figure 70. Simulation for battery energy consumption with and without solar array at throttle speed (100%-50%).

The estimated flight endurance at 100% (first ten minutes) and 50% throttle speed setting for the respective output power from the solar array is shown in Table 25.

Table 25. Simulation flight endurance results at throttle speed (100% - 50%).

Throttle Speed	50%
Flight endurance without solar array (minutes)	118.3
Flight endurance with solar array output power of 18.11 W (minutes)	336.4
Flight endurance with solar array output power of 32.44 W (minutes)	∞
Flight endurance with solar array output power of 40 W (minutes)	∞

4. Simulation for Battery Energy Consumption with and without Solar Array at Throttle Speed (100% - 55%)

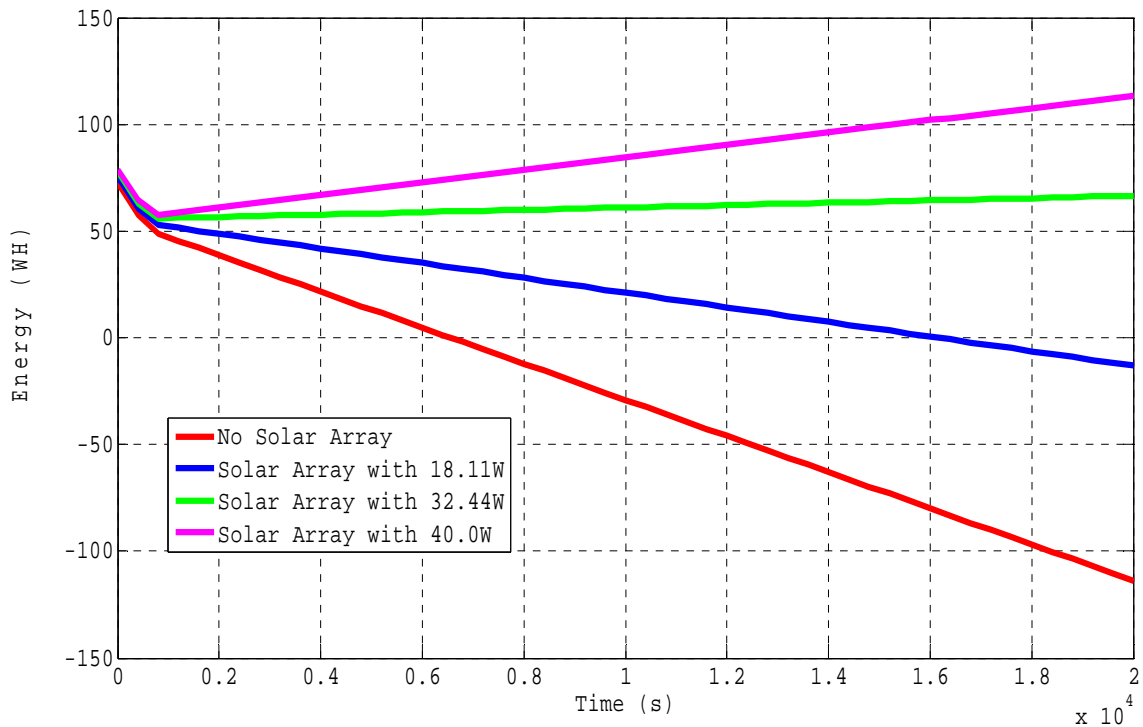


Figure 71. Simulation for battery energy consumption with and without solar array at throttle speed (100%-55%).

The estimated flight endurance at 100% (first ten minutes) and 55% throttle speed setting for the respective output power from the solar array is shown in Table 26.

Table 26. Simulation flight endurance results at throttle speed (100% - 55%).

Throttle Speed	55%
Flight endurance without solar array (minutes)	109.4
Flight endurance with solar array output power of 18.11 W (minutes)	269.8
Flight endurance with solar array output power of 32.44 W (minutes)	∞
Flight endurance with solar array output power of 40 W (minutes)	∞

5. Simulation for Battery Energy Consumption with and without Solar Array at Throttle Speed (100% - 60%)

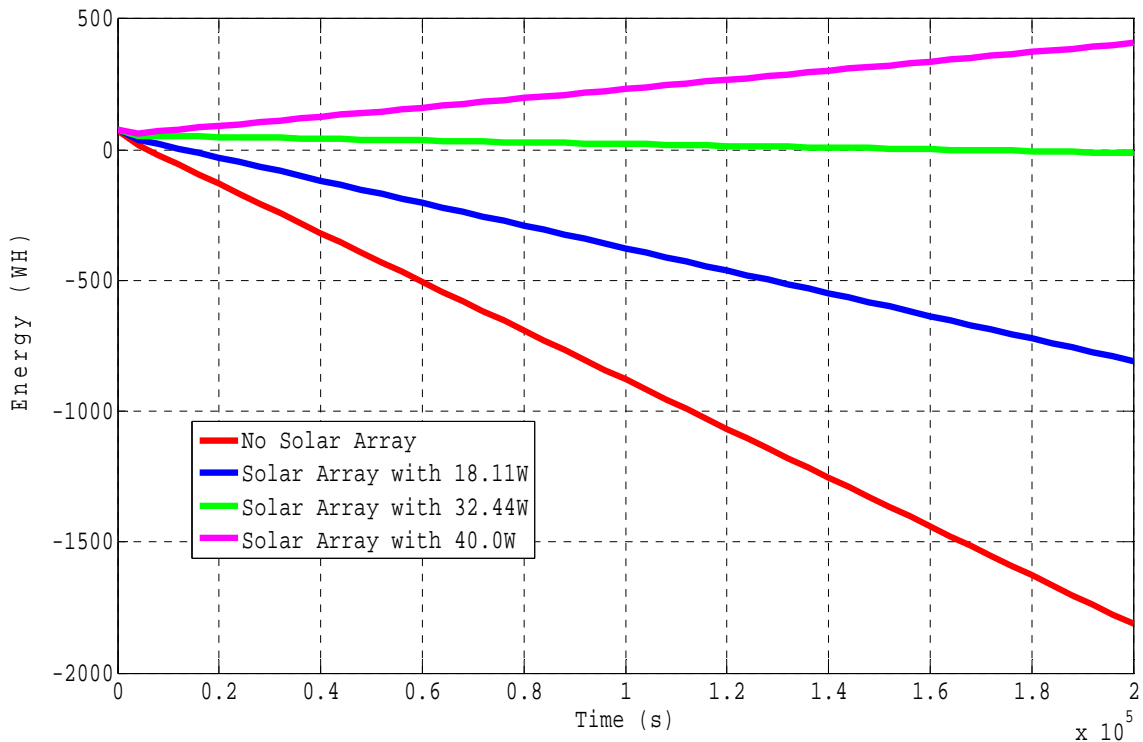


Figure 72. Simulation for battery energy consumption with and without solar array at throttle speed (100%-60%).

The estimated flight endurance at 100% (first ten minutes) and 60% throttle speed setting for the respective output power from the solar array is shown in Table 27.

Table 27. Simulation flight endurance results at throttle speed (100% - 60%).

Throttle Speed	60%
Flight endurance without solar array (minutes)	99.9
Flight endurance with solar array output power of 18.11 W (minutes)	216.3
Flight endurance with solar array output power of 32.44 W (minutes)	2750.0
Flight endurance with solar array output power of 40 W (minutes)	∞

6. Simulation for Battery Energy Consumption with and without Solar Array at Throttle Speed (100% - 65%)

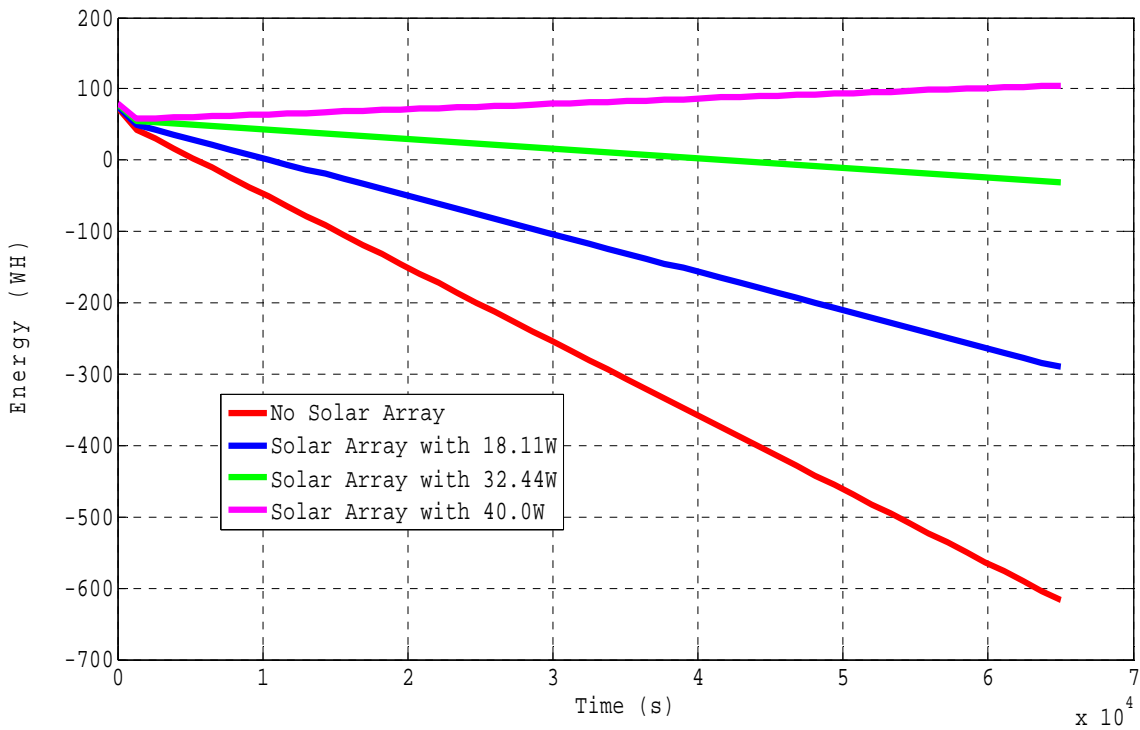


Figure 73. Simulation for battery energy consumption with and without solar array at throttle speed (100%-65%).

The estimated flight endurance at 100% (first ten minutes) and 65% throttle speed setting for the respective output power from the solar array is shown in Table 28.

Table 28. Simulation flight endurance results at throttle speed (100% - 65%).

Throttle Speed	65%
Flight endurance without solar array (minutes)	91.1
Flight endurance with solar array output power of 18.11 W (minutes)	176.9
Flight endurance with solar array output power of 32.44 W (minutes)	695.4
Flight endurance with solar array output power of 40 W (minutes)	∞

7. Simulation for Battery Energy Consumption with and without Solar Array at Throttle Speed (100% - 70%)

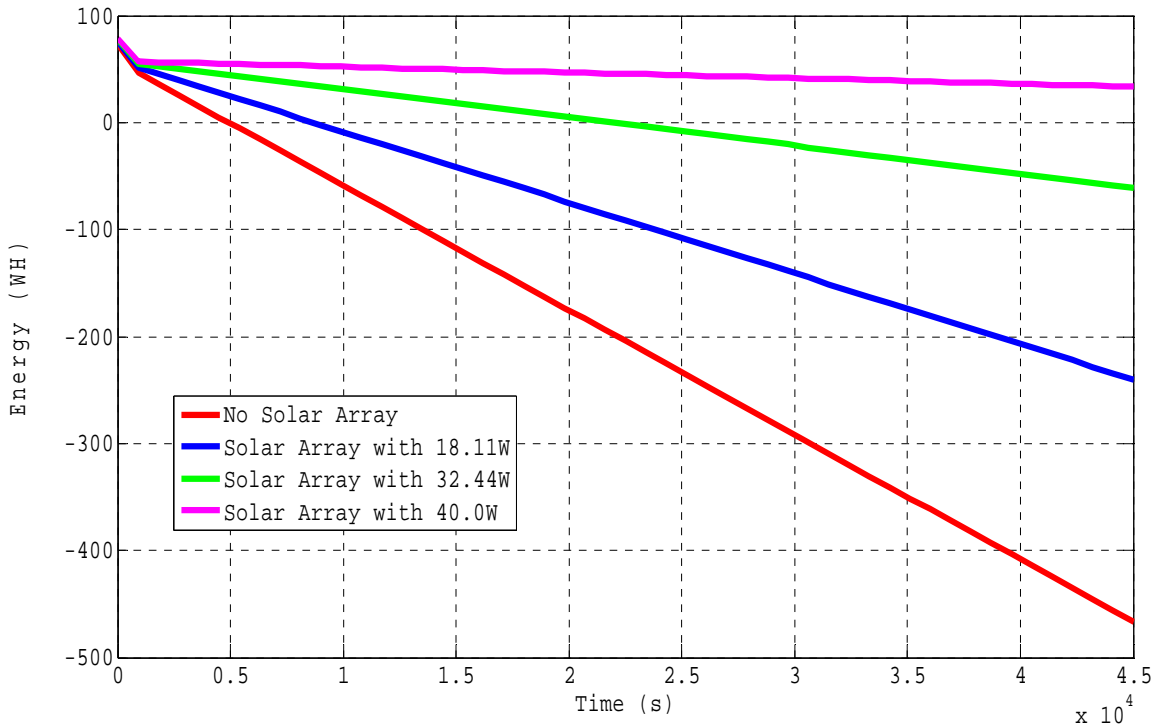


Figure 74. Simulation for battery energy consumption with and without solar array at throttle speed (100%-70%).

The estimated flight endurance at 100% (first ten minutes) and 70% throttle speed setting for the respective output power from the solar array is shown in Table 29.

Table 29. Simulation flight endurance results at throttle speed (100% - 70%).

Throttle Speed	70%
Flight endurance without solar array (minutes)	82.2
Flight endurance with solar array output power of 18.11 W (minutes)	144.8
Flight endurance with solar array output power of 32.44 W (minutes)	363.9
Flight endurance with solar array output power of 40 W (minutes)	∞

8. Simulation for Battery Energy Consumption with and without Solar Array at Throttle Speed (100% - 75%)

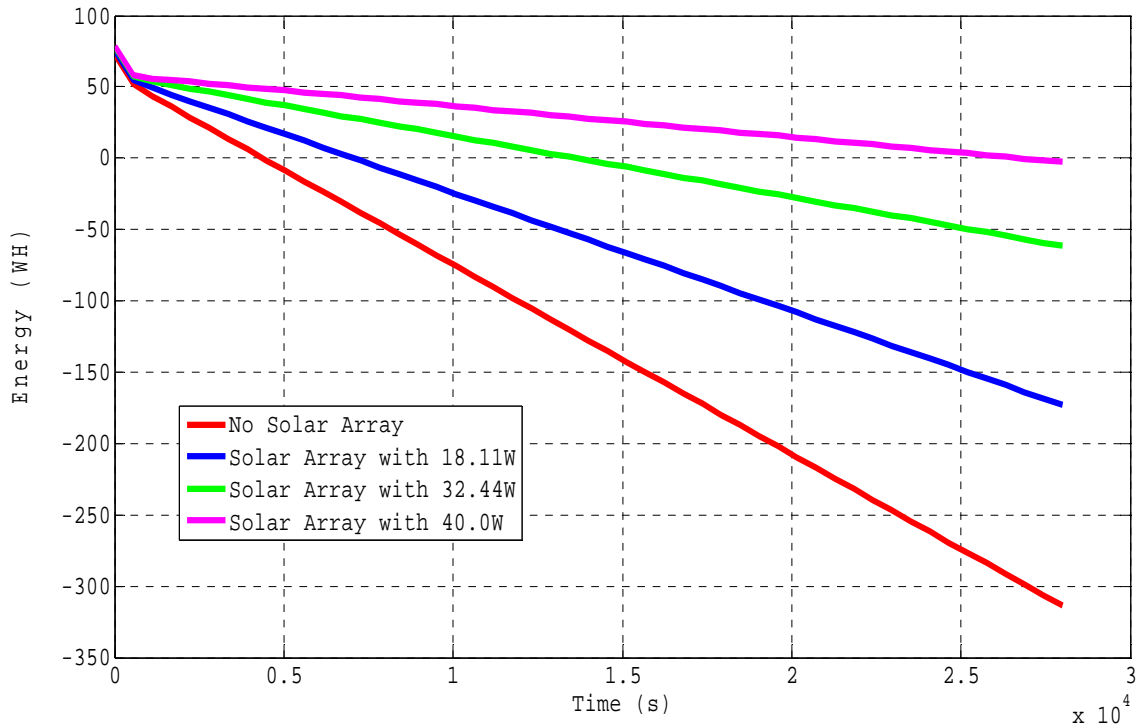


Figure 75. Simulation for battery energy consumption with and without solar array at throttle speed (100%-75%).

The estimated flight endurance at 100% (first ten minutes) and 75% throttle speed setting for the respective output power from the solar array is shown in Table 30.

Table 30. Simulation flight endurance results at throttle speed (100% - 75%).

Throttle Speed	75%
Flight endurance without solar array (minutes)	73.2
Flight endurance with solar array output power of 18.11 W (minutes)	117.8
Flight endurance with solar array output power of 32.44 W (minutes)	227.4
Flight endurance with solar array output power of 40 W (minutes)	446.0

9. Simulation for Battery Energy Consumption with and without Solar Array at Throttle Speed (100% - 80%)

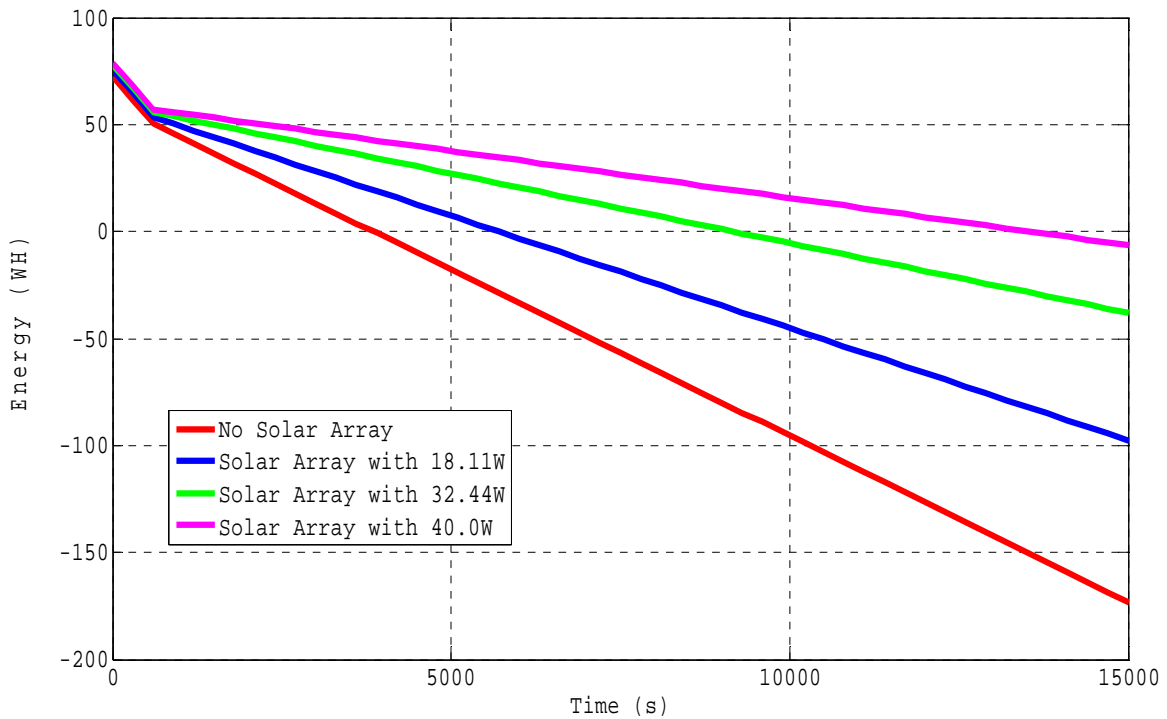


Figure 76. Simulation for battery energy consumption with and without solar array at throttle speed (100%-80%).

The estimated flight endurance at 100% (first ten minutes) and 80% throttle speed setting for the respective output power from the solar array is shown in Table 31.

Table 31. Simulation flight endurance results at throttle speed (100% - 80%).

Throttle Speed	80%
Flight endurance without solar array (minutes)	64.2
Flight endurance with solar array output power of 18.11 W (minutes)	94.9
Flight endurance with solar array output power of 32.44 W (minutes)	153.0
Flight endurance with solar array output power of 40 W (minutes)	225.8

10. Simulation for Battery Energy Consumption with and without Solar Array at Throttle Speed (100% - 85%)

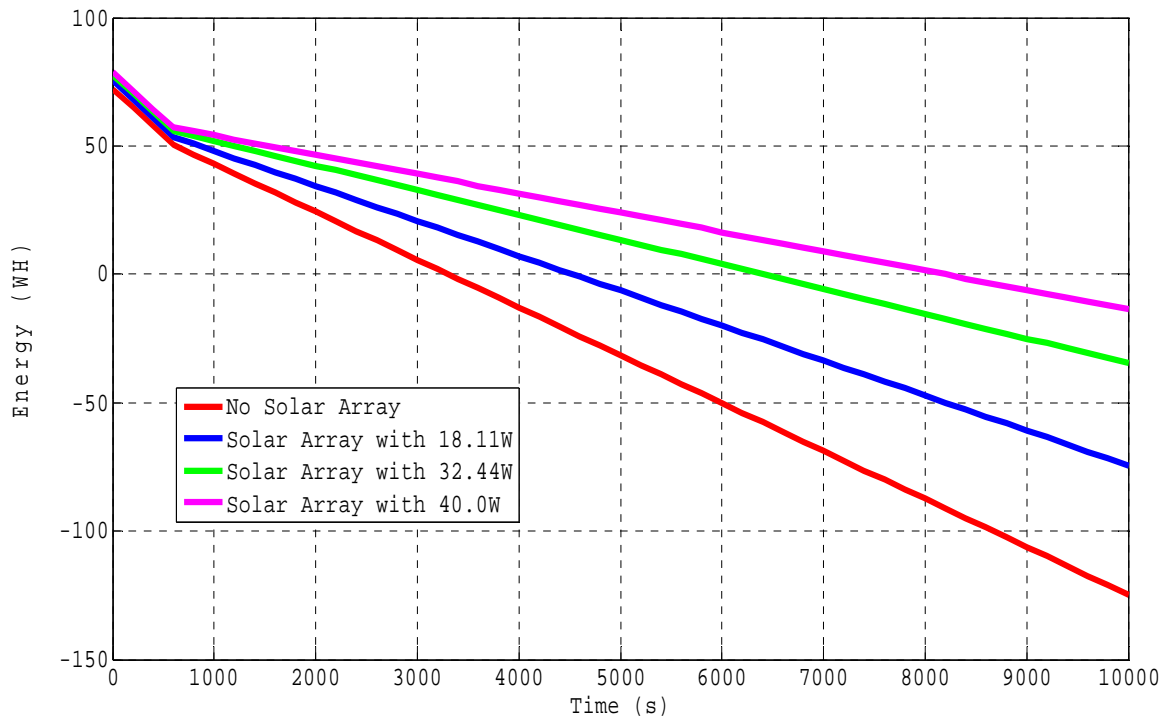


Figure 77. Simulation for battery energy consumption with and without solar array at throttle speed (100%-85%).

The estimated flight endurance at 100% (first ten minutes) and 85% throttle speed setting for the respective output power from the solar array is shown in Table 32.

Table 32. Simulation flight endurance results at throttle speed (100% - 85%).

Throttle Speed	85%
Flight endurance without solar array (minutes)	55.1
Flight endurance with solar array output power of 18.11 W (minutes)	75.4
Flight endurance with solar array output power of 32.44 W (minutes)	106.7
Flight endurance with solar array output power of 40 W (minutes)	136.5

11. Simulation for Battery Energy Consumption with and without Solar Array at Throttle Speed (100% - 90%)

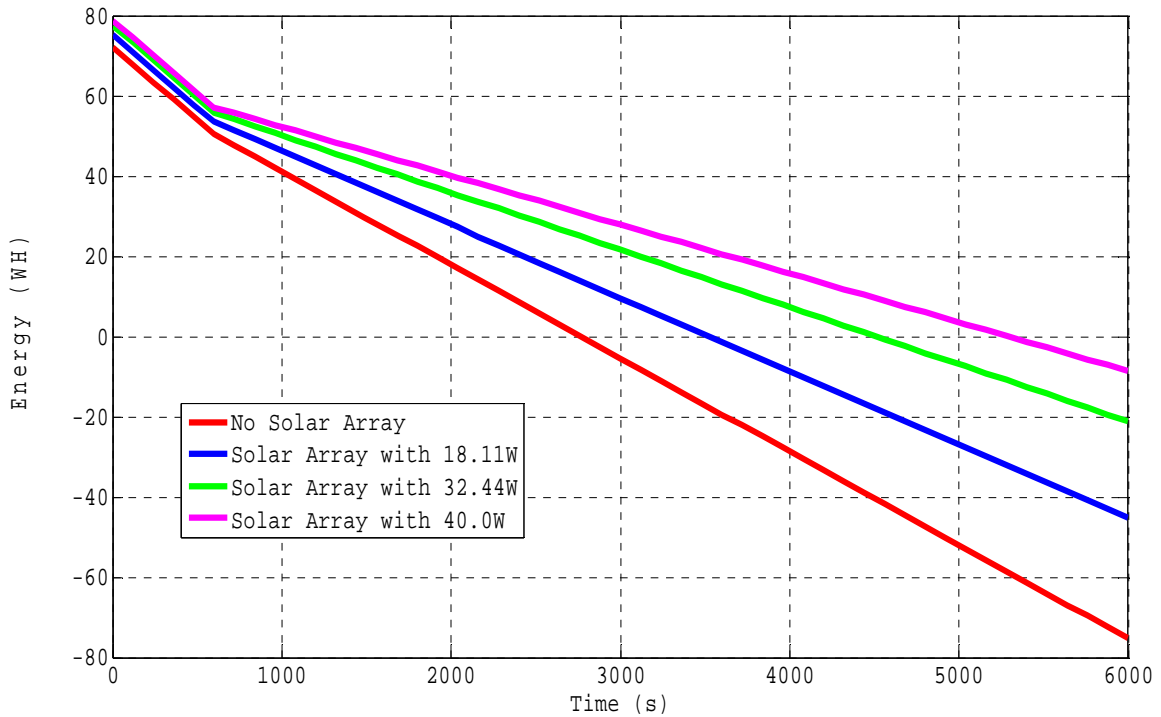


Figure 78. Simulation for battery energy consumption with and without solar array at throttle speed (100%-90%).

The estimated flight endurance at 100% (first ten minutes) and 90% throttle speed setting for the respective output power from the solar array is shown in Table 33.

Table 33. Simulation flight endurance results at throttle speed (100% - 90%).

Throttle Speed	90%
Flight endurance without solar array (minutes)	46.1
Flight endurance with solar array output power of 18.11 W (minutes)	58.8
Flight endurance with solar array output power of 32.44 W (minutes)	75.2
Flight endurance with solar array output power of 40 W (minutes)	88.2

12. Simulation for Battery Energy Consumption with and without Solar Array at Throttle Speed (100% - 95%)

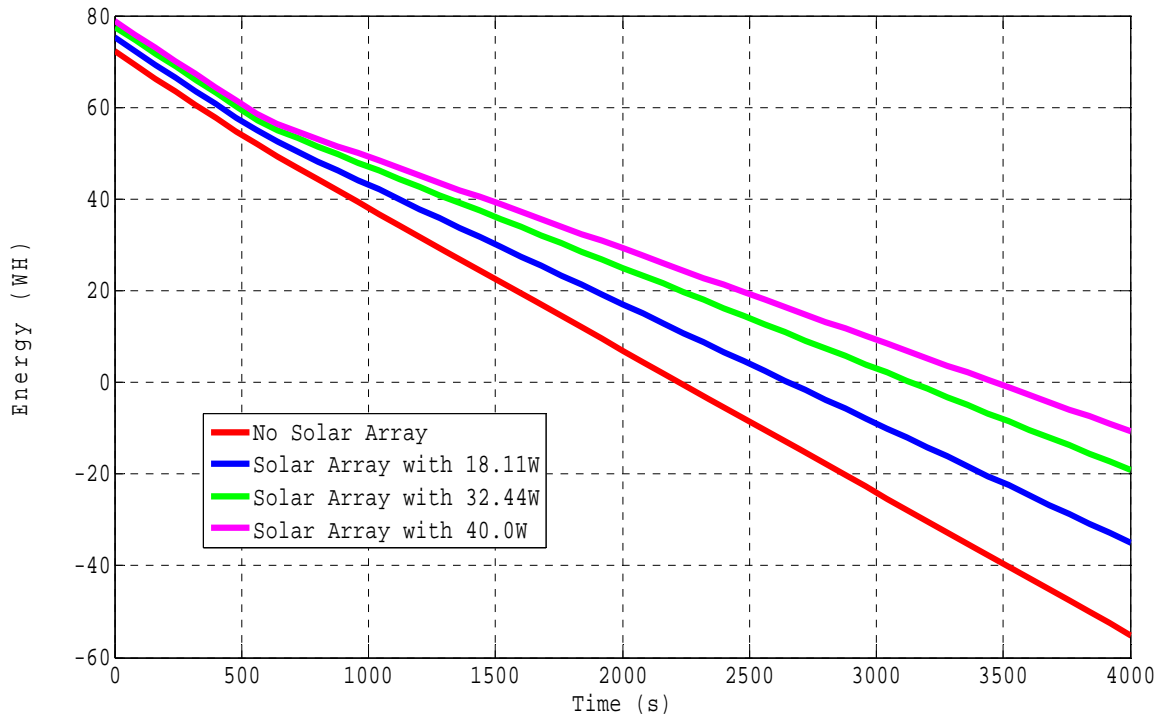


Figure 79. Simulation for battery energy consumption with and without solar array at throttle speed (100%-95%).

The estimated flight endurance at 100% (first ten minutes) and 95% throttle speed setting for the respective output power from the solar array is shown in Table 34.

Table 34. Simulation flight endurance results at throttle speed (100% - 95%).

Throttle Speed	95%
Flight endurance without solar array (minutes)	37.1
Flight endurance with solar array output power of 18.11 W (minutes)	44.3
Flight endurance with solar array output power of 32.44 W (minutes)	52.3
Flight endurance with solar array output power of 40 W (minutes)	57.8

13. Simulation for Battery Energy Consumption with and without Solar Array at Throttle Speed (100%)

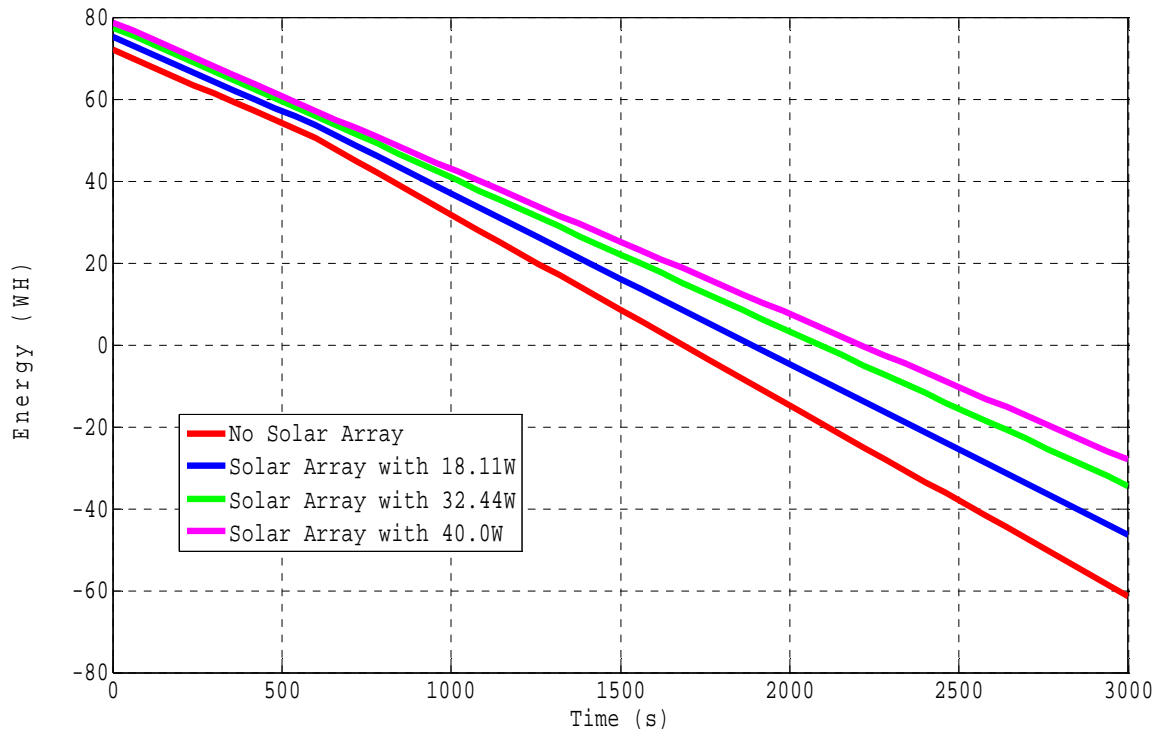


Figure 80. Simulation for battery energy consumption with and without solar array at throttle speed (100%).

The estimated flight endurance at full 100% throttle speed setting for the respective output power from the solar array is shown in Table 35.

Table 35. Simulation flight endurance results at throttle speed (100%).

Throttle Speed	100%
Flight endurance without solar array (minutes)	28.0
Flight endurance with solar array output power of 18.11 W (minutes)	31.4
Flight endurance with solar array output power of 32.44 W (minutes)	34.8
Flight endurance with solar array output power of 40 W (minutes)	36.8

The simulated flight results for the entire range of throttle speed settings, from 40% to 100%, are summarized in Table 36.

Normalized equivalent flight equations are further developed (using Simulink) to estimate the total flight endurance for the following configurations (i) without solar array, (ii) solar array incorporated with an output power of 18.11 W, (iii) solar array incorporated with an output power of 32.44 W, and (iv) solar array incorporated with an output power of 40 W. The respective plots are shown in Figures 81 to 84.

Table 36. Simulation flight endurance results—with and without solar array incorporated.

Throttle Speed	40%	45%	46%	47%	48%	49%	50%	51%	52%	53%	54%
Simulation results without solar array (minutes)	135.9	127.0	124.9	124.0	122.0	120.2	118.3	116.6	114.9	112.5	110.9
Simulation results with solar array output power of 18.11 W (minutes)	550.1	422.9	399.8	389.7	370.1	352.4	336.4	321.8	308.4	290.7	279.8
Simulation results with solar array output power of 32.44 W (minutes)	∞	∞	∞	∞	∞	∞	∞	∞	∞	∞	∞
Simulation results with solar array output power of 40.0 W (minutes)	∞	∞	∞	∞	∞	∞	∞	∞	∞	∞	∞
Throttle Speed	55%	56%	57%	58%	59%	60%	61%	62%	63%	64%	65%
Simulation results without solar array (minutes)	109.4	107.2	105.8	103.7	101.8	99.9	98.1	96.4	94.7	93.1	91.1
Simulation results with solar array output power of 18.11 W (minutes)	269.8	256.2	247.8	236.2	225.8	216.3	207.6	199.5	192.2	186.3	176.9
Simulation results with solar array output power of 32.44 W (minutes)	∞	∞	∞	∞	∞	2750.0	1764.7	1299.0	1031.8	854.2	695.4
Simulation results with solar array output power of 40.0 W (minutes)	∞	∞	∞	∞	∞	∞	∞	∞	∞	∞	∞

Throttle Speed	66%	67%	68	69	70%	71%	72%	73%	74%	75%	76%	77%
Simulation results without solar array (minutes)	89.2	87.8	86.0	83.8	82.2	80.3	78.5	76.8	74.8	73.2	71.5	69.5
Simulation results with solar array output power of 18.11 W (minutes)	169.4	164.1	157.6	150.2	144.8	138.6	133.0	127.8	122.1	117.8	113.1	108.0
Simulation results with solar array output power of 32.44 W (minutes)	587.8	526.4	462.3	401.5	363.9	325.9	295.0	269.8	244.7	227.4	209.5	192.2
Simulation results with solar array output power of 40.0 W (minutes)	∞	∞	∞	∞	∞	1133.6	825.9	651.8	520.0	446.0	380.9	326.2
Throttle Speed	78%	79%	80%	81%	82%	83%	84%	85%	86%	87%	88%	89%
Simulation results without solar array (minutes)	67.7	66.0	64.2	62.2	60.5	58.8	56.9	55.1	53.3	51.6	49.7	47.8
Simulation results with solar array output power of 18.11 W (minutes)	103.4	99.3	94.9	90.5	86.6	83.0	79.0	75.4	72.0	68.6	65.2	61.8
Simulation results with solar array output power of 32.44 W (minutes)	177.6	165.2	153.0	141.4	131.6	123.2	114.3	106.7	99.6	92.3	86.5	80.5
Simulation results with solar array output power of 40.0 W (minutes)	285.5	254.1	225.8	201.0	181.4	165.3	149.4	136.5	124.8	114.4	104.5	95.7

Throttle Speed	90%	91%	92%	93%	94%	95%	96%	97%	98%	99%	100%
Simulation results without solar array (minutes)	46.1	44.2	42.5	40.7	38.9	37.1	35.3	33.4	31.6	29.8	28.0
Simulation results with solar array output power of 18.11 W (minutes)	58.8	55.6	52.7	49.8	47.0	44.3	41.6	38.9	36.3	33.9	31.4
Simulation results with solar array output power of 32.44 W (minutes)	75.2	69.9	65.2	60.6	56.3	52.3	48.4	44.7	41.2	37.9	34.8
Simulation results with solar array output power of 40.0 W (minutes)	88.2	80.8	74.4	68.4	62.8	57.8	53.0	48.4	44.3	40.5	36.8

**14. General Equation Associated with Flight Endurance
(without Solar Array)**

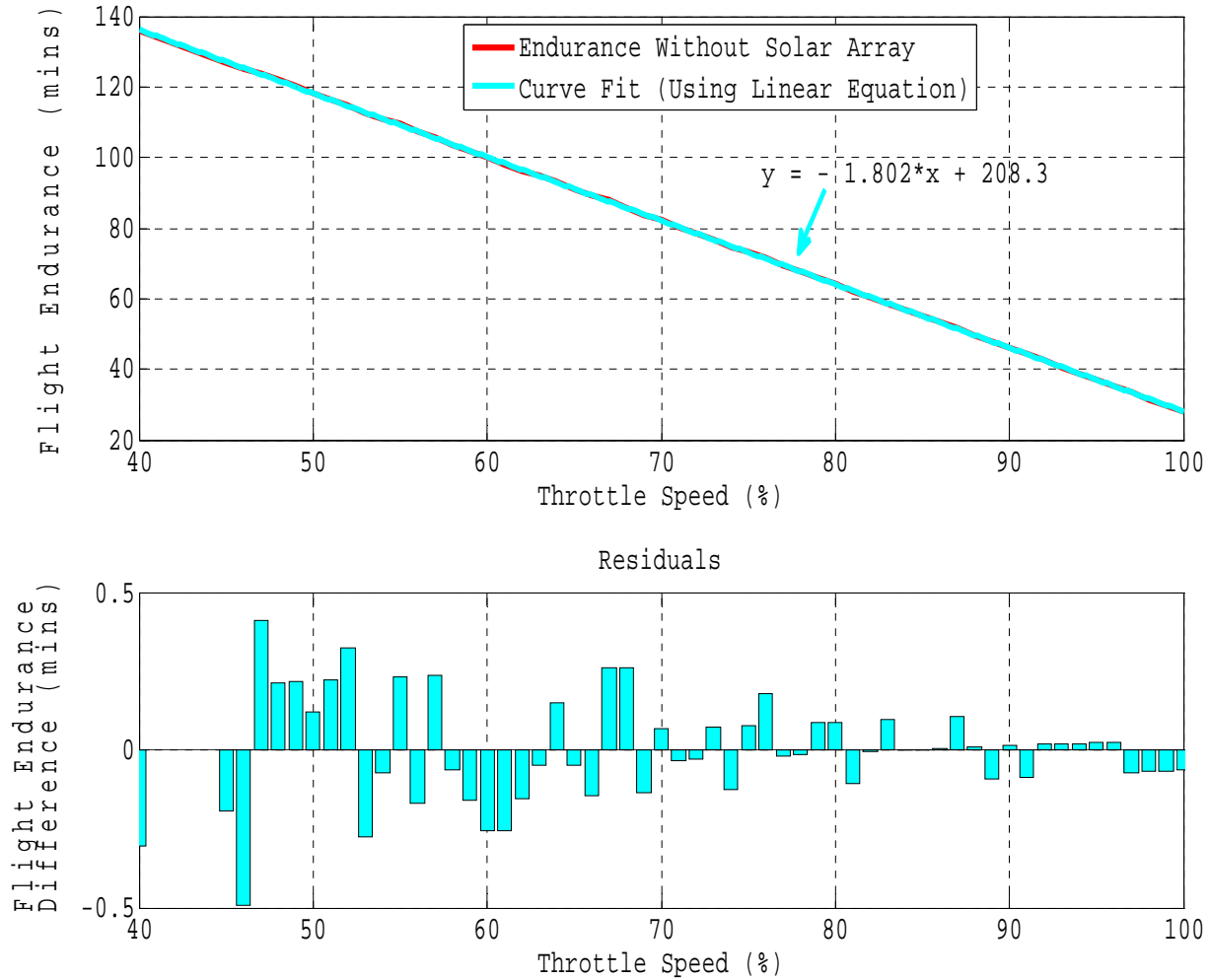


Figure 81. General equation associated with flight endurance (without solar array).

The straight line equation $y = -1.802x + 208.3$ shown in Figure 81 is used to estimate the flight endurance with no solar array incorporated. From the residual graph, the maximum flight deviation using the normalized flight equation is less than 0.5 minutes. Based on calculations, the overall flight equation is proven to exhibit a high

degree of accuracy at least 99.5% for the entire 40% to 100% range throttle speed setting.

**15. Normalized Equation Associated with Flight Endurance
(Solar Array with Output Power 18.11 W)**

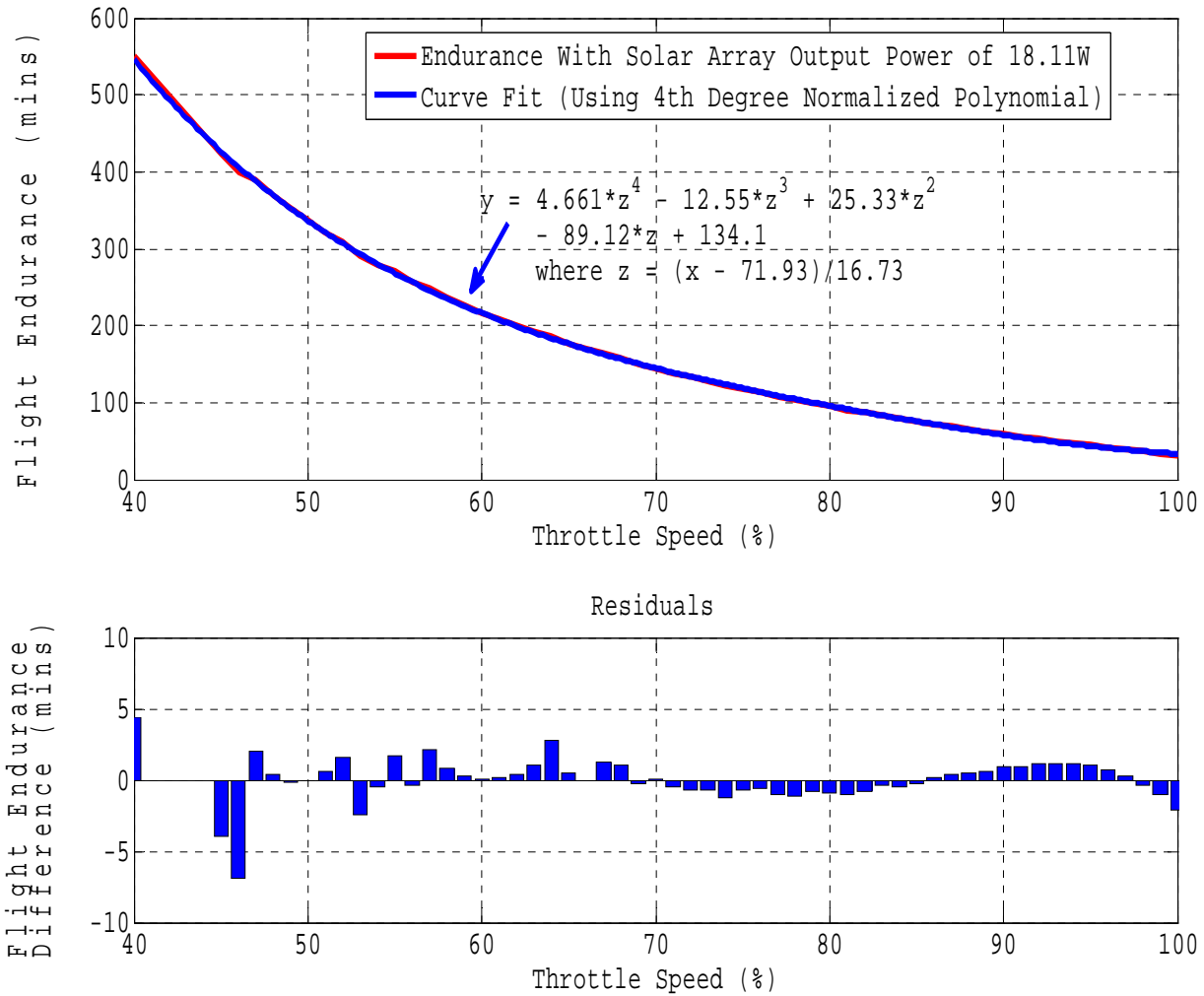


Figure 82. Normalized equation associated with flight endurance (solar array with output power 18.11 W).

A normalized 4th order normalized polynomial $y = 4.661z^4 - 12.55z^3 + 25.33z^2 - 89.12z + 134.1$, where $z = (x - 71.93)/16.73$, shown in Figure 82, is used to estimate flight endurance based on a net output power of 18.11 W.

From the residual graph, the maximum flight endurance deviation is approximately seven minutes at the 46% throttle speed setting. Based on calculations, the overall flight equation is shown to exhibit a high degree of accuracy of at least 98.3% between the 40% and 90% range throttle speed settings.

**16. Normalized Equation Associated with Flight Endurance
(Solar Array with Output Power 32.44 W)**

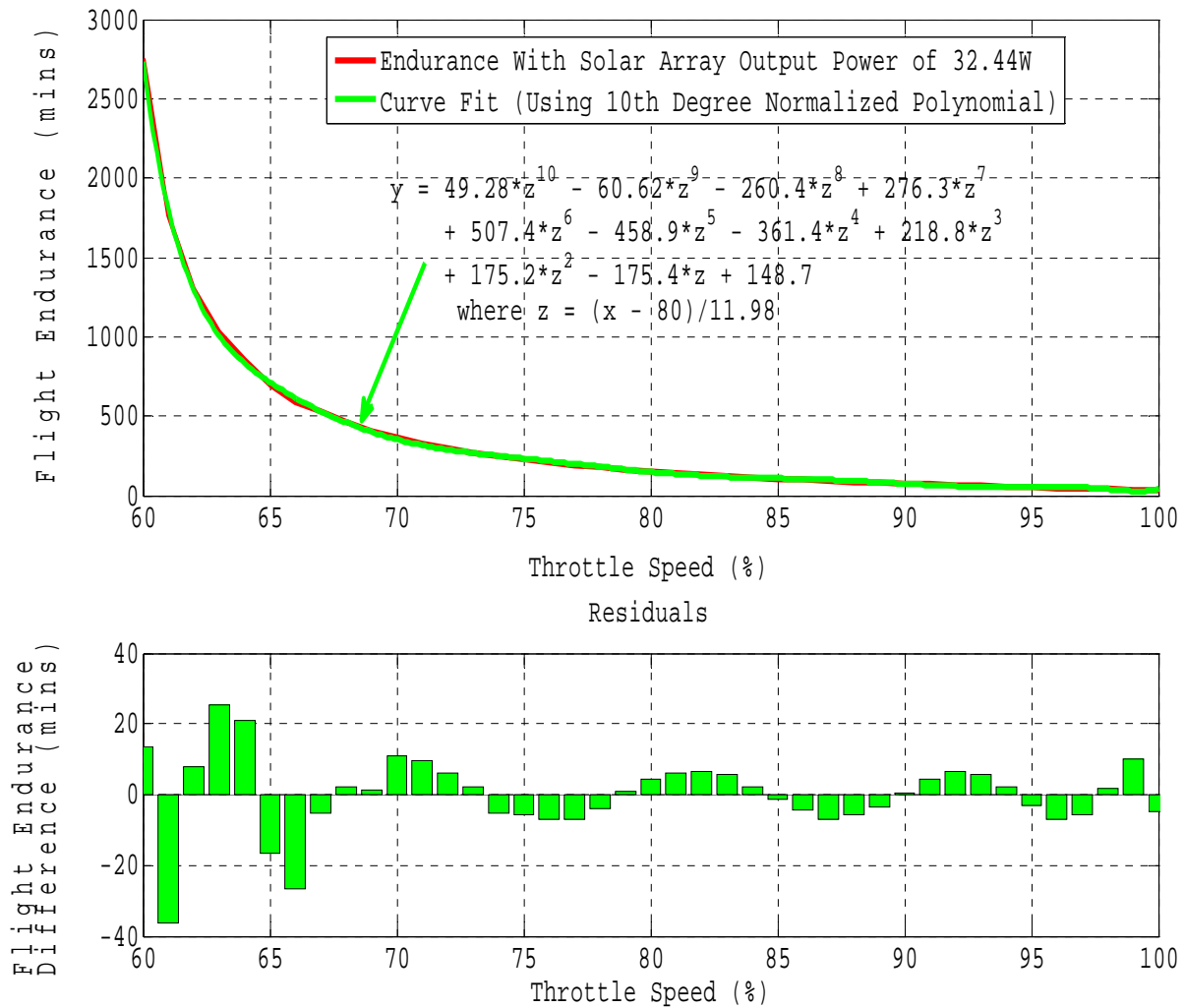


Figure 83. Normalized equation associated with flight endurance (solar array with output power 32.44 W).

A normalized 10th order normalized polynomial $y = 191.6z^{10} - 230.8z^9 - 1035z^8 + 1098z^7 + 1984z^6 - 1784z^5 - 1483z^4 + 980.4z^3 + 478.8z^2 - 302.1z + 142.7$, where $z = (x - 79.5)/12.27$, shown in Figure 83, is used to estimate the flight endurance based on a net output power of 32.44 W. This simulation shows that the flight endurance achieves infinity at throttle speed settings of 59% or less.

From the residual graph, the maximum flight endurance deviation is approximately 36 minutes at the 61% throttle speed setting. Based on calculations, the overall flight equation is shown to exhibit a high degree of accuracy of at least 95% between the 60% to 86% throttle speed settings. However, the accuracy of the normalized flight equation reduces to 84% at the 96% throttle speed setting.

It is worth noting that normalized flight equations are developed as an alternative to running simulations to provide a quick estimation of flight endurance. Nevertheless, an accurate prediction of flight endurance can still be obtained using the Simulink model for all throttle speed settings.

**17. Normalized Equation Associated with Flight Endurance
(Solar Array with Output Power 40 W)**

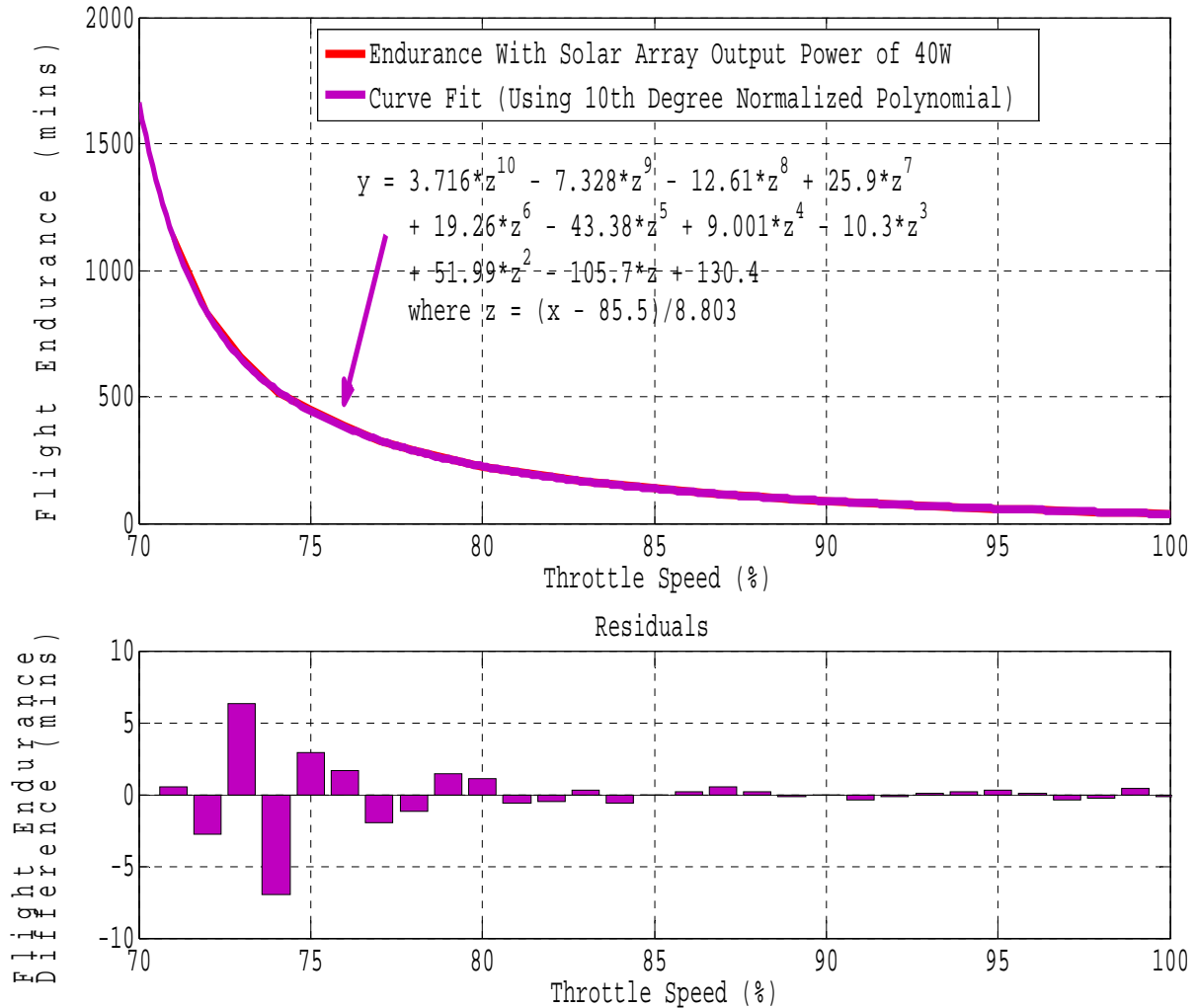


Figure 84. Normalized equation associated with flight endurance (solar array with output power 40 W).

From Figure 84, it can be seen that a normalized 10th order normalized polynomial $y = 3.716z^{10} - 7.328z^9 - 12.61z^8 + 25.9z^7 + 19.26z^6 - 43.38z^5 + 9.001z^4 - 10.3z^3 + 51.99z^2 - 105.7z + 130.4$, where $z = (x - 85.5)/8.803$, is used to estimate the flight endurance based on a net output power of 40 W from the final solar array. From the simulation, the flight endurance is infinity at throttle speed settings

of 70% or less. This means that the mini-UAV's flight can be fully sustained by solar energy when operating under constant sunlight irradiance conditions at 70% or less throttle speed settings. The on-board battery energy is only required when night falls.

From the residual graph, the maximum flight endurance deviation is approximately seven minutes at the 74% throttle speed setting. Based on calculations, the overall flight equation is shown to exhibit a high degree of accuracy of at least 98.6% between the range throttle speed settings of 71% to 100%.

E. CONCLUSION ON SIMULATION WORK

From Figures 82 to 84, it can be seen that the normalized flight equations offer a close approximation of the simulated flight endurance as an alternative. In conclusion, data collected from the simulations for the final solar array shows that perpetual flight can be achieved under constant sunlight irradiance conditions with an output solar power of 32.44 W or greater at the 60% or less throttle speed settings.

F. OBSERVATIONS

1. Ground Tests

Ground tests were planned to validate the simulation results of the enhanced simulation model. However, due to weather limitations in the local Monterey area, it was not possible to obtain adequate sunlight hours during the research phase of this thesis. However, this validation can be performed if future practical testing is carried out

under simulated AM 1.5 sunlight irradiance conditions or at a test site with adequate sunlight conditions.

2. Operating Temperature and Sunlight Irradiance

It was assumed that the parameters of the solar array used in the Simulink models remained constant and unaffected by the operating temperature and sunlight irradiance throughout the entire simulation. However, this may not be true as the operating temperature and sunlight irradiance index are expected to vary due to natural wind and different weather conditions (e.g., cloudy skies, noon hours, sunset hours, etc.) at time of flight. When the operating temperature is reduced, the solar array produces a higher output DC voltage. This potentially minimizes power loss during the DC-to-DC power conversion phase, leading to a higher overall output power. Conversely, the output power decreases when the sunlight irradiance index reduces (reduction in electron-hole pair generation).

Nevertheless, the reduction in output power can be compensated by operating the mini-UAV at its optimum performance speed and in areas where there is a higher sunlight irradiance index (e.g., Arizona). In this case, it is possible to maintain full charge on the battery energy capacity during day flight. When night falls, the battery power is used to sustain night operation.

3. Simulink Models

The Simulink models used in this thesis are designed to suit a wide range of operating conditions. Parameters such as the solar array's surface area, cell's efficiency, and DC-to-DC power converter's efficiency can be easily modified to meet specific operating conditions. The

existing models can be further tailored to include new sub-models to simulate the flight endurance of entirely different mini-UAVs or for different classes of UAVs. Mathematical flight equations can also be developed quickly to predict the flight endurance.

The main limitation faced with simulation is the lack of real data collected to validate other types or classes of UAV performance. In addition, the accuracy can be further impacted by the adequacy of the model. To overcome these limitations, the new Simulink models (included with additional sub-models) should be tested extensively to validate its adequacy by using real data collected from the UAV operators.

G. CHAPTER SUMMARY

The maximum output power extracted from the final solar array was 40 W. Basic Simulink models were first validated by predicting the overall flight endurance against the actual flight endurance data [3]. The basic validated Simulink model was subsequently enhanced to predict the flight endurance based on new input parameters for the final solar array. Equivalent normalized flight endurance equations for different energy consumptions were also developed.

It is also worth mentioning that the Simulink models are extremely flexible and can be tailored to consider new operating factors for different UAVs operating in different environments.

In the next chapter, conclusions for the thesis and recommendations for future research are discussed.

VIII. CONCLUSIONS

In this thesis, different mini-UAV systems were explored, including their capabilities, advantages and limitations. A key point to understand is the importance of using a mini-UAV with a large surface wing area. This large surface area allows the application of solar cells, which can be used to extend flight endurance by complementing on-board battery power.

The various types of energy storage technologies and fuel cell systems are also examined. It is noted that lithium-ion and lithium-polymer battery technologies are still highly practical and suitable for mini-UAV applications. This is primarily due to their high specific energy density and their reasonable specific power density.

The chemistry and physics aspects of solar cells were also discussed. Equations related to the calculation of solar cell's efficiency and fill factor were also presented. Specifically, the advantages and factors affecting the performance of CIGS solar cells were considered before the construction phase for the final solar array.

Preliminary test approaches were introduced to determine the range of output power harnessed from the experimental solar panels. It was observed that the laminated solar panels offer a better fill factor and efficiency. The lamination also acts as a protective layer on the top surface of the cell. The final solar array was then constructed and consisted of forty-eight cells

connected in series, yielding a total surface area of 3360cm². It was designed to provide an approximate output power of 40 W under good sunlight irradiance conditions.

Basic simulation models were developed and validated to estimate the flight endurance of the mini-UAV. They were then enhanced to estimate the flight endurance for the final solar array operating at different throttle speed setting. Normalized flight equations were also developed as an alternative to the actual flight testing. Analysis of the simulation results revealed that the on-board battery energy capacity remained at full capacity when the mini-UAV operated at 70% or less throttle speed settings. It was noted that the simulation models developed are extremely user-friendly, flexible and easy to modify to include new parameters for different classes of UAV.

For this thesis, the technology demonstration of using solar cells on-board mini-UAV shows that the entire flight can be fully sustained by power extracted from the solar array during good (somewhere close to AM 1.5 irradiance conditions) daylight hours when operated at cruising throttle speed.

A. RECOMMENDATIONS

1. Simulation Models

It is recommended to further enhance the existing simulation models to include a wider range of operating conditions and different classes or types of UAVs. One of the main limitations in the existing simulation models is the assumption that there is constant sunlight irradiance throughout the entire simulation period. However, sunlight

irradiance varies with time. For example, the irradiance index increases and peaks near noon before it decreases as sunset approaches. Depending on the season and time of the year and day, the varying sunlight irradiance index will affect the output power of the solar array. The simulation results will be more accurate if the enhanced simulation models can incorporate the effects of varying sunlight irradiance.

2. New Technology CIGS, Energy Storage, and Power Electronics Devices

The efficiency of the existing flexible CIGS cells used for the solar array is rated at 13%. This is one of the most efficient flexible cells on the market today. Based on a surface area of 3360 cm², the solar array is able to produce a maximum output power of 43.7 W at 13% efficiency based on AM 1.5 irradiance conditions. This translates to operating the mini-UAV at 70% throttle speed without utilizing battery energy during day mission flights.

Therefore, it is recommended to use more efficient solar cells (such as futuristic flexible triple junction cells) and DC-to-DC power converter (with MPPT algorithm) with a larger surface wing area and higher battery energy storage capacity to achieve perpetual flight capability.

3. Improved Aerodynamics

To achieve substantial flight endurance, besides using highly efficient solar cells capable of large battery

storage capacity, it is crucial that the UAV's wing airfoil is constructed to deliver good aerodynamics/lift capability as seen in Figure 85.

Therefore, the wing's upper surface is shaped such that the air rushing over the top speeds up and stretches out. This decreases the air pressure above the wing. Since high air pressure always moves towards low air pressure, the air below the wing pushes upward towards the air above the wing. Since the wing is in the middle, the whole mini-UAV is lifted in this case [106].

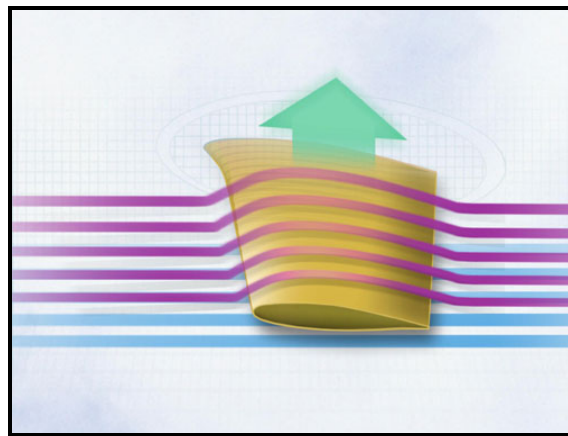


Figure 85. Airfoil. (After [106]).

4. Indoor Testing Facility

One of the major constraints for outdoor testing is the weather conditions. In the local Monterey area, the weather conditions are generally cool and cloudy. This means that except on a very good day, it is rather difficult to obtain a strong sunlight irradiance index for accurate testing. Therefore, it is recommended to provide an indoor testing facility to simulate AM 1.5 sunlight irradiance conditions so that the testing phase can be independent of the weather conditions.

APPENDIX A. MATLAB SOURCE CODES

The Matlab codes for the simulations in this thesis are provided in this appendix. The generic codes for the Simulink model to generate the flight endurance at three different output powers are contained in Section A. The data and generic codes to generate the plots for the various flight endurance at different throttle speed settings contained in Section B.

A. GENERIC CODES FOR SIMULINK MODEL

```
%Simulation for all throttle speeds at 40.0W, 32.44W, 18.11W, and with  
no solar output power.
```

```
clc  
plot  
(Time,Overall_Energy_Consumption_Graph_Without_MPPT,'r',Time,Overall_En  
ergy_Consumption_Graph_At_18_pt_48WH,'b',Time,Overall_Energy_Consumptio  
n_Graph_At_33_pt_1WH,'g',Time,Overall_Energy_Consumption_Graph_At_38WH,  
'm');  
title('Battery Energy Consumption W/ and W/O Solar Array (40W, 32.44W  
and 18.11W) for Throttle Speed (100%-XX%) Vs Time')  
xlabel('Time (s)')  
ylabel('Energy (WH)')  
legend ('No Solar Array','Solar Array with 18.11W','Solar Array with  
32.44W','Solar Array with 40.0W')  
grid on;  
hold off;
```

B. DATA AND GENERIC CODES FOR PLOTTING VARIOUS FLIGHT ENDURANCES AT DIFFERENT THROTTLE SPEED SETTINGS

```
%Flight endurance Vs throttle speed settings  
clc  
Duration_Without_Solar_Array=[135.9, 127.0, 124.9, 124.0, 122.0, 120.2,  
118.3, 116.6, 114.9, 112.5, 110.9, 109.4, 107.2, 105.8, 103.7, 101.8,  
99.9, 98.1, 96.4, 94.7, 93.1, 91.1, 89.2, 87.8, 86.0, 83.8, 82.2, 80.3,  
78.5, 76.8, 74.8, 73.2, 71.5, 69.5, 67.7, 66.0, 64.2, 62.2, 60.5, 58.8,  
56.9, 55.1, 53.3, 51.6, 49.7, 47.8, 46.1, 44.2, 42.5, 40.7, 38.9, 37.1,  
35.3, 33.4, 31.6, 29.8, 28.0];  
Duration_With_Solar_Array_At_18_Pt_11W=[550.1, 422.9, 399.8, 389.7,  
370.1, 352.4, 336.4, 321.8, 308.4, 290.7, 279.8, 269.8, 256.2, 247.8,  
236.2, 225.8, 216.3, 207.6, 199.5, 192.2, 186.3, 176.9, 169.4, 164.1,  
157.6, 150.2, 144.8, 138.6, 133.0, 127.8, 122.1, 117.8, 113.1, 108.0,  
103.4, 99.3, 94.9, 90.5, 86.6, 83.0, 79.0, 75.4, 72.0, 68.6, 65.2,
```

```

61.8, 58.8, 55.6, 52.7, 49.8, 47.0, 44.3, 41.6, 38.9, 36.3, 33.9,
31.4];
t1=[40, 45, 46, 47, 48, 49, 50, 51, 52, 53, 54, 55, 56, 57, 58, 59, 60,
61, 62, 63, 64, 65, 66, 67, 68, 69, 70, 71, 72, 73, 74, 75, 76, 77, 78,
79, 80, 81, 82, 83, 84, 85, 86, 87, 88, 89, 90, 91, 92, 93, 94, 95, 96,
97, 98, 99, 100];
Duration_With_Solar_Array_At_32_Pt_44W=[2750.0, 1764.7, 1299.0, 1031.8,
854.2, 695.4, 587.8, 526.4, 462.3, 401.5, 363.9, 325.9, 295.0, 269.8,
244.7, 227.4, 209.5, 192.2, 177.6, 165.2, 153.0, 141.4, 131.6, 123.2,
114.3, 106.7, 99.6, 93.0, 86.5, 80.5, 75.2, 69.9, 65.2, 60.6, 56.3,
52.3, 48.4, 44.7, 41.2, 37.9, 34.8];
t2=[60, 61, 62, 63, 64, 65, 66, 67, 68, 69, 70, 71, 72, 73, 74, 75, 76,
77, 78, 79, 80, 81, 82, 83, 84, 85, 86, 87, 88, 89, 90, 91, 92, 93, 94,
95, 96, 97, 98, 99, 100];
Duration_With_Solar_Array_At_40W=[1133.6, 825.9, 651.8, 520, 446, 80.9,
326.2, 285.5, 254.1, 225.8, 201, 181.4, 165.3, 149.4, 136.5, 124.8,
114.4, 104.5, 95.7, 88.2, 80.8, 74.4, 68.4, 62.8, 57.8, 53.0, 48.4,
44.3, 40.5, 36.8];
t3=[71, 72, 73, 74, 75, 76, 77, 78, 79, 80, 81, 82, 83, 84, 85, 86, 87,
88, 89, 90, 91, 92, 93, 94, 95, 96, 97, 98, 99, 100];
plot(t1,Duration_Without_Solar_Array,'r',t1,Duration_With_Solar_Array_A
t_18_Pt_11W,'b',t2,Duration_With_Solar_Array_At_32_Pt_44W,'g',t3,Durati
on_With_Solar_Array_At_40W,'m');
title('Throttle Speed Vs Flight Endurance')
xlabel('Throttle Speed (%)')
ylabel('Flight Endurance (mins)')
legend ('Endurance Without Solar Array','Endurance With Solar Array At
18.11W','Endurance With Solar Array At 32.44W','Endurance With Solar
Array At 40W')
grid on;
hold off;

```

LIST OF REFERENCES

- [1] K. C. Wong, "Aerospace Industry Opportunities in Australia - UNMANNED AERIAL VEHICLES (UAVs) - Are They Ready This Time? Are We?" Department of Aeronautical Engineering, University of Sydney, November 1997, [Online]. Available: http://sydney.edu.au/engineering/aeromech/wwwdocs/UAV_RAeS_prez_26Nov97.PDF. [Accessed 9 November 2010]
- [2] J. L. Flatley, "Zephyr Solar UAV Sets Yet Another Flight Record: 7 Days and Counting!" July 2010, [Online]. Available: <http://www.engadget.com/2010/07/17/zephyr-solar-uav-sets-yet-another-flight-record-7-days-and-coun/>. [Accessed 5 October 2010]
- [3] J. V. Coba, "Application of Copper Indium Gallium Diselenide Photovoltaic Cells to Extend The Endurance and Capabilities of The Raven RQ-11B Unmanned Aerial Vehicle," Master's Thesis, Naval Postgraduate School, Monterey, California, September 2009.
- [4] TTU International Bimonthly Newsletter on Defence and Strategy, "UAV: EADS, HELPING TO BUILD STRATEGIC AUTONOMY," July 2010, [Online]. Available: <http://www.ttu.fr/english/endocpdf/EADSUAVTTU2010.pdf> [Accessed 12 November 2010]
- [5] Aviationnews.eu, "EADS Defence & Security Delivers Second Batch of DRAC UAVs to French Ministry of Defence," February 2010, [Online]. Available: <http://www.aviationnews.eu/2010/02/10/eads-defence-security-delivers-second-batch-of-drac-uavs-to-french-ministry-of-defence/>. [Accessed 12 November 2010]
- [6] Google, "DRAC Mini UAV Images," 2010, [Online]. Available: http://www.google.com/images?hl=en&expIds=17050,25657,26486,26488,26492,26500,27028,27404,27601,27607&sugexp=ldym1s&xhr=t&q=drac+mini+uav&cp=13&rlz=1R2GGLL_zh-CN&wrapid=tljpl289808511682022&um=1&ie=UTF-8&source=og&sa=N&tab=wi&biw=1259&bih=598. [Accessed 12 November 2010]

- [7] Raven RQ-11B, "Technical Specifications," January 2009, [Online]. Available: http://www.avinc.com/downloads/AV_RAVEN-DOM_V10109.pdf. [Accessed 12 November 2010]
- [8] The Official Website of the U.S. Air Force, "Raven RQ-11B," January 2010, [Online]. Available: <http://www.af.mil/information/factsheets/factsheet.asp?id=10446>. [Accessed 12 November 2010]
- [9] Google, "Raven RQ-11B Mini UAV Images," 2010, [Online]. Available: http://www.google.com/images?hl=en&source=imghp&biw=1276&bih=598&q=Raven+RQ-11B+uav&gbv=2&aq=f&aqi=&aql=&oq=&gs_rfai=. [Accessed 12 November 2010]
- [10] Lockheed Martin, "Desert Hawk III - Putting Capability in the Hands of the Warfighter," 2006, [Online]. Available: <http://www.lockheedmartin.com/data/assets/14502.pdf> [Accessed 12 November 2010]
- [11] Google, "Desert Hawk III Mini UAV Images," 2010, [Online]. Available: http://www.google.com/images?hl=en&expIds=17259,26831,27404,27601&sugexp=cilb&xhr=t&q=desert+hawk+iii&cp=15&rlz=1R2GGLL_zh-CN&wrapid=tljpl28967812340902&um=1&ie=UTF-8&source=og&sa=N&tab=wi&biw=1276&bih=598. [Accessed 12 November 2010]
- [12] Innovative UAV Aircraft & Aerial Video Systems™, "DraganFly Tango," 2010, [Online]. Available: <http://www.draganfly.com/uav-airplane/tango/specifications/>. [Accessed 12 November 2010]
- [13] EMT, "Aladin," 2010, [Online]. Available: http://www.emt-penzberg.de/fileadmin/download/ALADIN_en.pdf. [Accessed 12 November 2010]
- [14] EMT, "Aladin," 2010, [Online]. Available: <http://www.emt-penzberg.de/index.php?id=13&L=1>. [Accessed 12 November 2010]

- [15] Google, "Aladin Mini UAV Images," 2010, [Online]. Available: http://www.google.com/images?hl=en&expIds=17259,26831,27404,27601&sugexp=cilb&xhr=t&q=aladin+mini+uav&cp=15&rlz=1R2GGLL_zh-CN&wrapid=tljpl289662060590022&um=1&ie=UTF-8&source=og&sa=N&tab=wi&biw=1259&bih=598 [Accessed 12 November 2010]
- [16] Defense Updates, "Skylark 1LE Man Portable Mini UAV System," 2009, [Online]. Available: <http://defense-update.com/products/s/skylark1-uav.htm#more> [Accessed 11 November 2010]
- [17] Defense Updates International Online Defense Magazine, "Skylark II," 2006, [Online]. Available: <http://defense-update.com/products/s/skylark2.htm> [Accessed 12 November 2010]
- [18] Israeli Weapons Ltd, "Skylark1," 2010, [Online]. Available: <http://www.israeli-weapons.com/weapons/aircraft/uav/skylark/Skylark.html> [Accessed 12 November 2010]
- [19] Defense Update, "Skylark II," 2006, [Online]. Available: <http://defense-update.com/products/s/skylark2.htm> [Accessed 12 November 2010]
- [20] Israeli Weapons Ltd, "Skylark UAV Enters IDF Service," 2010, [Online]. Available: <http://www.israeli-weapons.com/weapons/aircraft/uav/skylark/Skylark.html> [Accessed 12 November 2010]
- [21] Naval Technology.com, "ScanEagle Mini-UAV, USA," 2010, [Online]. 2010. Available: <http://www.naval-technology.com/projects/scaneagle-uav/> [Accessed 12 November 2010]
- [22] The Official Website of the U.S. Air Force, "ScanEagle," November 2009, [Online]. Available: <http://www.af.mil/information/factsheets/factsheet.asp?id=10468> [Accessed 12 November 2010]

- [23] Defense Update, "Skylite B Mini UAV," 2009, [Online]. Available: <http://defense-update.com/products/s/skylite-B.htm> [Accessed 11 November 2010]
- [24] Rafael, "Skylite B - Long - Endurance Mini - UAV," 2010, [Online]. Available: http://www.rafael.co.il/marketing/SIP_STORAGE/FILES/7/967.pdf[Accessed 12 November 2010]
- [25] Directory of U.S. Military Rockets and Missiles, "AeroEnvironment Puma," January 2007, [Online]. <http://www.designation-systems.net/dusrm/app4/puma.html> [Accessed 12 November 2010]
- [26] Defense Industry Daily, "Puma AE: An "All Environment Mini-UAV," October 2010, [Online]. Available: <http://www.defenseindustrydaily.com/Puma-AE-An-All-Environment-Mini-UAV-04962/#hand-launched-uav> [Accessed 12 November 2010]
- [27] UNMANNED AERIAL VEHICLES AND DRONES, "OUTLOOK/SPECIFICATIONS," 2010, [Online]. Available: http://www.aviationweek.com/media/pdf/spec_04_uav.pdf [Accessed 12 November 2010]
- [28] Puma AE, "Technical Specifications," 2010, [Online]. Available: http://www.avinc.com/downloads/AV_PUMAAE_V10109.pdf. [Accessed 12 November 2010]
- [29] Military and Aerospace, "Puma Miniature UAV Lands on Water and Ground For Special Forces Applications," 2010, [Online]. Available: <http://www.militaryaerospace.com/index/display/article-display/364954/articles/military-aerospace-electronics/online-news/puma-miniature-uav-lands-on-water-and-ground-for-special-forces-applications.html> [Accessed 12 November 2010]
- [30] ST Aerospace, "Skyblade III," 2008, [Online]. Available: <http://www.staero.aero/www/keyoffering.asp?serkeyid=0DAwMDAwMTg> [Accessed 12 November 2010]

- [31] Defence Science Organization, "Technologies," 2009, [Online]. Available: <http://www.dso.org.sg/technologies.aspx> [Accessed 12 November 2010]
- [32] P. F. Ribeiro, M. L. Crowand, B. K. Johnson, A. Arsoy and Y. Liu, "Energy Storage Systems for Advanced Power Applications," December 2001, [Online]. Available: <http://www.calvin.edu/~pribeiro/misc/Papers%20Published/energy%20storage%20systems.pdf> [Accessed 5 Oct 2010]
- [33] Wikipedia, "Sodium Sulfur Battery," October 2010, [Online]. Available: http://en.wikipedia.org/wiki/NaS_battery [Accessed 15 October 2010]
- [34] The Energy Blog, "About Sodium-Sulfur (NaS) Batteries," November 2010, [Online]. Available: http://thefraserdomain.typepad.com/energy/2006/01/sodiumsulfur_na.html [Accessed 7 October 2010]
- [35] Wikipedia, "Lithium Sulfur Battery," October 2010, [Online]. Available: http://en.wikipedia.org/wiki/Lithium_sulfur_battery [Accessed 5 October 2010]
- [36] The Encyclopedia of Alternative Energy and Sustainable Living, "Lithium-sulfur battery," November 2010, [Online]. Available: http://www.daviddarling.info/encyclopedia/L/AE_lithium-sulfur_battery.html [Accessed 5 November 2010]
- [37] D. Borghino, "Lithium-Sulfur Batteries Could Store Triple The Power of Lithium-Ion," June 2009, [Online]. Available: <http://www.gizmag.com/next-generation-battery-lithium-sulphur/11926/> [Accessed 5 October 2010]
- [38] Wikipedia, "Lithium-Ion Polymer Battery," October 2010.

- [39] Hobby-Lobby International Inc, "Lithium Polymer," November 2010. [Online]. Available: http://www.hobby-lobby.com/pro_lite_v2_5_cell_3300_mah_18.5v_20c_lipoly_1033780_prd1.htm. [Accessed 5 November 2010]
- [40] Batteries and Energy Technologies, "Rechargeable Lithium Batteries," 2005, [Online]. Available: <http://www.mpoweruk.com/lithiumS.htm>. [Accessed 5 October 2010]
- [41] Battery University, "The Nickel-Based Battery, Its Dominance, and the Future," 2010, [Online]. Available: http://batteryuniversity.com/learn/article/the_nickel_based_battery_its_dominance_and_the_future. [Accessed 5 October 2010]
- [42] Hobby-Lobby International Inc, "Nickel Cadmium and Nickel Metal Hydride," November 2010, [Online]. Available: http://www.hobby-lobby.com/all_nicad_nimh_batteries_326_ctg.htm [Accessed 5 November 2010]
- [43] Wikipedia, "Nickel-Cadmium Battery," November 2010, [Online]. Available http://en.wikipedia.org/wiki/Nickel-cadmium_battery [Accessed 5 November 2010]
- [44] Fit My Budget, "High Capacity Rechargeable NiMH Battery Pack 4.8V for Cobra Radios FA-BP," 2010, [Online]. Available: <http://www.fitsmybudget.com/product.php?productid=17785> [Accessed 5 November 2010]
- [45] K.on Lee, J. Yi, B. Kim, J. Ko, S.n Jeong, M. Noh, and S. S. Lee "Micro-energy storage system using permanent magnet and high-temperature superconductor," September 2007, [Online]. Available: http://mmst.kaist.ac.kr/results/A_61.pdf [Accessed 5 Oct 2010]
- [46] Zoom Performance Product, "Performance Flywheels," September 2010, [Online]. Available: <http://zoomperformance.com/flywheels.html>. [Accessed 5 November 2010]

- [47] Federal Technology Alert, "Flywheel Energy Storage," September 2003, [Online]. Available: http://www1.eere.energy.gov/femp/pdfs/fta_flywheel.pdf [Accessed 5 November 2010]
- [48] Wikipedia, "Flywheel Energy Storage," October 2010, [Online] Available: http://en.wikipedia.org/wiki/Flywheel_energy_storage [Accessed 5 November 2010]
- [49] CAP.XX, "Energy Storage Technologies: A Comparison," 2008, [Online]. Available: http://www.cap-xx.com/resources/reviews/strge_cmprsn.htm [Accessed 5 November 2010]
- [50] Alternative Energy - Alternative Fuels, "Electric Cars- New developments could See The End of The Gas Guzzlers," 2010 [Online]. Available: <http://www.alternative-energy.everything-fine.com/electric-cars-new-developments-could-see-the-end-of-the-gas-guzzlers/> [Accessed 5 November 2010]
- [51] Kidwind Project, "Using Mini-Supercapacitors to Store Energy," 2010, [Online]. Available: http://www.kidwind.org/PDFs/SUPPORT_Supercapacitors.pdf [Accessed 5 November 2010]
- [52] Battery University, "What's The Role of Supercapacitor," 2010, [Online]. Available: <http://www.batteryuniversity.com/partone-8.htm>. [Accessed 5 November 2010]
- [53] Marco Semadeni, "Energy Storage as an Essential Part of Sustainable Energy Systems," May 2003, [Online]. Available: http://www.cepe.ethz.ch/publications/workingPapers/CEPE_WP24.pdf. [Accessed 12 November 2010]
- [54] The Electropadia, "Battery and Energy Technologies," 2005 [Online]. Available: <http://www.mpoweruk.com/specifications/comparisons.pdf> [Accessed 12 November 2010]

- [55] Network for Renewable Energy Research, "Introduction to Hydrogen and Fuel Cell," 2010 [Online]. Available: http://www.intelligent-energy.com/products_and_services/fuel_cells/how_they_work/ [Accessed 5 November]
- [56] Intelligent Energy, "What Is a Fuel Cell," 2010 [Online]. Available: http://www.intelligent-energy.com/products_and_services/fuel_cells/how_they_work/ [Accessed 5 November]
- [57] S. P. S. Badwal, S. Giddey and P. Bandopadhyay, "Hydrogen, Fuel Cells and Renewable Energy" [Online]. Available: http://www.latrobe.edu.au/csrc/conferences/rera/presentations/badwal_sukhvinder.pdf [Accessed 5 November 2010]
- [58] Defense Update, "Birdeye 650LE Mini-UAV Uses Fuel Cells to Fly 6 Hours Mission," 2010 [Online]. Available: http://www.defence-update.net/wordpress/20100823_birdeye-650le.html [Accessed 5 November 2010]
- [59] Science Daily, "Ion Tiger Fuel Cell Unmanned Air Vehicle Completes 23-Hour Flight," October 2009, [Online] Available <http://www.sciencedaily.com/releases/2009/10/091013123350.htm>. [Accessed 8 November 2010]
- [60] X. Liu, X. Zhang, Y. Zhang, G. Ding, "Development of Micro Fuel Cell," IEEE Explore. July 2010 [Online]. Available http://ieeexplore.ieee.org.libproxy.nps.edu/search/srchabstract.jsp?tp=&arnumber=5615353&queryText%3Dmicro+fuel+cells%26openedRefinements%3D*%26rowsPerPage%3D100%26searchField%3DSearch+All&tag=1 [Accessed 5 November 2010]
- [61] Aalto University, "Fuel Cells," 2002 [Online]. Available: <http://www.tkk.fi/Units/AES/projects/renew/fuelcell/posters/fuelcells.html> [Accessed 7 November 2010]
- [62] Wikipedia, "Direct Methanol Fuel Cell," July 2010.

- [63] Fuel Cells for Power, "Direct Methanol Fuel Cell (DMFC)," 2010, [Online]. Available: http://www.fuelcellsforpower.com/index.php?option=com_content&view=article&id=48&Itemid=54. [Accessed 6 November 2010]
- [64] J. P. Esquivel, N. Sabate, J. Santander, N. Torres, I. Gracia, L. Fonseca, P. Ivanov and C. Cane, "A Silicon-Based Direct Methanol Micro Fuel Cell," IEEE Explore. January 2007, [Online]. Available: <http://ieeexplore.ieee.org.libproxy.nps.edu/stamp/stamp.jsp?tp=&arnumber=4271198&tag=1> [Accessed 6 November 2010]
- [65] Shanghai Institute of Microsystem and Information Technology, "Micro Direct Methanol Fuel Cell," 2009, [Online]. Available: http://english.sim.cas.cn/rh/as/200906/t20090629_9412.html [Accessed 7 November 2010]
- [66] U.S. Department of Energy, "Fuel Cell," June 2009. [Online]. Available: http://www1.eere.energy.gov/hydrogenandfuelcells/fuelcells/fc_types.html#phosphoric [Accessed 7 November 2010]
- [67] U.S. Department of Energy, "Phosphoric Acid Fuel Cell Technology," January 2011, [Online]. Available: http://www.fossil.energy.gov/programs/powersystems/fuelcells/fuelcells_phosacid.html [Accessed 17 February 2011]
- [68] Wikipedia, "Molten Carbonate Fuel Cell," August 2010.
- [69] U.S. Department of Energy, "Fuel Cell," June 2009, [Online]. Available: http://www1.eere.energy.gov/hydrogenandfuelcells/fuelcells/fc_types.html#molten [Accessed 7 November 2010]
- [70] Wikipedia, "Solid Oxide Fuel Cell," November 2010.
- [71] U.S. Department of Energy, "Fuel Cell," June 2009, [Online]. Available: http://www1.eere.energy.gov/hydrogenandfuelcells/fuelcells/fc_types.html#oxide. [Accessed 7 November 2010]

- [72] Fuel Cell Basics, "Regenerative Fuel Cells," 2011, [Online]. Available: http://www.fctec.com/fctec_types_rfc.asp [Accessed 17 February 2011]
- [73] National Fuel Cell Research Center - University of California, Irvine, "Electrolyzer and Reversible Fuel Cell," 2009, [Online]. Available: <http://www.nfccr.uci.edu/2/ACTIVITIES/PROJECTS/hydrogen/ElectrolyzerandReversibleFuelCell.aspx> [Accessed 8 November 2010]
- [74] Infinity Fuel Cell, "Regenerative Fuel Cells," 2011, [Online]. Available: <http://www.infinityfuel.com/regenfuelcells.htm> [Accessed 17 February 2011]
- [75] SolarBuzz, "Solar Cell Technologies," 2010, [Online]. Available: <http://www.solarbuzz.com/Technologies.htm>. [Accessed 18 November 2010]
- [76] Renewable Energy World.com, "Efficiency Record of 17.6% on Flexible CIGS Solar Cell on Plastic Developed at EMPA," September 2010, [Online]. Available: <http://www.renewableenergyworld.com/rea/partner/first-conferences/news/article/2010/09/efficiency-record-of-17-6-on-flexible-cigs-solar-cell-on-plastic-developed-at-empa> [Accessed 18 November 2010]
- [77] Global Solar Energy, "CIGS Thin Film Material," 2009, [Online]. Available: <http://www.globalsolar.com/en/products/cigs-thin-film-material.html> [Accessed 18 November 2010]
- [78] Bright Hub, "What Happens To Solar Radiation When It Reaches The Earth As Electromagnetic Waves?" 2010, [Online]. Available: <http://www.brighthub.com/environment/renewable-energy/articles/63714.aspx> [Accessed 18 November 2010]
- [79] Wikipedia, "Electromagnetic Radiation," November 2010, [Online].

- [80] Opto IQ, "PHOTOVOLTAICS: Measuring the Sun," May 2009, [Online]. Available: <http://www.optoiq.com/index/photonics-technologies-applications/lfw-display/lfw-article-display/361941/articles/laser-focus-world/features/photovoltaics-measuring-the-sun.html> [Accessed 19 November 2010]
- [81] Australian CRC for Renewable Energy Ltd, "How Do Solar Cells Work," June 1999, [Online]. Available: <http://www.esdalcollege.nl/eos/vakken/na/zonnecel.htm> [Accessed 19 November 2010]
- [82] University of Texas at El Paso- Electrical and Computer Engineering Department, "The Energy Band Model - The Band Gap Energy," 2010, [Online]. Available: <http://www.ece.utep.edu/courses/ee3329/ee3329/Studyguide/ToC/Fundamentals/BDiagrams/conduction.html> [Accessed 20 November 2010]
- [83] Google, "Band Gap Energy Images," 2010, [Online]. Available: http://www.google.com/images?q=band%20gap%20energy%20diagram&hl=en&rlz=1R2GGLL_zh-CN&prmd=iv&psj=1&wrapid=tlif12902919013371&um=1&ie=UTF-8&source=og&sa=N&tab=wi&biw=1276&bih=598 [Accessed 20 November 2010]
- [84] Sandia National Laboratories, "Sandia's Photovoltaic Research & Development" 2010, [Online]. Available: <http://photovoltaics.sandia.gov/docs/PVFEffIntroduction.htm> [Accessed 20 November 2010]
- [85] Encyclopedia Britannica, "Solar Cell: Structure," 2005, [Online]. Available: <http://www.britannica.com/EBchecked/topic-art/552875/1406/A-commonly-used-solar-cell-structure> [Accessed 20 November 2010]
- [86] K. L. Chopra, P. D. Paulson, and V. Dutta, "Thin Film Solar Cells: An Overview," 2004, [Online]. Available: <http://159.226.64.60/fckeditor/UserFiles/File/tyndc/reference/19938777866147.pdf> [Accessed 20 November 2010]

- [87] S. Ishizuka, T. Yoshiyama, K. Mizukoshi, A. Yamada, and S.u Niki, "Monolithically Integrated CIGS Submodules Fabricated On Flexible Substrates," IEEE Explore, June 2010, [Online]. Available: <http://ieeexplore.ieee.org/stamp/stamp.jsp?arnumber=05614095> [Accessed 21 November 2010]
- [88] M. Pagliaro, R. Ciriminna, and G.i Palmisano, "Flexible Solar Cells," October 2008, [Online]. Available: <http://onlinelibrary.wiley.com/doi/10.1002/cssc.200800127/pdf> [Accessed 20 November 2010]
- [89] M. Dennis J. Coyle, Holly A. Blaydes, J. E. Pickett, R. S. Northey, and J. O. Gardner, "Degradation Kinetics of CIGS Solar Cells," IEEE Explore, June 2009, [Online]. Available: <http://ieeexplore.ieee.org/stamp/stamp.jsp?arnumber=05411551> [Accessed 21 November 2010]
- [90] L. C. Olsen, M. E. Gross, G. L. Graff, S. N. Kundu, "Approaches to Encapsulation of Flexible CIGS Cells," 10 September 2008, [Online]. Available: <http://spiedl.aip.org/getpdf/servlet/GetPDFServlet?filetype=pdf&id=PSISDG007048000001704800000001&idtype=c&vips&prog=normal> [Accessed 21 November 2010]
- [91] Google, "Buck Converter Images," 2010, [Online]. Available: http://www.google.com/images?hl=en&source=imghp&biw=1276&bih=598&q=buck+converter&btnG=Search+Images&gbv=2&aq=f&aqi=&aql=&oq=&gs_rfai= [Accessed 22 November 2010]
- [92] Google, "Boost Converter Images," 2010, [Online]. Available: http://www.google.com/images?hl=en&biw=1276&bih=598&gbv=2&tbs=isch%3A1&sa=1&q=boost+converter+circuitry&aq=f&aqi=glg-m1&aql=&oq=&gs_rfai= [Accessed 22 November 2010]
- [93] "EC3150 Solid State Power Electronics Conversion." Class notes for EC3150, Department of Electrical and Computer Engineering, Naval Postgraduate School, Summer 2010.

- [94] I. Glasner, J. Appelbaum, "Advantage of Boost Vs. Buck Topology for Maximum Power Point in Photovoltaic Systems," IEEE Explore, November 1996, [Online]. Available: <http://ieeexplore.ieee.org.libproxy.nps.edu/stamp/stamp.jsp?tp=&arnumber=4651563> [Accessed 26 November 2010]
- [95] M. A. S. Masoum, M. Sarvi, "Voltage and Current Based MPPT of Solar Arrays under Variable Insolation and Temperature Conditions," IEEE Explore, September 2008, [Online]. Available: <http://ieeexplore.ieee.org.libproxy.nps.edu/Xplore/cookieDetectResponse.jsp> [Accessed 26 November 2010]
- [96] J. Ahmad, H. Kim, "A Voltage Based MPPT for Low Power and Low Cost PV Applications," 2009, [Online]. Available: <http://www.waset.org/journals/waset/v60/v60-121.pdf> [Accessed 26 November 2010]
- [97] Wikipedia, "Battery (Electricity)," November 2010.
- [98] Amprobe, "Amprobe Solar-600 Solar Analyzer," January 2011, [Online]. Available: <http://www.tequipment.net/AmprobeSOLAR-600.asp> [Accessed 11 January 2011]
- [99] Value Testers, "Amprobe Solar-100 Solar Power Meter," 2011, [Online]. Available: <http://www.valuetesters.com/Amprobe-SOLAR-100-Solar-Power-Meter.php> [Accessed 11 January 2011]
- [100] Global Solar Energy, "G2 thin film string datasheet," July 2008.
- [101] Amazon, "3 Inch Wide Carton Sealing Clear Packing Tape," 2011, [Online]. Available: http://www.amazon.com/s/ref=nb_sb_noss?url=search-alias%3Daps&field-keywords=3%22+clear+tape#/ref=sr_pg_3?rh=i%3Aaps%2Ck%3A3%22+clear+packing+tape&page=3&keywords=3%22+clear+packing+tape&ie=UTF8&qid=1295143449 [Accessed 9 January 2011]

- [102] Ampetronic, "FB1.8 Flat Copper Tape," 2011, [Online]. Available: <http://www.ampetronic.com/products/FB1.8-Flat-Copper-Tape.asp?cat=11> [Accessed 9 January 2011]
- [103] ST Microelectronics, "SPV1020," 2011, [Online]. Available: <http://www.st.com/stonline/books/pdf/docs/17588.pdf> [Accessed 12 January 2011]
- [104] Google, "SPV 1020 DC-to-DC Boost Converter," 2011, [Online]. Available: http://www.google.com/images?um=1&hl=en&rls=com.microsoft:en-sg:IE-SearchBox&rlz=1I7GGLL_zh-CN&tbs=isch:1&&sa=X&ei=44cvTbRBh6KxA-rs-b0F&ved=0CDIQBSgA&q=spv1020+stmicroelectronics&spell=1&biw=1259&bih=598 [Accessed 12 January 2011]
- [105] PowerStream, "How to calculate battery run-time," 2010, [Online]. Available: <http://www.powerstream.com/battery-capacity-calculations.htm> [Accessed 20 January 2011]
- [106] Boeing. "How Do Things Fly?" 2010 [Online]. Available: http://www.boeing.com/companyoffices/aboutus/wonder_of_flight/airfoil.html [Accessed 16 February 2011]

INITIAL DISTRIBUTION LIST

1. Defense Technical Information Center
Ft. Belvoir, Virginia
2. Dudley Knox Library
Naval Postgraduate School
Monterey, California
3. Dr. R. Clark Robertson, Chairman
Department of Electrical and Computer Engineering
Naval Postgraduate School
Monterey, California
4. Dr. Sherif Michael
Department of Electrical and Computer Engineering
Naval Postgraduate School
Monterey, California
5. Dr. Rudolf Panholzer
Space Systems Academic Group
Naval Postgraduate School
Monterey, California
6. Chee Keen Chin
Defence Science & Technology Agency
Singapore